Integrated Optical Modules for Miniature Raman Spectroscopy Devices

Fehmi Çivitci

INTEGRATED OPTICAL MODULES FOR MINIATURE RAMAN SPECTROSCOPY DEVICES

FEHMİ ÇİVİTCİ

Graduation committee:

Chairman and secretary:

Prof. Dr. P. M. G. Apers	University of Twente

Promoter:

Prof. Dr. M. Pollnau	University of Twente

Assistant promoter:

Dr. H. J. W. M. Hoekstra	University of Twente

Members:

Prof. Dr. A. Driesen	University of Twente
Dr. Ir. A. J. Annema	University of Twente
Prof. Dr. H. Ürey	Koc University
Prof. Dr. K. A. Williams	Technical Uni. of Eindhoven

The research described in this thesis was carried out at the Integrated Optical MicroSystems (IOMS) Group, Faculty of Electrical Engineering, Mathematics and Computer Science, MESA+ Institute for Nanotechnology, University of Twente, P.O. Box 217, 7500 AE, Enschede, The Netherlands. It was financially supported by the Dutch Technology Foundation – STW through project 10051 (Optical Lab in a Package).

Printed by
Copyright © 2014 by FEHMİ ÇİVİTCİ, Enschede, The Netherlands
All rights reserved.

ISBN 978-90-365-3767-4
DOI 10.3990./1.9789036537674
URL http://dx.doi.org/10.3990/1.9789036537674

INTEGRATED OPTICAL MODULES FOR MINIATURE RAMAN SPECTROSCOPY DEVICES

DISSERTATION

to obtain
the degree of doctor at the University of Twente,
on the authority of the rector magnificus,
prof. dr. H. Brinksma
on account of the decision of the graduation committee,
to be publicly defended
on Friday the 31st of October 2014 16:45

by

FEHMİ ÇİVİTCİ
born on the 11th of September 1983
in Antalya, Turkey

This dissertation is approved by:
the promoter: Prof. Dr. M. Pollnau
the assistant promoter: Dr. H. J. W. M. Hoekstra

"There is plenty of room at the bottom."

Richard Feynman, 1959

Table of Contents

LIST OF FIGURES **X**

LIST OF TABLES **XV**

ABSTRACT **XVII**

SAMENVATTING **XIX**

1 INTRODUCTION **1**

1.1 CONVENTIONAL RAMAN SPECTROSCOPY 3

1.2 SMALL SCALE RAMAN SPECTROMETER SYSTEM 4

1.2.1 Light Turning Mirror 5

1.2.2 Integrated Optics Spectrometer 6

1.2.3 Integrated Optics Polarization Splitter 7

1.3 TARGETED APPLICATION 7

1.4 ORGANIZATION OF THE THESIS 8

1.5 REFERENCES 9

2 LIGHT TURNING MIRRORS FOR HYBRID INTEGRATION OF SION-BASED OPTICAL WAVEGUIDES AND PHOTO-DETECTORS **19**

2.1 INTRODUCTION 19

2.2 DEVICE DESIGN AND CALCULATED PERFORMANCE 20

2.3 FABRICATION PROCESS 24

2.4 CHARACTERIZATION 28

2.4.1 Structural characterization 28

2.4.2 Optical characterization 29

2.5 CONCLUSIONS 32

2.6 REFERENCES 33

3 DESIGN OF A PRISM SPECTROMETER BASED ON ADIABATICALLY CONNECTED WAVEGUIDE SLABS **35**

3.1 INTRODUCTION 35

3.2 PRISM SPECTROMETER: PRINCIPLE AND BASIC THEORY 36

3.2.1 Prism 38

3.2.2 Parabolic Mirrors 43

3.2.3 Imaging of the Input Field 46
3.2.4 Effect of Phase Shift upon Reflection 51
3.3 DESIGN 53
3.3.1 Scheme 54
3.3.2 A Numerical Example 56
3.4 CONCLUSIONS 64
3.5 REFERENCES 64
4 INTEGRATED OPTICS PRISM SPECTROMETER: FABRICATION AND TESTING 67
4.1 INTRODUCTION 67
4.2 DESIGN 68
4.3 FABRICATION 75
4.4 CHARACTERIZATION 78
4.5 CONCLUSIONS 85
4.6 REFERENCES 86
5 INTEGRATED OPTICS POLARIZATION SPLITTER: DESIGN, FABRICATION AND TESTING 87
5.1 INTRODUCTION 87
5.2 DEVICE PRINCIPLE 88
5.3 DESIGN 90
5.3.1 Elliptical Mirror 91
5.3.2 Polarization Splitting Trench 95
5.4 CHARACTERIZATION 100
5.5 CONCLUSIONS 104
5.6 REFERENCES 104
6 SEMI-GUIDED PLANE WAVE REFLECTION BY THIN-FILM TRANSITIONS FOR ANGLED INCIDENCE 107
6.1 INTRODUCTION 107
6.2 SCALAR THEORY 109
6.2.1 Total Internal Reflectance 111
6.2.2 Goos-Hänchen-shift 114
6.3 EXAMPLES 116
6.3.1 Step Discontinuity 117
6.3.2 Tapered Transition 121

6.4 CONCLUSION 122
6.5 REFERENCES 123

7 CONCLUSIONS AND OUTLOOK 125
7.1 CONCLUSIONS 125
7.2 OUTLOOK 127

APPENDICES 129

APPENDIX A: SURFACE ROUGHNESS CHARACTERIZATION FOR 45° ANGLED SI WALLS 131

APPENDIX B: THERMAL OXIDATION OF ANISOTROPICALLY ETCHED SI 135

LIST OF PUBLICATIONS 138

ACKNOWLEDGEMENT 140

List of Figures

Figure 1.1: Schematic of conventional Raman spectroscopy system. 3
Figure 1.2: Schematic of the envisioned device. 5
Figure 2.1: Cross-sectional view of the proposed device............................21
Figure 2.2: (a) Cross-section of the simplified mirror structure used in the simulation and (b) calculated intensity profile at the far field for TE polarization. 23
Figure 2.3: Wafer cross-sections corresponding to different steps in the fabrication process flow. 24
Figure 2.4: (a) SEM cross section and (b) top view of Si structures etched by the optimized Si anisotropic etchant. 27
Figure 2.5: SEM photos of (a) as-deposited and (b) annealed BPSG layer on Si, which has 45° angled walls. Both photos were taken after a quick BHF dip for making the slits and voids prominent..............................27
Figure 2.6: (a) SEM cross section obtained by dicing the sample through the center of an elevated Si structure and (b) top view photograph of part of the fabricated chip showing four mirrors with corresponding waveguides as well as dummy pyramids. 29
Figure 2.7: Schematic of the optical setup used for measuring the mirror performance. 30
Figure 2.8: Measured far-field beam profiles for (a) TE- and (b) TM-polarized light. The graphs show the calculated, measured, and ideal irradiance integrated over *y*, along the x-axis for (c) TE and (d) TM polarizations. 30
Figure 2.9: Measured and fitted irradiance, integrated over *y*, along the *x*-axis for (a) TE and (b) TM polarization. 32
Figure 3.1: Schematic of the considered prism spectrometer. The white and dark grey areas correspond to thick and thin slabs, respectively. Ridge waveguides are indicated by yellow lines. The inset illustrates schematically the relation of the output intensities to the parameters that characterize the device performance. Regions with different thicknesses of the guiding layer are connected adiabatically via vertical tapering...37
Figure 3.2: Schematic (top view) of a generic prism structure. 41

Figure 3.3: Schematic pictures of the collimation mirror (a), the focusing mirror (b) and the focal area (c), introducing the used symbols. 45
Figure 3.4: Intensity profiles for modal fields (solid lines) and the corresponding images (dashed lines) for indicated parameters, calculated using Equation (3.28). 48
Figure 3.5: Relative power captured by a receiver waveguide at a distance of tw0 from the maximum of the image. 48
Figure 3.6: Modal width, FWHM of O (a) and the functional loss $O(t=0)$ as a function of V. 49
Figure 3.7: Illustration to the derivation of the effects of PSR. 53
Figure 3.8: Illustration to Equation (37) giving the approximate device area (indicated by the grey rectangle). 54
Figure 3.9: Value of the quantity R as a function of layer thicknesses h1 and h2. 57
Figure 3.10: Transmittance vs. angle of incidence on the adiabatic taper. The inset depicts the taper structure. 58
Figure 3.11: Structure of the imaginary channel waveguide used to calculate phase change upon total internal reflection of slab TE modes. 59
Figure 3.12: Simplified 1D view of the imaginary waveguide structure. 60
Figure 3.13: Phase shift upon TIR vs. incidence angle for the considered interface with 0.5° taper angle at λ = 850 nm. $\Delta\theta$ is the used incidence angle range for the designed mirror. 62
Figure 3.14: Full layout of the designed prism spectrometer, which has a size of 5.5 x 13 mm2; the inset shows the input and receiver waveguides in more detail. 63
Figure 4.1: Schematic of the fabricated spectrometer. The white and dark grey areas correspond to thick and thin slabs, respectively. Ridge waveguides are indicated by the color yellow. The symbols N refer to the effective index of the planar structures corresponding to the regions indicated by the position of these symbols. 69
Figure 4.2: Prism dispersion (D') as a function of t_1 and t_2. 71
Figure 4.3: Graph of the quantity $F_p(\eta)$. 74

Figure 4.4: Full layout of the fabricated spectrometer, which has a size of 8 x 29.5 mm^2. The figures at the bottom show the input and receiver waveguides in detail. 75
Figure 4.5: Wafer cross-sections corresponding to different steps in the fabrication process flow. 77
Figure 4.6: A top view photograph of the fabricated device. The main part of the prism in the middle and parts of the mirrors on the left and right hand sides are shown. 78
Figure 4.7: Schematic view of the optical setup used for taking the top-view photographs of the fabricated chip. 79
Figure 4.8: The set of photographs taken from the different regions of the fabricated chip while a laser source at 850 nm is coupled into the input waveguide. 81
Figure 4.9: Scheme of the setup used for acquisition of the output spectrums from the receiver waveguides for a white light input to the chip. 82
Figure 4.10: The output spectrum of the three receiver waveguides corresponding to the lowest three wavelengths of the considered wavelength region (775 – 925 nm). 83
Figure 4.11: Phase shift upon TIR vs. incidence angle for the fabricated interface with 65 µm taper length at λ = 850 nm. $\Delta\theta$ is the used incidence angle range for both the mirrors. 85
Figure 5.1: Schematic of the polarization splitter. The white and grey areas correspond to thick and thin slabs, respectively. Ridge waveguides are indicated by yellow lines. The capitals N refer to the effective index of the planar structures corresponding to the indicated regions. 89
Figure 5.2: Schematic of the elliptical mirror introducing the used symbols. 92
Figure 5.3: Schematic of the polarization splitting trench and used symbols. The rays correspond to the situation with a parallel exit interface. 96
Figure 5.4: Vertical separation between TE and TM focal points (w_s) as a function of incidence angle of the central ray (θ_i) up to the angle 2° below critical angle for reflection (61.7°). 98

Figure 5.5: Full layout of the fabricated polarization splitter, which has a size of 4.2 x 13.8 mm^2. The figures at the bottom show the input and receiver waveguides in detail. 100
Figure 5.6: Schematic view of the optical setup used for the taking top view photographs of the fabricated polarization splitter chip. 101
Figure 5.7: The set of photographs taken from the different regions of the fabricated chip while a laser source at 850 nm is coupled into the input waveguide. The first 4 photos were taken while the input is mixed polarized light, (e) and (f) were taken while the input is TE polarized light, (g) and (h) were taken while the input is TM polarized light, (i) is the combined version of (e) and (g). 103
Figure 6.1: Incidence of vertically guided, laterally unguided plane waves under an angle on a step discontinuity between regions with different core film thicknesses. Primary interest is in the relative amplitude, and in the phase, of the reflected semi-guided wave, typically as a function of the angle of incidence. This phase change, or more precisely its angular derivative, determines the lateral displacement, the so-called Goos-Hänchen shift, of an in-plane-guided beam upon reflection at the transition [8, 9]. 108
Figure 6.2: Step discontinuity, cross sectional and top views, with the relevant wave vectors and angles indicated. 109
Figure 6.3: Lateral shift Δ (Goos-Hänchen-shift) of a semi-guided beam upon total internal reflection with incidence angle θ at the border of region (I). The displacement can be viewed as the effect of a geometric reflection of the ray associated with the beam at an effective interface that is positioned at a distance δ apart from plane $z = 0$ of the physical discontinuity. 116
Figure 6.4: Reflection of a semi-guided plane wave at a step discontinuity. (a): Guided wave reflectance R, transmittance T, phase change upon reflection ϕ , and effective permitivities of the background $\epsilon_{eff,b}$ and guiding regions $\epsilon_{eff,g}$, versus the angle of incidence θ. (b): absolute values and time snapshots of the time-harmonic scalar field E associated with the effective problem (Equation (6.5)) for different angles of incidence θ. 118

Figure 6.5: Total internal reflection of semi-guided plane waves at the step discontinuity of Figure 6.4. (a): Phase change ϕ of the guided wave upon reflection, associated Goos-Hänchen-shift Δ, and the effective boundary distance δ, as a function of the angle of incidence θ; estimates determined as outlined in Section 6.2 (scalar theory, ST) and Chapter 3 (transverse resonance, TR), in the later case by mode analysis of rib waveguides of different widths W. (b) Guided mode profiles of a rib of width $W = 4$ µm, constituted by two of the former step discontinuities, with associated mode indices m and mode angles θ.......................... 120
Figure 6.6: Simulations of tapered transitions of different length L. (a): Reflectance R, transmittance T, and the phase change upon reflection ϕ as a function of the angle of incidence θ, computed with the scalar approach of Section 6.2. (b): Configurations with total internal reflection, phase change upon reflection ϕ, lateral beam shift Δ and geometrical penetration depth δ versus the incidence angle θ, for a taper extension $L = 14.90$ µm (taper angle $0.5°$). 122

List of Tables

Table 5.1: Thicknesses for the different chip regions indicated in Figure 5.1 and the effective refractive indexes of the corresponding slabs, for TE and TM polarizations at λ_c. 90
Table 5.2: Design parameters chosen for the elliptical mirror and input waveguide. 94
Table 5.3: Parameters chosen for the polarization splitter slab. 99

Abstract

Raman spectroscopy is a powerful materials analysis technique used for identification of molecules residing near the surface of a sample. It has been successfully used for a broad range of application areas such as material science, biology, medicine and pharmacology owing to its numerous advantages. A traditional Raman measurement system is a complex setup, whose usage is limited due to its bulky and expensive components. If it would be possible to achieve a miniature Raman spectroscopic system with affordable costs by using integrated optics and electronics technology, it could be utilized further in the aforementioned applications. The goal of this PhD study is to realize small-scale optical components, which could be building blocks of a hand-held Raman measurement system, by using integrated optics. For this purpose, three different integrated optical modules in the SiON material platform are proposed in this thesis: Out of plane light turning mirrors, prism spectrometers and polarization splitters.

Integration of on-chip optics and electronics is an important aspect of realizing small scale Raman measurement devices. A highly efficient, quasi-TIR (total internal reflection) based 90° out of plane light turning mirror for hybrid flip-chip integration of SiON waveguides and CMOS-based photodiodes is proposed in this thesis. The mirror is defined at the interface between the optical structure and air by removal of Si from the substrate.

A spectrometer is a crucial part of Raman measurement systems. Here, we propose an integrated optical prism spectrometer, which utilizes dispersion effects in slab waveguides with two different thicknesses of the guiding layer, and which are connected adiabatically via vertical tapers. The principle and design aspects of the device are presented in detail. A theoretical analysis for the optical effects in the adiabatic transitions is also given. Furthermore, design, fabrication and characterization of a partially

optimized on-chip prism spectrometer, to be used for TE polarized light at a central wavelength of 850 nm, are described.

The design, fabrication and characterization of an on-chip polarization splitter (for a wavelength of 850 nm) to be used in polarized Raman measurements are also considered in this thesis. For the polarization splitting a waveguiding trench, with adiabatic transitions, is used.

Samenvatting

Raman spectroscopie is een krachtige methode voor de karakterisering van materialen die gebruikt kan worden voor de identificatie van moleculen nabij het oppervlak van een monster. Ze is met succes toegepast in een groot scala aan gebieden zoals materiaalwetenschappen, biologie, geneeskunde en farmacologie vanwege haar talrijke voordelen. Een traditionele Raman meetopstelling is betrekkelijk ingewikkeld en beperkt inzetbaar vanwege de omvang en prijs van de componenten. Indien het mogelijk zou zijn een miniatuur Ramanspectroscoop te realiseren voor een redelijke prijs dan zou dit nieuwe wegen openen voor bovengenoemde toepassingen. Het doel van dit promotieonderzoek is de realisatie van miniatuur optische componenten voor integratie in handzame Raman detectiesystemen. Hiertoe zijn drie verschillende, geïntegreerd optische modules, te realiseren in het SiON platform, voorgesteld in dit proefschrift: 90° uitkoppelspiegels, prisma spectrometers en polarisatiesplitsers.

De integratie van optische en elektronische chips is een belangrijk aspect bij de realisatie van miniatuur Raman detectiesystemen. Een zeer efficiënte 90° uitkoppelspiegel, gebaseerd op quasi TIR (totale interne reflectie), voor hybride flip-chipintegratie van SiON golfgeleiders en CMOS gebaseerde fotodiodes wordt voorgesteld in dit proefschrift. De spiegel wordt gedefinieerd door het grensvlak tussen de optische structuur en lucht door de verwijdering van Si van het substraat.

Een spectrometer is een essentieel onderdeel van een Ramandetectiesysteem. Hier stellen we een geïntegreerd optische prismaspectrometer voor die gebaseerd is op dispersie-effecten in planaire golfgeleiders met twee verschillende diktes voor de geleidende laag en die verbonden zijn via adiabatische overgangen. Het device principe en ontwerpaspecten komen uitgebreid aan bod. Ook wordt een theoretische analyse gegeven van het

gedrag van licht in genoemde adiabatische overgangen. Daarnaast worden ontwerp, fabricage en karakterisering van een gedeeltelijk geoptimaliseerde prismaspectrometer op chip, geschikt voor TE gepolariseerd licht met een centrale golflengte van 850 nm, beschreven.

Daarnaast zijn ontwerp, fabricage en karakterisering van een polarisatiesplitser op chip (voor een golflengte van 850 nm), geschikt voor gebruik in gepolariseerde Ramanmetingen, onderzocht. Voor de polarisatiesplitsing is een groef met adiabatische overgangen aangebracht in een planaire golfgeleider.

1 Introduction

A new era in material analysis was opened in 1928 by the discovery of Raman scattering [1, 2]. The phenomenon can be explained as inelastic scattering of photons from the molecules as a result of interaction between photons and vibrational modes of the molecules [3]. The frequency of the scattered photons depends on the energy needed to excite vibrational modes, which is specific to the type of the molecule. Therefore, spectral analysis of the scattered light, which is called Raman spectroscopy, can be used for identification of the molecules that are present in the sample. Nowadays, Raman spectroscopy is a widespread technique used in many fields such as chemistry, biology, medicine and archaeology [4-6]. In a Raman measurement system, the sample is illuminated with a monochromatic laser light and the spectrum of the back-scattered light is investigated for determination of the vibrational energies of the molecules. The distinct advantages of the Raman spectroscopy can be explained as follows: It can be applied for solid, liquid and gas phases of the materials [7]. It does not require any sample preparation. It is a non-destructive method (except for the intense illumination cases) and convenient for in-situ analysis of living tissues and biological samples [8].

A lot of variations of Raman measurements have been developed either to increase the collected Raman signal or to examine a specific property of the sample. Surface Enhanced Raman Spectroscopy (SERS) [9] and Coherent anti-Stokes Raman Spectroscopy (CARS) [10] can be considered as examples of developments related to signal enhancement. For the other group of variations, hyper Raman spectroscopy [11], resonance Raman spectroscopy [12] and polarized Raman spectroscopy [13] can be mentioned.

A traditional Raman measurement setup consists of a light source, excitation and collection optics (dichroic mirrors, objective lenses, filters, polarizers, etc.), wavelength (de)multiplexing devices (grating or prism based monochromators), detectors and electronics connected to a computer. The electronics may include low noise amplifiers for proper amplification of the detector output, high speed gates for suppression of strong fluorescence [14], lock in amplifiers for signal recovery, etc.; since the Raman signal collected from most of the samples is very weak. All these optics and electronics components mentioned above should be installed and operated by a well-trained technician on an optical table to obtain accurate Raman measurements. In order to increase the utilization of Raman spectroscopy, it should be available in a portable scale with a reasonable cost. There are portable Raman spectrometers with ~10 cm^{-1} resolution in 200-2000 cm^{-1} spectral range available in the market but they are still bulky (1-2 kg) and expensive since conventional optical components are employed in such systems [15]. The size and cost of such a device can be reduced further, if all the optics and electronics components mentioned above are fabricated by using micro/nano technology. The first steps towards miniaturisation of Raman spectroscopy is to realize light excitation, collection and wavelength (de)multiplexing with a very fine resolution (2.22 cm^{-1}) by integrated optics [16]; and high speed electronics monolithically integrated with Si photo-detectors can be implemented using standard CMOS technology [17]. Furthermore, these optics and electronics chips should be integrated in an efficient way to make an alignment-free and robust measurement device.

In this PhD study, which is supported by Dutch Technology Foundation (STW) through project Optical Lab in a Package (OptoLiP - 10051), two important aspects of realizing small scale Raman spectrometer devices are considered. First, quasi-total internal reflecting mirrors are developed for efficient integration of integrated optics chips and CMOS electronics chips, which have photo-diodes and processing electronics on it. The mentioned electronic chip is a subject of another PhD study (our partner in OptoLiP project) and it will not be discussed in this thesis. Second, integrated optical

spectrometers and polarization splitters are implemented to be used as the (de)multiplexing optics in the small size Raman measurement device.

The rest of this chapter is organized as follows: First, a conventional setup for Raman spectroscopy will be explained in Section 1.1. After that, the small scale Raman spectrometer system, the subject of this study, will be introduced in Section 1.2. The envisioned application of the study will be briefly mentioned in Section 1.3. The chapter will end by giving the outline of the thesis.

1.1 Conventional Raman Spectroscopy

The schematic of a conventional Raman spectroscopy system is shown in Figure 1.1 [18]. The setup is composed of a laser source, focusing optics, collection optics, monochromator, detector and detector electronics connected to a computer. Note that, an alternative system could be to use a dichroic mirror at the output of the laser source and to use the same lens for both the focusing and the collection of light [19].

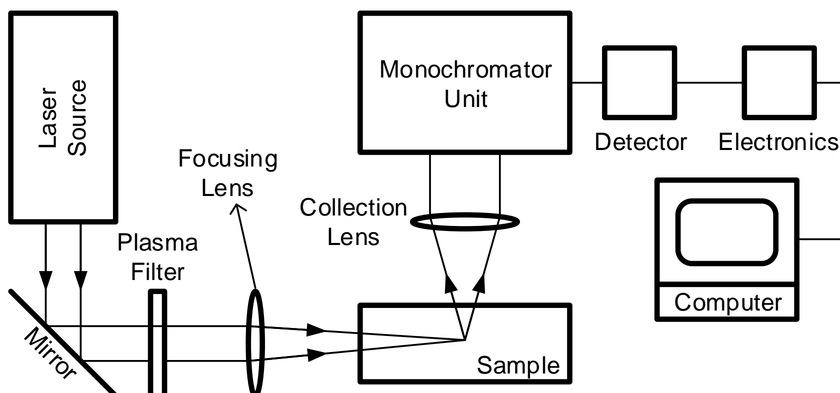

Figure 1.1: Schematic of conventional Raman spectroscopy system.

The operation of the system in Figure 1.1 can be explained as follows. The output of the laser source is reflected from the mirror and passes through a plasma filter, which is used for suppression of unwanted emission of the laser. Then, the filtered light is focused onto the sample by a focusing lens. The light scattered from the sample is transferred to the monochromator unit, which can be either a diffraction grating or a prism based system, through the collection lens. If the suppression of the monochromator for the excitation light is not enough, an edge filter can be used at the entrance of the monochromator [20]. Finally, the spectrum at the output of the monochromator is sent to the photo-detector that is connected to the computer controlled electronics for investigation of the spectrum.

A small scale version of this setup, which is the aim of OptoLiP project, can be built by miniaturizing certain components: (i) On-chip integrated optical lasers can be used as the excitation source [21, 22]; (ii) integrated optics spectrometers can be used as the monochromator unit [23]; (iii) series of photo-diodes implemented in CMOS technology together with its readout electronics can be used as the detector and readout electronics pair [17]. In this thesis, the integration of the on-chip optics and electronics components will be addressed. Furthermore, planar spectrometers and polarization splitters will be considered as it will be explained in the next section.

1.2 Small Scale Raman Spectrometer System

The schematic of the envisioned device can be seen in Figure 1.2. In the upper part, there is an electronics chip, which is implemented in standard CMOS technology, composed of a high speed (for gated operation) Si photo-detector and its corresponding readout electronics. As can be seen from the figure, the optical chip, which is fabricated on a separate substrate, is placed below the CMOS chip. The integrated optics spectrometer and polarization splitter could be placed on this optical chip that is implemented in SiON waveguide technology. There is a quasi-total internal reflection mirror at the end of the output waveguides of the optical components. The mirror, which

is defined at the interface between material of the optical structure and air, is used for directing the outputs of the various waveguides to corresponding photo-detectors. In the rest of this section, the light turning mirrors, integrated optics spectrometers and polarization splitters will be explained briefly.

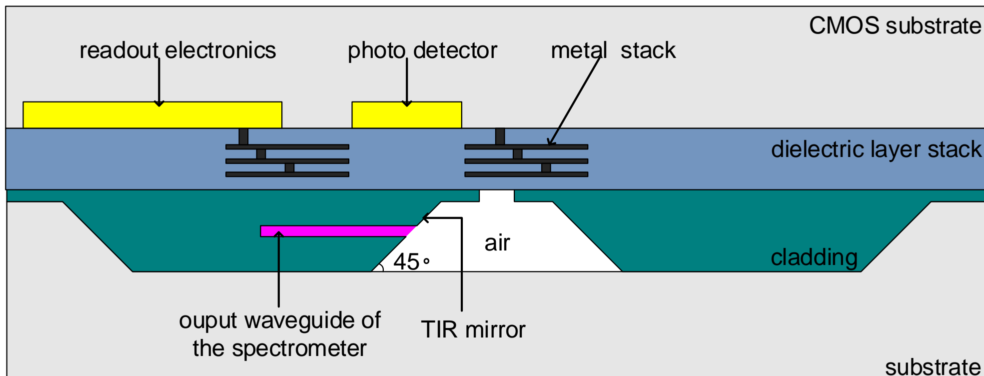

Figure 1.2: Schematic of the envisioned device.

1.2.1 Light Turning Mirror

In-plane and out of plane light turning integrated optical components have been studied for many years. The former one is essential for realization of compact integrated optical devices since it eliminates the necessity of large area waveguide bends [24-26]. The out of plane light turning components can be used in many applications such as optical disk pick up heads [27], board level interconnection of polymer waveguides and electronics on printed circuit boards [28] and chip level interconnection between optical and electronics chips [29]. Inclined exposure of photosensitive polymers is one of the methods for implementation of 45° angled light turning mirrors [30-33]. Another method is the use of micro hinge technology, which also enables precision alignment of the micro optical elements after fabrication [34]. Fluidic self-assembly and angle controlled etching methods are also used [35, 36]. These four variations have very complicated fabrication process technology. Diffraction based light turning structures are also used

as an out of plane light coupling method [37, 38]. However, these devices can only work for a limited wavelength range, which is defined by the grating period. In addition, total internal reflection (TIR) mirrors, which can be either fabricated by focused ion beam (FIB) milling or using special dicing blade for termination of waveguides, can be used [39-41]. However, these processes are not proper for batch fabrication.

In this thesis, we propose a new method to fabricate 45° mirrors in optical chips that enable high efficiency 90° out-of-plane light coupling to a flip-chip mounted electronic chip holding 2D photo-detector arrays with corresponding processing electronics.

1.2.2 Integrated Optics Spectrometer

In modern spectroscopy systems diffraction grating based monochromator units are widely used [42, 43]. Similarly, diffraction grating based devices are extensively utilized in integrated optics [44-46]. The most popular diffraction grating based micro-spectrometer device is the arrayed waveguide grating and it is used for many applications such as optical coherence tomography, Raman spectrometry, confocal microscopy, multi-wavelength light sources etc. [16, 47-53]. Planar grating structures are another alternative for this kind of integrated optics spectrometers [54-56]. In addition, MEMS based device are used as micro-spectrometers [57-59].

In this thesis, we proposed a prism based integrated optics spectrometer, which has an infinite free spectral range and no loss into any other order. The device is implemented in SiON waveguide technology [60-64] by using two masking steps in the fabrication. In such a spectrometer, dispersion is introduced by the wavelength dependence of the ratio between effective indices of the modes in a thin and a thick film. The transition area between the thin and thick film regions is chosen to be adiabatic to decrease the scattering losses. The device relies on ridge WGs for light transport and on parabolic mirrors for collimation and focusing.

1.2.3 Integrated Optics Polarization Splitter

A polarized Raman measurement provides information about the molecular orientation in addition to the molecular structure data that can be obtained in the vibrational Raman measurement [65]. The polarized measurement is done by polarizing the collected light from the sample before it couples into the spectrometer so that the acquired spectrum belongs only to a certain polarization [66, 67]. Integrated optics polarization splitters can be used for on-chip polarized Raman measurements.

On-chip polarization splitters are primarily considered for communication links with a polarization diversity scheme [68]. All variants of integrated optics based polarization splitters rely on the waveguide birefringence phenomenon [69]. There are different implementations of the splitter in the literature such as; birefringent directional couplers [70, 71], asymmetric Y junctions [72-74], interference based birefringent splitters [75, 76], grating based devices [77-79] and photonic crystal based devices [80].

In this thesis, an on-chip, adiabatically connected slab waveguide based polarization splitter will be introduced. The device is suitable to be fabricated by using the same technological steps developed for the on-chip prism based spectrometer. The device relies on ridge WGs for light transport and on an elliptical mirror for imaging of the input field onto the receiver waveguides.

1.3 Targeted Application

The envisioned application of the project is to determine the concentration of the natural moisturizing factor (NMF) in human skin [81]. Determination of NMF concentration in the skin is particularly important since a low NMF concentration is linked to a gene mutation predisposing a person for development of atopic dermatitis [82]. The NMF is formed in the lower part of the stratum corneum and most of the techniques for the determination of the NMF concentration are destructive. However, in vivo Raman

spectroscopy can be also be used for the determination of NMF concentration in non-destructive way. In this project, our target is the implementation of a small sized Raman spectroscopic system for in vivo measurement of NMF concentrations. For this application, the spectrometer should be operated with TE polarized light in a range of 100 nm around the central wavelength of λ_c = 850 nm with a channel spacing of $\Delta\lambda_{cs}$ = 5 nm. Note that, the scheme shown in Figure 1.2 is very suitable but not limited to the NMF application. It can also be used for other clinical and biological applications and in high speed communication links if the spectrometer and detector parameters are chosen accordingly. In the course of this research, essential integrated optical modules are developed and characterized but system integration is yet to be done.

1.4 Organization of the Thesis

In this study, three different integrated optics devices to be used for small scale Raman spectroscopy setup are designed, fabricated and characterized. They are (i) an integrated optics spectrometer in SiON technology, (ii) an integrated optics polarization splitter in SiON technology and (iii) light turning mirrors for integration of SiON waveguides with photo-detectors. An introduction is already given; the rest of the thesis is organized as follows.

In Chapter 2, we propose a new method to fabricate 45° mirrors in optical chips that enable high efficiency 90° out-of-plane light coupling to a flip-chip mounted electronic chip holding 2D photo-detector arrays with corresponding processing electronics.

In Chapter 3, we describe the performance and design aspects of a prism spectrometer produced with adiabatically connected slab WGs (having two different thicknesses), using principles of geometrical optics and diffraction theory.

In Chapter 4, we describe the design, fabrication and characterization of an on-chip prism spectrometer to be used for determining the natural moisturizing factor (NMF) concentration of the human skin.

In Chapter 5, we describe the design, fabrication and characterization of an on-chip polarization splitter implemented in the same technology used for the prism spectrometer.

In Chapter 6, we introduce the theoretical modeling for angled incidence of slab-guided waves to a tapered or step-like discontinuity by using a scalar 2-D Helmholtz equation.

The thesis ends with concluding remarks in Chapter 7. In this last chapter (Chapter 7) future directions are also mentioned.

1.5 References

[1] C. Raman and K. Krishnan, "A new type of secondary radiation," *Nature,* vol. 121, pp. 501-502, 1928.

[2] C. V. Raman, "A change of wave-length in light scattering," *Nature,* vol. 121, p. 619, 1928.

[3] R. L. McCreery, *Raman spectroscopy for chemical analysis* vol. 225: John Wiley & Sons, 2005.

[4] D. De Faria, S. Venâncio Silva, and M. De Oliveira, "Raman microspectroscopy of some iron oxides and oxyhydroxides," *Journal of Raman spectroscopy,* vol. 28, pp. 873-878, 1997.

[5] R. M. Jarvis and R. Goodacre, "Discrimination of bacteria using surface-enhanced Raman spectroscopy," *Analytical Chemistry,* vol. 76, pp. 40-47, 2004.

[6] B. Schrader, B. Dippel, I. Erb, S. Keller, T. Löchte, H. Schulz*, et al.*, "NIR Raman spectroscopy in medicine and biology: results and aspects," *Journal of Molecular Structure,* vol. 480, pp. 21-32, 1999.

[7] I. Beattie and J. Horder, "Gas-phase Raman spectroscopy of the trihalides of aluminium, gallium, and indium. The Raman spectra of solid and liquid indium

trichloride and tribromide," *Journal of the Chemical Society A: Inorganic, Physical, Theoretical,* pp. 2655-2659, 1969.

[8] I. Notingher, S. Verrier, H. Romanska, A. Bishop, J. Polak, and L. Hench, "In situ characterisation of living cells by Raman spectroscopy," *Journal of Spectroscopy,* vol. 16, pp. 43-51, 2002.

[9] C. L. Haynes, A. D. McFarland, and R. P. V. Duyne, "Surface-enhanced Raman spectroscopy," *Analytical Chemistry,* vol. 77, pp. 338 A-346 A, 2005.

[10] R. Begley, A. Harvey, and R. L. Byer, "Coherent anti-Stokes Raman spectroscopy," *Applied Physics Letters,* vol. 25, pp. 387-390, 1974.

[11] L. Ziegler, "Hyper-Raman spectroscopy," *Journal of Raman spectroscopy,* vol. 21, pp. 769-779, 1990.

[12] B. Robert, "Resonance Raman spectroscopy," *Photosynthesis research,* vol. 101, pp. 147-155, 2009.

[13] G. Duesberg, I. Loa, M. Burghard, K. Syassen, and S. Roth, "Polarized Raman spectroscopy on isolated single-wall carbon nanotubes," *Physical review letters,* vol. 85, p. 5436, 2000.

[14] P. Matousek, M. Towrie, C. Ma, W. Kwok, D. Phillips, W. Toner*, et al.*, "Fluorescence suppression in resonance Raman spectroscopy using a high-performance picosecond Kerr gate," *Journal of Raman Spectroscopy,* vol. 32, pp. 983-988, 2001.

[15] J. Jehlička, A. Culka, P. Vandenabeele, and H. G. Edwards, "Critical evaluation of a handheld Raman spectrometer with near infrared (785nm) excitation for field identification of minerals," Spectrochimica Acta Part A: Molecular and Biomolecular Spectroscopy, vol. 80, pp. 36-40, 2011.

[16] N. Ismail, B. Imran Akca, F. Sun, K. Wörhoff, R. M. De Ridder, M. Pollnau*, et al.*, "Integrated approach to laser delivery and confocal signal detection," *Optics letters,* vol. 35, pp. 2741-2743, 2010.

[17] S. Radovanovic, A.-J. Annema, and B. Nauta, "A 3-Gb/s optical detector in standard CMOS for 850-nm optical communication," *Solid-State Circuits, IEEE Journal of,* vol. 40, pp. 1706-1717, 2005.

[18] T. E. Conners and S. Banerjee, *Surface analysis of paper*: CRC Press, 1995.

[19] G. Puppels, M. Grond, and J. Greve, "Direct imaging Raman microscope based on tunable wavelength excitation and narrow-band emission detection," *Applied spectroscopy,* vol. 47, pp. 1256-1267, 1993.

[20] P. L. Flaugh, S. E. O'Donnell, and S. A. Asher, "Development of a new optical wavelength rejection filter: demonstration of its utility in Raman spectroscopy," *Applied spectroscopy,* vol. 38, pp. 847-850, 1984.

[21] D. Lo, L. Shi, J. Wang, G.-X. Zhang, and X.-l. Zhu, "Zirconia and zirconia-organically modified silicate distributed feedback waveguide lasers tunable in the visible," *Applied physics letters,* vol. 81, pp. 2707-2709, 2002.

[22] M. Pollnau, D. Geskus, E. H. Bernhardi, K. van Dalfsen, K. Worhoff, and R. M. de Ridder, "Highly efficient solid-state waveguide lasers," in *Advanced Solid-State Photonics*, 2012, p. AM5A. 1.

[23] N. Ismail, F. Sun, K. Wörhoff, A. Driessen, R. M. de Ridder, and M. Pollnau, "Integrated arrayed waveguide grating spectrometer for measuring Raman spectra," in *The European Conference on Lasers and Electro-Optics*, 2011, p. CH5_4.

[24] Y. Tang, W. Wang, T. Li, and Y. Wang, "Integrated waveguide turning mirror in silicon-on-insulator," *Photonics Technology Letters, IEEE,* vol. 14, pp. 68-70, 2002.

[25] P. Buchmann and H. Kaufmann, "GaAs single-mode rib waveguides with reactive ion-etched totally reflecting corner mirrors," *Journal of lightwave technology,* vol. 3, pp. 785-788, 1985.

[26] J. S. Jensen and O. Sigmund, "Systematic design of photonic crystal structures using topology optimization: Low-loss waveguide bends," *Applied Physics Letters,* vol. 84, pp. 2022-2024, 2004.

[27] L. Lin, J. Shen, S. Lee, and M. Wu, "Realization of novel monolithic free-space optical disk pickup heads by surface micromachining," *Optics letters,* vol. 21, pp. 155-157, 1996.

[28] A. L. Glebov, M. G. Lee, S. Aoki, D. Kudzuma, J. Roman, M. Peters*, et al.*, "Integrated waveguide micro-optic elements for 3D routing in board-level optical interconnects," in *Integrated Optoelectronic Devices 2006*, 2006, pp. 61260N-61260N-11.

[29] Y. Ishii, S. Koike, Y. Arai, and Y. Ando, "SMT-compatible large-tolerance" OptoBump" interface for interchip optical interconnections," *Advanced Packaging, IEEE Transactions on,* vol. 26, pp. 122-127, 2003.

[30] X. Dou, X. Wang, H. Huang, X. Lin, D. Ding, D. Z. Pan, *et al.*, "Polymeric waveguides with embedded micro-mirrors formed by Metallic Hard Mold," *Optics express,* vol. 18, pp. 378-385, 2010.

[31] M. Immonen, M. Karppinen, and J. K. Kivilahti, "Fabrication and characterization of polymer optical waveguides with integrated micromirrors for three-dimensional board-level optical interconnects," *Electronics Packaging Manufacturing, IEEE Transactions on,* vol. 28, pp. 304-311, 2005.

[32] F.-G. Tseng and H.-T. Hu, "A novel micro optical system employing inclined polymer mirrors and Fresnel lens for monolithic integration of optical disk pickup heads," in *TRANSDUCERS, Solid-State Sensors, Actuators and Microsystems, 12th International Conference on, 2003*, 2003, pp. 599-602.

[33] D.-Y. Oh, K. Gil, S. S. Chang, D. K. Jung, N. Y. Park, and S. S. Lee, "A tetrahedral three-facet micro mirror with the inclined deep X-ray process," *Sensors and Actuators A: Physical,* vol. 93, pp. 157-161, 2001.

[34] M. C. Wu, L.-Y. Lin, S.-S. Lee, and K. Pister, "Micromachined free-space integrated micro-optics," *Sensors and Actuators A: Physical,* vol. 50, pp. 127-134, 1995.

[35] U. Srinivasan, M. A. Helmbrecht, C. Rembe, R. S. Muller, and R. T. Howe, "Fluidic self-assembly of micromirrors onto microactuators using capillary forces," *Selected Topics in Quantum Electronics, IEEE Journal of,* vol. 8, pp. 4-11, 2002.

[36] M. Kagami, A. Kawasaki, and H. Ito, "A polymer optical waveguide with out-of-plane branching mirrors for surface-normal optical interconnections," *Journal of Lightwave Technology,* vol. 19, p. 1949, 2001.

[37] T. Shiono and H. Ogawa, "Planar-optic-disk pickup with diffractive micro-optics," *Applied optics,* vol. 33, pp. 7350-7355, 1994.

[38] S. M. Schultz, E. N. Glytsis, and T. K. Gaylord, "Volume grating preferential-order focusing waveguide coupler," *Optics letters,* vol. 24, pp. 1708-1710, 1999.

[39] H. Ximen, R. DeFreez, J. Orloff, R. Elliott, G. Evans, N. Carlson*, et al.*, "Focused ion beam micromachined three-dimensional features by means of a digital scan," *Journal of Vacuum Science & Technology B,* vol. 8, pp. 1361-1365, 1990.

[40] R. Yoshimura, M. Hikita, M. Usui, S. Tomaru, and S. Imamura, "Polymeric optical waveguide films with 45 mirrors formed with a 90 V-shaped diamond blade," *Electronics Letters,* vol. 33, pp. 1311-1312, 1997.

[41] A. L. Glebov, J. Roman, M. G. Lee, and K. Yokouchi, "Optical interconnect modules with fully integrated reflector mirrors," *Photonics Technology Letters, IEEE,* vol. 17, pp. 1540-1542, 2005.

[42]A. Weber, S. P. Porto, L. E. Cheesman, and J. J. Barrett, "High-resolution Raman spectroscopy of gases with cw-laser excitation," *JOSA,* vol. 57, pp. 19-27, 1967.

[43] M. Pelletier, "Raman spectroscopy using an echelle spectrograph with CCD detection," *Applied spectroscopy,* vol. 44, pp. 1699-1705, 1990.

[44] T. Suhara and H. Nishihara, "Integrated optics components and devices using periodic structures," *Quantum Electronics, IEEE Journal of,* vol. 22, pp. 845-867, 1986.

[45] R. Wolffenbuttel, "State-of-the-art in integrated optical microspectrometers," *Instrumentation and Measurement, IEEE Transactions on,* vol. 53, pp. 197-202, 2004.

[46] A. Yariv and M. Nakamura, "Periodic structures for integrated optics," *IEEE Journal of Quantum Electronics,* vol. 13, pp. 233-253, 1977.

[47] B. Akca, C. Doerr, G. Sengo, K. Wörhoff, M. Pollnau, and R. de Ridder, "Broad-spectral-range synchronized flat-top arrayed-waveguide grating applied in a 225-channel cascaded spectrometer," *Optics express,* vol. 20, pp. 18313-18318, 2012.

[48] B. Akca, V. Nguyen, J. Kalkman, N. Ismail, G. Sengo, F. Sun*, et al.*, "Toward spectral-domain optical coherence tomography on a chip," *Selected Topics in Quantum Electronics, IEEE Journal of,* vol. 18, pp. 1223-1233, 2012.

[49] I. Akca, N. Ismail, F. Sun, D. V. Nguyen, J. Kalkman, T. G. van Leeuwen*, et al.*, "Integrated arrayed waveguide grating spectrometer for on-chip optical

coherence tomography," in *Conference on Lasers and Electro-Optics*, 2010, p. JWA66.

[50] N. Ismail, F. Sun, G. Sengo, K. Wörhoff, A. Driessen, R. M. De Ridder*, et al.*, "Improved arrayed-waveguide-grating layout avoiding systematic phase errors," *Optics express,* vol. 19, pp. 8781-8794, 2011.

[51] V. D. Nguyen, B. I. Akca, K. Wörhoff, R. M. De Ridder, M. Pollnau, T. G. van Leeuwen*, et al.*, "Spectral domain optical coherence tomography imaging with an integrated optics spectrometer," *Optics letters,* vol. 36, pp. 1293-1295, 2011.

[52] H. Sanjoh, H. Yasaka, Y. Sakai, K. Sato, H. Ishii, and Y. Yoshikuni, "Multiwavelength light source with precise frequency spacing using a mode-locked semiconductor laser and an arrayed waveguide grating filter," *Photonics Technology Letters, IEEE,* vol. 9, pp. 818-820, 1997.

[53] Y. Sano and T. Yoshino, "Fast optical wavelength interrogator employing arrayed waveguide grating for distributed fiber Bragg grating sensors," *Lightwave Technology, Journal of,* vol. 21, pp. 132-139, 2003.

[54] J. Soole, A. Scherer, H. LeBlanc, N. Andreadakis, R. Bhat, and M. Koza, "Monolithic InP/InGaAsP/InP grating spectrometer for the 1.48–1.56 μm wavelength range," *Applied Physics Letters,* vol. 58, pp. 1949-1951, 1991.

[55] S. Janz, A. Balakrishnan, S. Charbonneau, P. Cheben, M. Cloutier, A. Delâge*, et al.*, "Planar waveguide echelle gratings in silica-on-silicon," *Photonics Technology Letters, IEEE,* vol. 16, pp. 503-505, 2004.

[56] J. Soole, A. Scherer, H. Leblanc, N. Andreadakis, R. Bhat, and M. Koza, "Monolithic InP-based grating spectrometer for wavelength-division multiplexed systems at 1.5 μm," *Electronics letters,* vol. 27, pp. 132-134, 1991.

[57] C. Ataman, H. Urey, and A. Wolter, "A Fourier transform spectrometer using resonant vertical comb actuators," *Journal of micromechanics and microengineering,* vol. 16, p. 2517, 2006.

[58] F. Lee, G. Zhou, H. Yu, and F. S. Chau, "A MEMS-based resonant-scanning lamellar grating Fourier transform micro-spectrometer with laser reference system," *Sensors and Actuators A: Physical,* vol. 149, pp. 221-228, 2009.

[59] R. Wolffenbuttel, "MEMS-based optical mini-and microspectrometers for the visible and infrared spectral range," *Journal of Micromechanics and Microengineering,* vol. 15, p. S145, 2005.

[60] K. Wörhoff, R. M. Ridder, P. V. Lambeck, and A. Driessen, "Silicon oxynitride in integrated optics," 1998.

[61] P. V. Lambeck and K. Worhoff, "SiON technology for integrated optical sensors," in *Photonics Fabrication Europe*, 2003, pp. 195-204.

[62] K. Worhoff, E. Klein, G. Hussein, and A. Driessen, "Silicon oxynitride based photonics," in *Transparent Optical Networks, 2008. ICTON 2008. 10th Anniversary International Conference on*, 2008, pp. 266-269.

[63] K. Worhoff, P. V. Lambeck and A. Driessen, "Design, tolerance analysis, and fabrication of silicon oxynitride based planar optical waveguides for communication devices," *Journal of Lightwave Technology,* vol. 17, p. 1401, 1999.

[64] F. Sun, A. Driessen, and K. Wörhoff, "High performance optical waveguides based on boron and phosphorous doped silicon oxynitride," in *OPTO*, 2010, pp. 760403-760403-9.

[65] M. Amer, *Raman spectroscopy for soft matter applications*: John Wiley & Sons, 2009.

[66] A. C.-T. Ko, L.-. Choo-Smith, M. Hewko, M. G. Sowa, C. Dong, and B. Cleghorn, "Detection of early dental caries using polarized Raman spectroscopy," *Optics express,* vol. 14, pp. 203-215, 2006.

[67] N. Ismail, L.-P. Choo-Smith, K. Wörhoff, A. Driessen, A. Baclig, P. Caspers, *et al.*, "Raman spectroscopy with an integrated arrayed-waveguide grating," *Optics letters,* vol. 36, pp. 4629-4631, 2011.

[68] M. R. Watts, M. Qi, T. Barwicz, L. Socci, P. T. Rakich, E. P. Ippen*, et al.*, "Towards integrated polarization diversity: design, fabrication and characterization of integrated polarization splitters and rotators," in *Optical Fiber Communication Conference*, 2005, p. PDP11.

[69] M. Okuno, A. Sugita, K. Jinguji, and M. Kawachi, "Birefringence control of silica waveguides on Si and its application to a polarization-beam splitter/switch," *Lightwave Technology, Journal of,* vol. 12, pp. 625-633, 1994.

[70] I. Kiyat, A. Aydinli, and N. Dagli, "A compact silicon-on-insulator polarization splitter," *Photonics Technology Letters, IEEE,* vol. 17, pp. 100-102, 2005.

[71] H. Maruyama, M. Haruna, and H. Nishihara, "TE-TM mode splitter using directional coupling between heterogeneous waveguides in LiNbO 3," *Lightwave Technology, Journal of,* vol. 13, pp. 1550-1554, 1995.

[72] R. M. de Ridder, A. Sander, A. Driessen, and J. H. Fluitman, "An integrated optic adiabatic TE/TM mode splitter on silicon," *Lightwave Technology, Journal of,* vol. 11, pp. 1806-1811, 1993.

[73] Y. Shani, C. H. Henry, R. Kistler, R. Kazarinov, and K. Orlowsky, "Integrated optic adiabatic polarization splitter on silicon," *Applied Physics Letters,* vol. 56, pp. 120-121, 1990.

[74] S. M. Garner, V. Chuyanov, S.-S. Lee, A. Chen, W. H. Steier, and L. R. Dalton, "Vertically integrated waveguide polarization splitters using polymers," *Photonics Technology Letters, IEEE,* vol. 11, pp. 842-844, 1999.

[75] J. M. Hong, H. H. Ryu, S. R. Park, J. W. Jeong, S. G. Lee, E.-H. Lee*, et al.*, "Design and fabrication of a significantly shortened multimode interference coupler for polarization splitter application," *Photonics Technology Letters, IEEE,* vol. 15, pp. 72-74, 2003.

[76] L. Soldano, A. DeVreede, M. Smit, B. Verbeek, E. Metaal, and F. Groen, "Mach-Zehnder interferometer polarization splitter in InGaAsP/InP," *IEEE photonics technology letters,* vol. 6, pp. 402-405, 1994.

[77] D. Taillaert, H. Chong, P. I. Borel, L. H. Frandsen, R. M. De La Rue, and R. Baets, "A compact two-dimensional grating coupler used as a polarization splitter," *Photonics Technology Letters, IEEE,* vol. 15, pp. 1249-1251, 2003.

[78] E. Simova and I. Golub, "Polarization splitter/combiner in high index contrast Bragg reflector waveguides," *Optics express,* vol. 11, pp. 3425-3430, 2003.

[79] W. N. Ye, D.-X. Xu, S. Janz, P. Waldron, P. Cheben, and N. G. Tarr, "Passive broadband silicon-on-insulator polarization splitter," *Optics letters,* vol. 32, pp. 1492-1494, 2007.

[80] V. Zabelin, L. Dunbar, N. Le Thomas, R. Houdré, M. Kotlyar, L. O'Faolain*, et al.*, "Self-collimating photonic crystal polarization beam splitter," *Optics letters,* vol. 32, pp. 530-532, 2007.

[81] P. Caspers, G. Lucassen, and G. Puppels, "Combined in vivo confocal Raman spectroscopy and confocal microscopy of human skin," *Biophysical journal,* vol. 85, pp. 572-580, 2003.

[82] S. Kezic, G. O'Regan, N. Yau, A. Sandilands, H. Chen, L. Campbell*, et al.*, "Levels of filaggrin degradation products are influenced by both filaggrin genotype and atopic dermatitis severity," *Allergy,* vol. 66, pp. 934-940, 2011.

2 Light Turning Mirrors for Hybrid Integration of SiON-based Optical Waveguides and Photo-detectors[1]

For hybrid integration of an optical chip with an electronic chip containing photo-diodes and processing electronics, light must be coupled from the optical to the electronic chip. This chapter presents a method to fabricate quasi-total-internal-reflecting mirrors on an optical chip, placed at an angle of 45° with the chip surface, that enable 90° out-of-plane light coupling between flip-chip bonded chips. The fabrication method utilizes a metal-free, parallel process and is fully compatible with conventional fabrication of optical chips. The mirrors are created using anisotropic etching of 45° facets in a Si substrate, followed by fabrication of the optical structures. After removal of the mirror-defining Si structures by isotropic etching, the obtained interfaces between optical structure and air direct the output from optical waveguides to out-of-plane photo-detectors on the electronic chip, which is aimed to be flip-chip mounted on the optical chip.

2.1 Introduction

In recent years, waveguide based integrated optical devices have been used in many applications, such as telecommunication, optical spectroscopy, biological sensing, and signal processing in medical imaging [1-3]. Usually the waveguide output signals are measured using photo-diodes (PDs) that

[1] This chapter has been published as: F. Civitci, G. Sengo, A. Driessen, M. Pollnau, A. Annema, and H.J.W.M. Hoekstra, "Light turning mirrors for hybrid integration of SiON-based optical waveguides and photo-detectors," Optics Express, vol. 21, pp. 24375-24384, 2013.

may be dedicated to applications such as time gating in spectroscopic research or in diagnostics. In particular, for (high-resolution) spectroscopy the signals from a large number of different channels must be measured simultaneously, which can be done most conveniently with 2D arrays of PDs. Monolithic integration of the latter to the Si substrate of an optical chip has several disadvantages: (i) the PDs and their electronic processing circuitry must be fabricated first, implying that the temperature budget to fabricate the optical structures is limited to about 400 °C, whereas higher-temperature process steps are often needed, such as low-pressure chemical vapor deposition (LPCVD) and reflow of deposited layers; (ii) fabrication of PDs and their electronic processing circuitry on each optical chip would be far more expensive than processing a CMOS chip that includes densely packed PDs and electronics which could be flip-chip mounted on an optical die due to the large area occupied by the optical chip compared to the CMOS chip.

This chapter describes a method to fabricate 45° mirrors in optical chips that enable highly efficient 90° out-of-plane light coupling to a flip-chip mounted electronic chip holding 2D PD arrays with corresponding processing electronics. The fabrication process for these mirrors is suitable for batch production and has a thermal budget of 900 °C. The mirror is defined by anisotropic etching of a 45° facet in the Si substrate. After waveguide fabrication the mirror is formed by locally removing the Si facet at the interface between the truncated optical waveguide and air. In the next section, this device is introduced and the mirror performance is estimated by simulations. Then the fabrication process steps toward realizing the mirror are described. Finally, the results of structural device characterization and experimental performance of the fabricated devices are presented.

2.2 Device design and calculated performance

This section introduces the composition and principle of the proposed device and discusses the choices related to the configuration of the device. Simulation results to estimate the mirror performance are presented.

Figure 2.1 displays the cross section of the 45° mirror structure. The device is composed of a single-mode SiON channel waveguide, which is embedded in BPSG and continues, at the mirror side of the structure, on a 45°-angled

thin Si_3N_4 layer, which has an interface with air at the opposite side of the SiON layer. This thin Si_3N_4 layer prevents the exchange of molecules at the interface between the buffer layer and the Si substrate, which otherwise might cause an ill-defined Si surface. Furthermore, calculations show that, with an optimized thickness of 100 nm, it leads to a decrease of the functional loss of the mirror by about 3%, thanks to the increased refractive-index contrast between the optical structure and air. Here, functional loss is defined as the loss in reflectance due to the fact that the mirror is ideally not fully reflecting (quasi-TIR). The device can also be configured such that the waveguide is truncated before it reaches the mirror interface, but calculations show that the functional loss would be increased. The working principle of this device is as follows. Owing to the abrupt directional change of the waveguide (45°) the light carried by the SiON waveguide is no longer confined and is reflected upwards via the nitride layer and its interface with air, where quasi-TIR takes place. This behavior is confirmed by 2D finite-difference time-domain (FDTD) calculations.

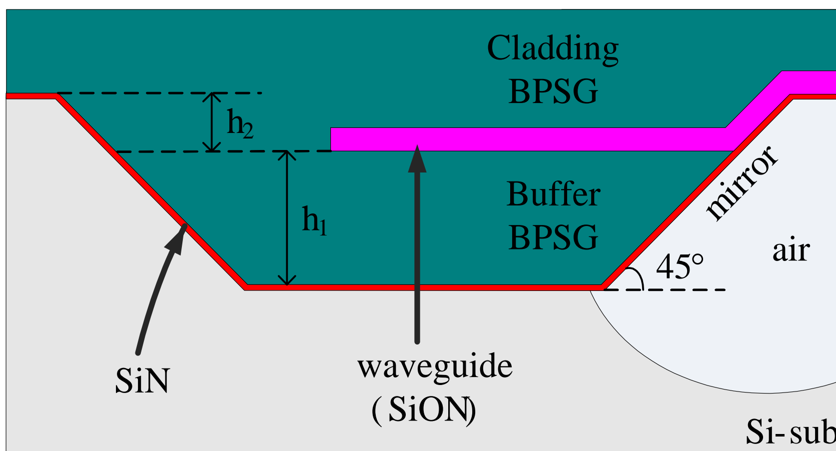

Figure 2.1: Cross-sectional view of the proposed device

These mirrors are designed to be used in SiON waveguide technology in an application [4] using a central wavelength of λ_c = 850 nm. In principle, also a ridge waveguide geometry can be used; however, it is not possible to use

ridge waveguides in combination with a BPSG buffer layer, because outgassing in the subsequent high-temperature annealing step would lead to damage to the BPSG layer if fully covered with a SiON layer.

The waveguides are designed to be single-mode at λ_c, since single modality is required by most of the potential applications. The total height ($h_1 + h_2$) of the pyramidal mirror structures is of critical concern in the waveguide design: the next section explains that this height should be as small as possible to ease the fabrication process. On the other hand, there is a lower limit to the buffer-layer height (h_1) because of radiation losses to the substrate, which can be minimized by increasing the vertical confinement of the waveguide mode.

We choose the waveguide width to be 1 μm, which is the minimum width that can be achieved with our fabrication process. Selecting the minimum width allows for a maximum waveguide height, which, in turn, maximizes the vertical confinement. The refractive index and thickness of the SiON layer are selected to be 1.585 and 600 nm, respectively, for achieving a single-mode waveguide at λ_c. The BPSG buffer height h_1 is set to 3.5 μm, which ensures less than 10^{-4} dB/cm radiation losses to the substrate, according to mode-solver calculations based on the finite-element method. This estimated loss is much smaller than propagation losses of slab SiON layers, which is 0.2 dB/cm for visible light [8]. The vertical distance between the buffer layer and uppermost point of the mirror (h_2) is selected to be 1.5 μm, which provides a proper overlap between waveguide mode and mirror surface. Consequently, the total height of the pyramids is about 5 μm.

The application of thermally grown SiO_2, which is normally used as a buffer material [5], would lead to deformation of the Si micro-structures. Therefore, we selected BPSG (instead of undoped SiO_2) as the buffer and cladding material, as it does not lead to deformation of the Si micro-structures and can be reflown at a temperature of 900 °C for removal of as-deposited defects. This reflow is required for the removal of voids or slits which arise during plasma-enhanced chemical vapor deposition (PECVD) near elevated micro-structures [6]; it defines the thermal budget of the device.

Performance of the proposed mirrors is estimated from the somewhat simplified structure in Figure 2.2(a) by calculating the field profile after reflection of the Fourier components corresponding to the channel

waveguide mode from the SiON-SiN-air structure. The simplification consists of the assumption that the 45° angled wall is fully covered with a 600 nm thick SiON layer, i.e., it is assumed that the modal power is incident from the SiON layer onto the mirror. The resulting calculated far-field-intensity distribution for transverse-electric (TE) polarization is displayed in Figure 2.2(b), indicating that the intensity profile is not symmetric along the vertical direction. This asymmetrical behavior occurs, because Fourier components corresponding to downward-travelling beams have a (slightly) different angle of incidence upon the reflecting layer than more upwardly directed beams and, hence, a lower reflection coefficient. Although most of the Fourier components undergo TIR, some are not totally reflected, which leads to a decrease in efficiency. The calculated functional loss of the mirror is 7% for TE polarization and 10% for transverse-magnetic (TM) polarization.

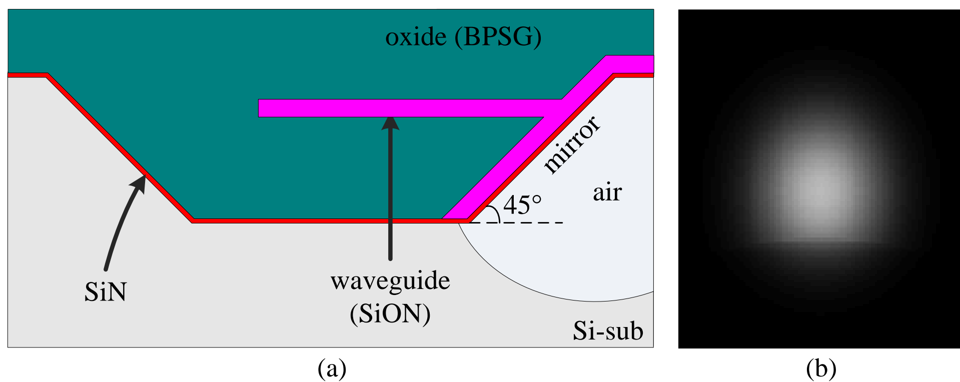

Figure 2.2: (a) Cross-section of the simplified mirror structure used in the simulation and (b) calculated intensity profile at the far field for TE polarization.

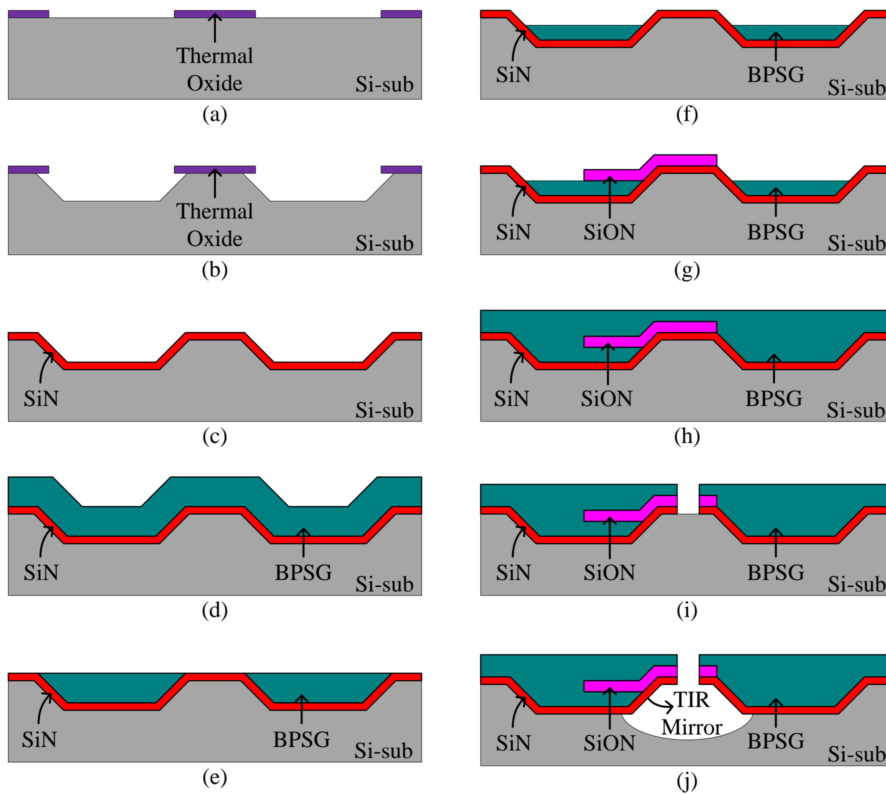

Figure 2.3: Wafer cross-sections corresponding to different steps in the fabrication process flow.

2.3 Fabrication process

The wafer cross-sections after different steps in the fabrication process flow are shown in Figures 2.3(a)–2.3(j). Each step is briefly discussed below.

a. The fabrication process starts with the growth of 200 nm thick thermal silicon oxide (dry oxidation at 1100 ˚C) to be used as an anisotropic Si etching mask. Subsequently, the oxide is patterned by buffered HF (BHF) etching.

b. 5 µm (= $h_1 + h_2$) deep anisotropic etching of the (100) Si wafer is performed by use of a solution of TMAH and Triton-x-100. When applying this etchant, the

{110} plane is etched slower than the {100} plane, resulting in an etch stop at the {110} planes, if the edges in the oxide mask are aligned parallel to {110} planes [7]. The desired wall angle of 45° is achieved with this etch stop, because the angle between the wafer surface and {110} planes is 45°. Concentration and temperature of the etchant are optimized in order to minimize the roughness of etched {110} surfaces. In this study, 75 ppm of Triton-x-100 is added to a 25% TMAH solution and the etching process is carried out at 80 °C (the etch rate of the solution is ~0.35 µm/min.). A short BHF dip is carried out before TMAH etching in order to remove native oxide on Si. Figure 2.4 shows the SEM pictures of Si structures that are etched with the optimized process. As can be seen from Figure 2.4(b), the etched {110} surfaces are not perfectly smooth. The effect of this roughness is investigated by performing an experiment in which a laser beam at 632 nm wavelength is focused onto the etched Si surface and the light reflected from this surface is compared with the light reflected from a bare Si wafer surface. The measurements show that the roughness diminishes the reflectance of the beam by the Si surface by only 4%. The details of this measurements are explained in Appendix A1.

c. The fabrication process is continued by removal of the thermal oxide in BHF. Then a 100 nm thick stoichiometric SiN layer is deposited by LPCVD.

d. Hereafter, a thick boron-phosphorous-doped silica glass (BPSG) film is grown using PECVD, to serve as the buffer layer. The deposition is carried out at 350 ˚C with a chamber pressure of 2000 mT and RF power of 200 W (13.56 MHz). Four different gasses are used in the process; SiH_4 and N_2O for oxide formation and diluted PH_3 and B_2H_6 for doping. The thickness of this layer should be at least 5 µm, which is equal to the etch depth defined in the anisotropic Si etch step, to obtain a flat surface using a chemical-mechanical polishing (CMP) step. Since as-deposited BPSG layers grown by this method contain voids and slits at the corners of pre-patterned layers (elevated Si structures in our case), post-deposition annealing at 900 °C during 16 hours right after deposition of the BPSG layer is required to overcome this problem. Figure 2.5. Shows SEM photos of (a) as-deposited and (b) annealed BPSG layer on Si, which has 45° angled walls. Both photos were taken after a quick BHF dip for making the slits and voids prominent. It can be seen from the figure that annealed BPSG is free of slits and voids.

e. The surface topology, resulting after the anisotropic Si etch step, is maintained after the BPSG deposition. To obtain a flat surface, CMP is performed after annealing the BPSG layer, because non-annealed BPSG would be attacked by the cleaning solution (RCA-2) used after the CMP process. The polishing is done with 0.4 psi back pressure, head and table speeds of 30 rpm and 42 rpm, respectively (removal rate is ~0.8 μm/min). Additional elevated Si dummy structures were processed to improve uniformity of the removal rate of this polishing process over the full wafer [8]. These dummy structures had the same dimensions as the mirrors and were distributed over the full wafer, except for the area occupied by the waveguides.

f. Subsequently, the BPSG is thinned in a BHF solution, such that a 3.5 μm thick buffer layer remains between guiding SiON layer and Si substrate.

g. This step is followed by deposition and patterning of the core SiON layer which has a refractive index of 1.585. The deposition is done by PECVD (deposition rate is 47 nm/min) at a substrate temperature of 300 ˚C, chamber pressure of 650 mT, an RF power of 60 W (187.5 kHz) and a gas mixture of 600 sccm N_2, 600 sccm SiH_4 and 315 sccm (can be changed for refractive index tuning) N_2O. The etching of the SiON layer is done by RIE (etch rate is ~40 nm/min) at a substrate temperature of 20 ˚C, an RF power of 350 W, a chamber pressure of 28 mT and a gass mixture of 100 sccm CHF_3 and 2 sccm O_2.

h. Next, the cladding BPSG layer is deposited, annealed, and polished by CMP under the same process conditions as applied to the buffer BPSG.

i. Then isotropic Si etching holes are introduced on top of the elevated Si structures by using RIE (the same process conditions as mentioned in g).

j. Finally, through these holes the isotropic Si etching is performed. In this step, gas-phase XeF_2 etching (30 sec cycles are used with expansion chamber pressure of 3 T) is used to selectively remove Si. The selectivity to Si_3N_4 and annealed BPSG layers should be high in order not to diminish the surface quality of the TIR mirrors. It is known that XeF_2 etching of Si_3N_4 is at least 25 times slower than that of Si [9]. Our experimental results show that XeF_2 etching of Si is 1500 times faster than that of annealed BPSG.

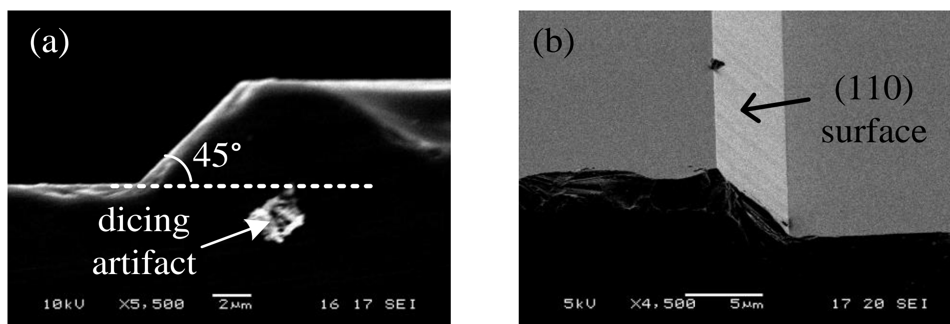

Figure 2.4: (a) SEM cross section and (b) top view of Si structures etched by the optimized Si anisotropic etchant.

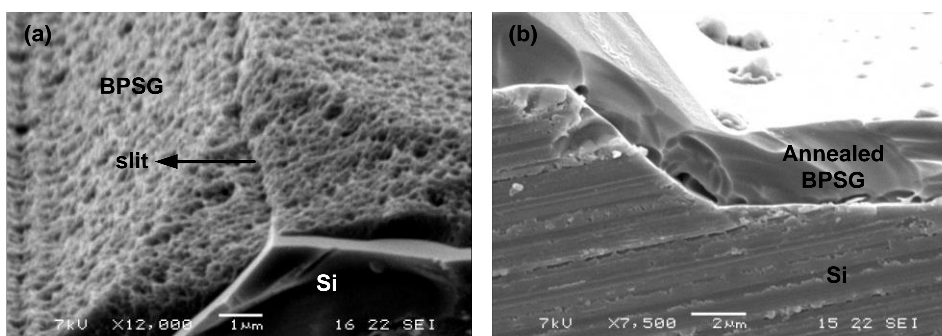

Figure 2.5: SEM photos of (a) as-deposited and (b) annealed BPSG layer on Si, which has 45° angled walls. Both photos were taken after a quick BHF dip for making the slits and voids prominent.

2.4 Characterization

This section discusses the structural features of the fabricated device and experimental results related to device performance.

2.4.1 Structural characterization

Figure 2.6(a) shows a SEM picture of a cross section of the wafer through one of the pyramidal structures, which is obtained by dicing the sample through the center of the elevated Si structure and then etching the sample in XeF_2 to remove the Si from the edge of the chip. After XeF_2 treatment, the part of the BPSG layer at the edge of the chip is suspended in air. The bright particles in the image are an artifact of the dicing process. The angle between the mirror and the wafer surface is measured from this figure to be 45°, as expected. Figure 2.6(b) displays a top-view photograph of a device that is composed of four mirrors with corresponding waveguides. Circular openings in the four mirror pyramids can be identified. These pyramids are surrounded by elevated Si dummy structures. The circular features around the four mirror pyramids correspond to the area etched during the XeF_2 treatment. Also visible in Figure 2.6(b) at the transition between the buffer BPSG and cladding BPSG is a step that is formed because of the unwanted etching (approximately 30 nm in total) of the SiN layer in two different steps of the fabrication process: (i) BHF thinning of the buffer BPSG layer (Figure 2.3(f)) and (ii) SiON patterning (Figure 2.3(g)). Such a transition between BPSG layers is not visible at those pyramids that are not etched in XeF_2, which is attributed to the insufficient image contrast in those areas. Considering the relatively low measured functional loss (see below), apparently this undesired defect hardly reduces the mirror performance. Nevertheless, the step can be avoided by modifying the fabrication process as follows: (i) TEOS oxide which does not interact with the substrate can be used instead of BPSG as the buffer layer, making the thin SiN layer between buffer layer and substrate unnecessary, thereby eliminating the unwanted etching issue in the BHF thinning step; (ii) ridge waveguides can be used instead of channel waveguides to prevent over-etching in the SiON patterning step.

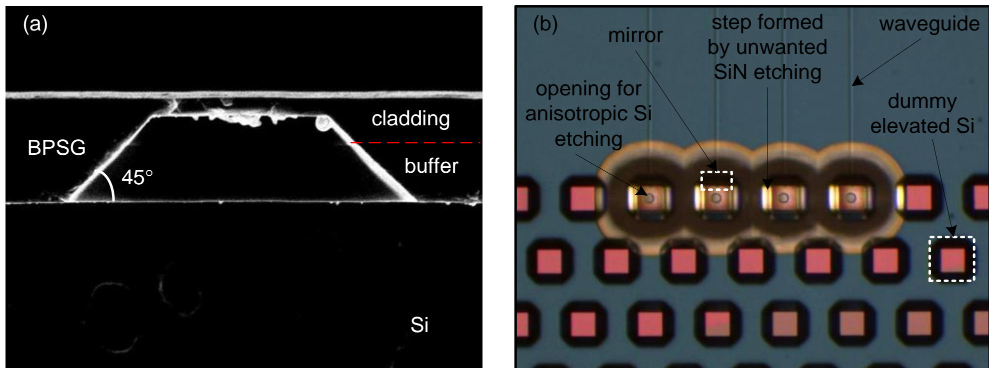

Figure 2.6: (a) SEM cross section obtained by dicing the sample through the center of an elevated Si structure and (b) top view photograph of part of the fabricated chip showing four mirrors with corresponding waveguides as well as dummy pyramids.

2.4.2 Optical characterization

Figure 2.7 shows a schematic of the optical setup used for estimating the mirror performance. Laser light at a wavelength of 850 nm is coupled into a single-mode optical fiber. Light at the output of this fiber is collimated by a thin lens, polarized by a polarization beam splitter (PBS) and a $\lambda/2$-plate, and coupled to the waveguide by a microscope objective lens. The light propagating in the waveguide is reflected from the mirror, illuminates a diffusive screen 1 cm away from it, and the resulting image is captured by a camera connected to a computer. Figures 2.8(a) and 2.8(b) show the measured far-field intensity patterns of TE- and TM-polarized light, respectively. The graphs in Figures 2.8(c) and 2.8(d) show the calculated, measured, and ideal (corresponding to 100% reflection from an ideal mirror) curves of the irradiance, integrated over y, along the x-axis for both polarizations. The graphs show that the measured intensity profile for TE polarization is narrower than the simulated one although they are similar in shape. For TM polarization, the steep intensity decrease in the left half of the calculated graph is less pronounced in the experimental curve. This discrepancy can be attributed to the simplifications made in the calculation.

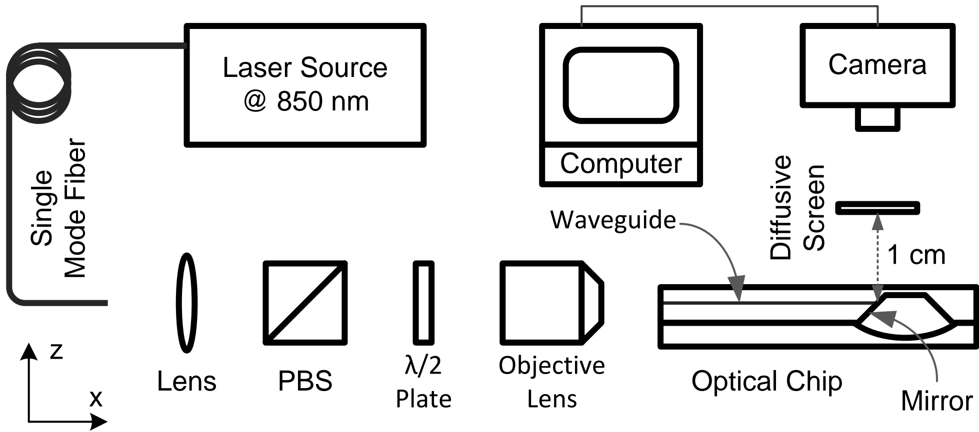

Figure 2.7: Schematic of the optical setup used for measuring the mirror performance.

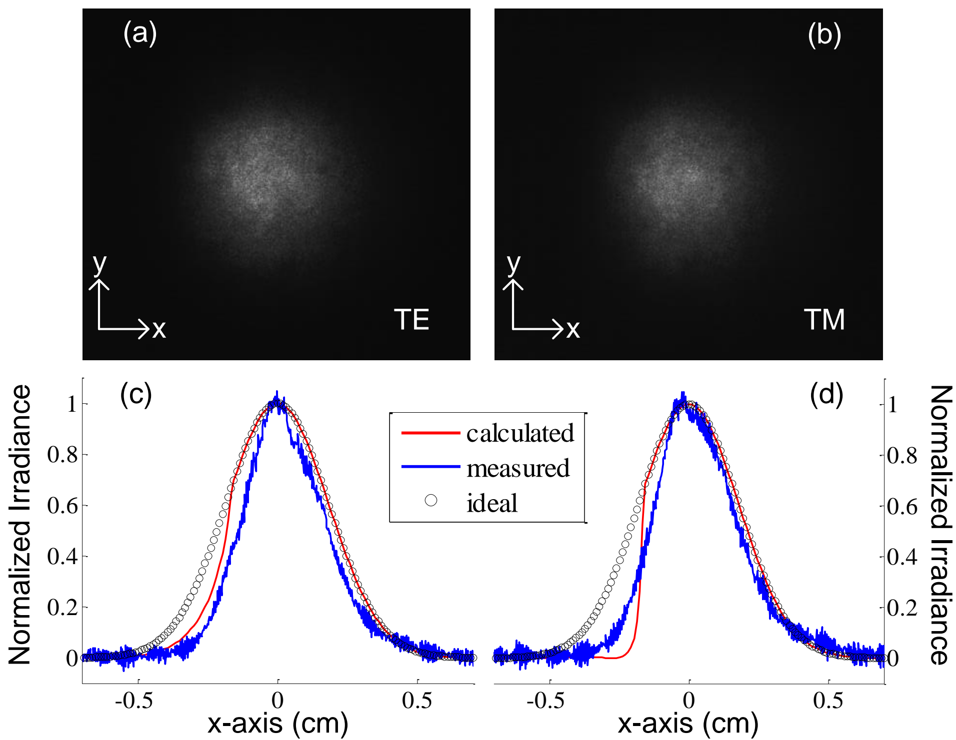

Figure 2.8: Measured far-field beam profiles for (a) TE- and (b) TM-polarized light. The graphs show the calculated, measured, and ideal irradiance integrated over y, along the x-axis for (c) TE and (d) TM polarizations.

Two methods are applied to measure the functional loss of the mirror. In the first method, we compare the mirror output corresponding to a specific waveguide with that of the same waveguide after the mirror has been removed by dicing. Differences in the excitation efficiencies of the waveguide during the measurements with and without mirror are accounted for by monitoring the light in the same part of the waveguide with a camera and determining the optical power propagating in the waveguide. This process is repeated a number of times to correct for statistical fluctuations, resulting in a functional loss of the fabricated mirror for TE polarization of 5% with 4% RMS deviation, which agrees well with the calculated value of 7%, and for TM polarization of 4% with 4% RMS deviation, which is considerably lower than the value of 15% obtained from calculations. This discrepancy is mainly due to simplifications made in the calculations and the possible roughness at the output of the waveguide after dicing, which could decrease the power coupling to the detector from the waveguide.
In the second method, which appears to be more reliable (owing to the aforementioned roughness of the waveguide output), the functional loss is determined from the measured far-field irradiance. Figures 2.8(c) and 2.8(d) show that the right-hand sides of the calculated and ideal irradiance curves exactly overlap. This implies that the reflectance of the plane waves corresponding to the right-hand side of the calculated curves is unity. Assuming unity reflectance for the measured curves, we fit the right-hand side (plus a small fraction of the left-hand side such that R^2, which is defined as the ratio of the sum of squares of the regression (SSR) and the total sum of squares (SST), is maximized, see Figure 2.9) of these curves to the Gaussian function

$$I = Ae^{-2\frac{(x-x_c)^2}{w^2}} . \tag{2.1}$$

where A, x_c, and w are peak value, position of the peak, and width of the Gaussian function, respectively. The used data range for fitting corresponds to the Fourier components of the far field of the beam reflected according to TIR from the mirror. Figure 2.9 shows the experimental and fitted curves for the irradiance, as well as the part of the experimental data used for fitting and the resulting fit. So, the curve fitting enables the identification of the

non-reflected part of the light, which is assumed to be the only source of loss. The efficiency is calculated by dividing the area below the measured curve by the area below the fitted curve. The results show that the functional loss of the fabricated mirror for TE polarization is 6.2%, while for TM polarization it is 17.8%, which agrees well with the calculated values of 7% and 15% for TE and TM polarization, respectively.

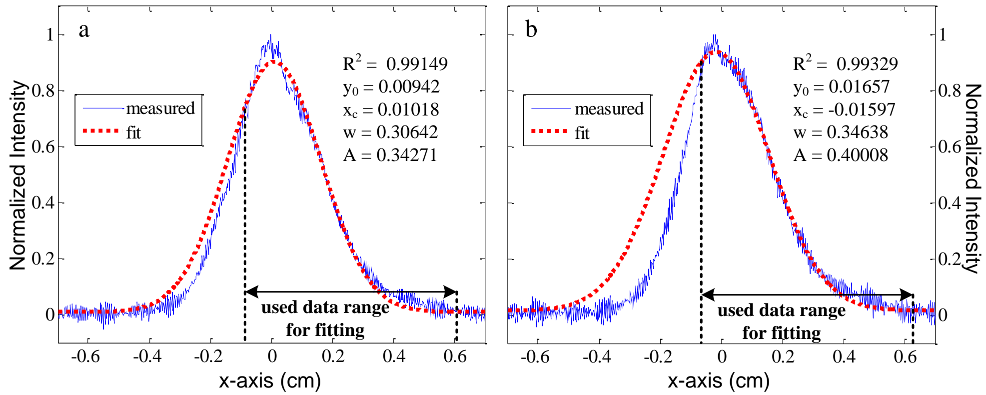

Figure 2.9: Measured and fitted irradiance, integrated over y, along the x-axis for (a) TE and (b) TM polarization.

2.5 Conclusions

Quasi-TIR-based 90° out-of-plane light-turning mirrors with high efficiency for hybrid flip-chip integration of SiON waveguides and CMOS-based photodiodes have been fabricated by use of a newly designed technology flow. Experimental results obtained from the fabricated device show that the experimental functional loss of the mirrors are 6.2% for TE and 17.8% for TM polarization, reasonably close to the values obtained from approximate calculations being 7% and 15%, respectively.

2.6 References

[1] B. Chmielak, M. Waldow, C. Matheisen, C. Ripperda, J. Bolten, T. Wahlbrink, M. Nagel, F. Merget, and H. Kurz, "Pockels effect based fully integrated, strained silicon electro-optic modulator," Opt. Express **19**, 17212–17219 (2011).

[2] S. V. Pham, M. Dijkstra, A. J. F. Hollink, L. J. Kauppinen, R. M. de Ridder, M. Pollnau, P. V. Lambeck, and H. J. W. M. Hoekstra, "On-chip bulk index concentration and direct label-free protein sensing utilizing an optical grated-waveguide cavity," Sens. Actuator B **174**, 602–608 (2012).

[3] B. I. Akca, L. Chang, G. Sengo, K. Wörhoff, R. M. de Ridder, and M. Pollnau, "Polarization independent enhanced-resolution arrayed waveguide grating used in spectral domain optical low coherence reflectometry," IEEE Photon. Technol. Lett. **24**, 848–850 (2012).

[4] N. Ismail, L. P. Choo-Smith, K. Wörhoff, A. Driessen, A. C. Baclig, P. J. Caspers, G. J. Puppels, R. M. de Ridder, and M. Pollnau, "Raman spectroscopy with an integrated arrayed-waveguide grating," Opt. Lett. **36**, 4629–4631 (2011).

[5] K. Wörhoff, P. V. Lambeck, and A. Driessen., "Design, tolerance analysis, and fabrication of silicon oxynitride based planar optical waveguides for communication devices," J. Lightwave Technol. **17**, 1401–1407 (1999).

[6] F. Sun, M. G. Hussein, K. Wörhoff, G. Sengo, and A. Driessen, "B/P doping in application of silicon oxynitride based integrated optics," in *Proceedings of The European Conference on Lasers and Electro-Optics 2009*, (European Physical Society, Mulhouse, 2009), paper: CE5_1.

[7] D. Resnik, D. Vrtacnik, U. Aljancic, M. Mozek, and S. Amon, "The role of triton surfactant in anisotropic etching of {110} reflective planes on (100) silicon," J. Micromech. Microeng. **15**, 1174–1183 (2005).

[8] D. O. Ouma, D. S. Boning, J. E. Chung, W. G. Easter, V. Saxena, S. Misra, and A. Crevasse, "Characterization and modeling of oxide chemical-mechanical polishing using planarization length and pattern density concepts," IEEE Trans. Semicond. Manuf. **15**, 232–244 (2002).

[9] K. R. Williams and R. S. Muller, “Etch rates for micromachining processing,” J. Micromech. Syst. **5**, 256–269 (1996).

3 Design of a Prism Spectrometer based on Adiabatically Connected Waveguide Slabs

The device principle of a prism-based on-chip spectrometer for TE polarization is introduced. The spectrometer utilizes the modal dispersion in planar waveguides in a lay-out with slab regions having two different thicknesses of the guiding layer. The set-up uses parabolic mirrors, for the collimation of light of the input waveguide and focusing of the light to the receiver waveguides, which utilize total internal reflection at the interface between two such regions. These regions are connected adiabatically to prevent unwanted mode conversion and loss at the edges of the prism. The structure can be fabricated with two wet etching steps. The chapter presents basic theory and a general approach for device optimization. The latter is illustrated with a numerical example assuming SiON technology.

3.1 Introduction

In the early years (70's) of Integrated Optics (IO), the theory and experimental characterization of slab waveguide based components, such as thin film lenses, prisms, reflectors and polarization splitters were extensively investigated [1]. The design of these components is straightforward since the propagation of light waves in these slabs can be described by geometrical optics in 2D and diffraction theory [2]. Furthermore, slab waveguide fabrication is not a complicated process. In spite of these advantages, only a small number of device principles, which combines one or more of these components, have been implemented, like prism based mode separators [3], grating based de-multiplexers [4] and thermo-optic switches [5].

Wavelength (de)multiplexing planar devices, or micro-spectrometers, have a large potential for applications in telecommunication and sensing [6-10]. In planar implementations the device principle is often based on IO variants of bulky grating spectrometers like an arrayed waveguide grating (AWG) [6], employing diffractionless propagation in waveguides and compact Echelle gratings [9, 10]. In addition, cascaded Mach-Zehnder interferometers and ring resonators are being used [11, 12] as micro-spectrometers.

In this chapter, we describe the performance and design aspects of a prism spectrometer produced with adiabatically connected slab waveguides (having two different thicknesses), using principles of geometrical optics and diffraction theory. The advantages of employing a prism based spectrometer are the absence of extra diffraction orders, thus avoiding spectral overlap of the different orders and loss into other orders, and the relative simplicity of fabrication. In such a spectrometer dispersion is introduced by the differing wavelength dependence for effective indices of modes in thin and thick films. The device relies on ridge waveguides for light transport and on parabolic mirrors for collimation and focusing. A design strategy will be presented and illustrated via a numerical example with TE polarized light in a range of 100 nm around the central wavelength of λ_c = 850 nm with a channel spacing of 5 nm by using SiON waveguide technology.

The rest of this chapter is organized as follows. First, we will introduce the principle and basic theory related to the prism spectrometer in Section 3.2. The part of the imaging theory discussed in this section is well usable for other spectrometer types, such as AWGs. It is followed by an explanation of the design of this device in Section 3.3, where also a numerical example is given. The chapter ends with conclusions (Section 3.4).

3.2 Prism Spectrometer: Principle and Basic Theory

A schematic picture of the considered prism spectrometer device is shown in Figure 3.1. It is composed of an input waveguide, a collimating mirror, a prism slab, a focusing mirror and receiver waveguides, corresponding to

different wavelengths. The picture in the middle of Figure 3.1 with output of 3 adjacent waveguides shows the important spectrometer parameters that will be used in this chapter, such as 3 dB bandwidth ($\Delta\lambda$), channel spacing ($\Delta\lambda_{cs}$), adjacent channel cross-talk (ACCT), global cross-talk (CT) and Loss.

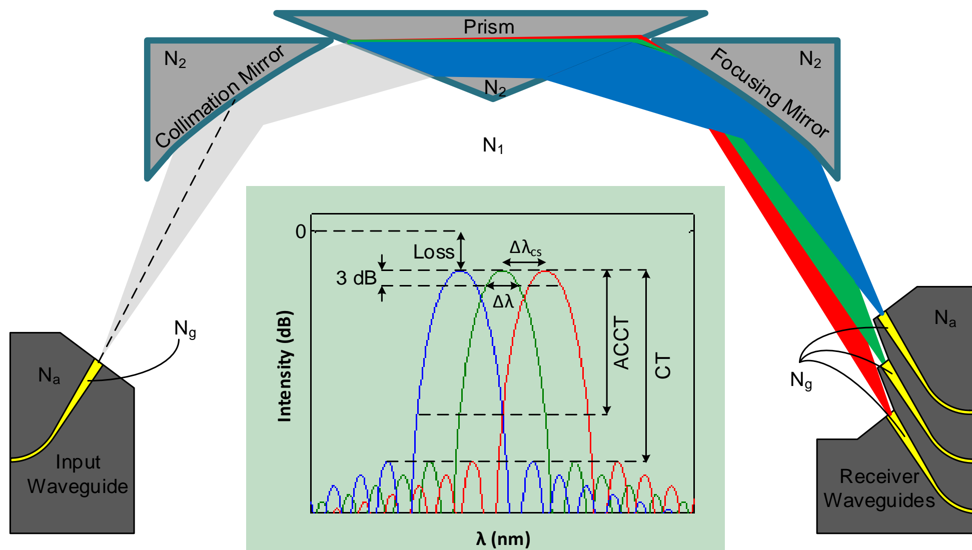

Figure 3.1: Schematic of the considered prism spectrometer. The white and dark grey areas correspond to thick and thin slabs, respectively. Ridge waveguides are indicated by yellow lines. The inset illustrates schematically the relation of the output intensities to the parameters that characterize the device performance. Regions with different thicknesses of the guiding layer are connected adiabatically via vertical tapering.

The proposed device is planned to be implemented in SiON waveguide technology by using a Si_3N_4 (nitride) layer sandwiched between buffer and cladding SiO_2 (oxide). Patterning of nitride will be done by using a BHF wet etching process in two different process steps; (i) definition of input/output waveguides and (ii) definition of prism and mirror trenches. A sacrificial oxide layer is deposited on top of the nitride layer in the latter in order to

achieve the adiabatic transition on the edges of patterned structures. The main advantage of using an adiabatic transition of the layer thickness, and thus the effective refractive index, between the slab waveguides is the elimination of partial reflection of the incident light at the edges of the prism [1]. With such a tapering the angle of incidence to the prism can be chosen relatively high (just below the critical angle θ_{crit}), which is beneficial for a larger angular dispersion (enabling a smaller device area for a given resolution) as discussed below (Section 3.2.1), without increasing insertion loss and the amount of stray light in the spectrometer. These adiabatic transitions also affect the modal phase shift upon total internal reflection (TIR) by the mirrors and so the imaging onto the receiver waveguides. This will be elaborated in Section 3.2.4. In the following subsections we will present the basic theory for the set-up, relevant for device design and operation.

3.2.1 Prism

A sketch of the prism is shown in Figure 3.2, where also the ray trajectory is indicated and used symbols are introduced. The angular dispersion is defined by

$$\sigma_2' = \partial\sigma_2/\partial\lambda, \tag{3.1}$$

where λ is the (vacuum) wavelength. The angular dispersion can be rewritten as follows: Diffraction at the prism interfaces is governed by Snell's law. For the first interface, this can be written as

$$\sin\sigma_1 = D\sin\alpha_1, \tag{3.2}$$

where we defined $D = N_2/N_1$, with N_1 and N_2 the effective indices of the thick and thin slabs, respectively. Note that the following inequality holds for $N_2 < N_1$. Knowing that σ_1 does not depend on λ, the derivative of the right hand side of Equation (3.2) with respect to λ gives

$$\frac{\partial \alpha_1}{\partial \lambda} = \alpha_1' = -\frac{D'}{D} \tan \alpha_1, \tag{3.3}$$

with $D' = \partial D / \partial \lambda$. The relation between α_1 and α_2 can be found from the geometry leading to

$$\alpha_1 + \alpha_2 = \eta. \tag{3.4}$$

By combining Equations (3.3) and (3.4) we arrive at

$$\frac{\partial \alpha_2}{\partial \lambda} = \alpha_2' = \frac{D'}{D} \tan \alpha_1. \tag{3.5}$$

If Snell's law is applied to the second interface it follows

$$\sin \sigma_2 = D \sin \alpha_2, \tag{3.6}$$

from which the following can be obtained by taking the derivative,

$$\sigma_2' = D' \frac{\sin \alpha_2}{\cos \sigma_2} + D\alpha_2' \frac{\cos \alpha_2}{\cos \sigma_2}. \tag{3.7}$$

The above equality can be rewritten by inserting Equation (3.5) into Equation (3.7) as follows:

$$\sigma_2' = D' \left(\frac{\sin \alpha_2}{\cos \sigma_2} + \frac{\sin \alpha_1 \cos \alpha_2}{\cos \alpha_1 \ \sin \sigma_2} \right). \tag{3.8}$$

For later use we consider the angular dispersion, assuming minimum deviation ($\alpha_1 = \alpha_2, \sigma_1 = \sigma_2 = \sigma$), which can be re-written from Equation (3.8) into:

$$\sigma_2' = \frac{D'}{D}(\tan\sigma + 1). \tag{3.9}$$

The deviation angle δ can be expressed as

$$\delta = \eta - \sigma_1 - \sigma_2 = \alpha_1 + \alpha_2 - \sigma_1 - \sigma_2, \tag{3.10}$$

where we used Equation (3.4). The minimum deviation condition implies that $\partial(\sigma_1 + \sigma_2)/\partial\sigma_1 = 0$, or $\partial\sigma_2/\partial\sigma_1 = -1$. As a consequence of the latter relative angles don't change, for light at a certain wavelength with an angle of incidence near σ_1, traversing the prism. Consequently, beams don't change shape while traveling through the prism, provided that there is no truncation of the beam (by the limited dimensions of the prism) and the angular dependence of the transmission is small (as accomplished by the adiabatic transitions; see Section 3.3.2 for a numerical example). So, if a Gaussian beam having a transverse field distribution according to

$$A(\rho) = A_1 e^{(-\rho^2 2\ln 2/W^2)}, \tag{3.11}$$

with W the full width at half maximum (FWHM) and ρ the transverse coordinate, is traversing the prism its shape will be unaltered if truncation of the beam by the limited prism size can be neglected. The far field of that beam is then given by [13]

$$F(u) = \int_{-\infty}^{+\infty} A(\rho) e^{iu\rho} d\rho = F_0 e^{-u^2 2\ \ln 2/\Delta u^2}, \tag{3.12}$$

where we assumed a time dependence $e^{i\omega t}$ of all electromagnetic fields, and u is defined as $u \equiv kN_1 \sin\phi$ with k the wavenumber and ϕ the diffraction angle. The FWHM of the far field intensity is given by $\Delta u = 4\ln 2\,/W$ and corresponds to $\Delta\phi = \Delta u/(kN_1)$. An expression for the resolution can now

be derived as follows. Assuming that two equally shaped peaks corresponding to different wavelengths are resolved if these are separated by the FWHM it follows

$$\Delta\phi = \sigma_2' \Delta\lambda_f, \qquad (3.13)$$

or

$$\Delta\lambda_f = 4 \ln 2 / (\sigma_2' W k N_1). \qquad (3.14)$$

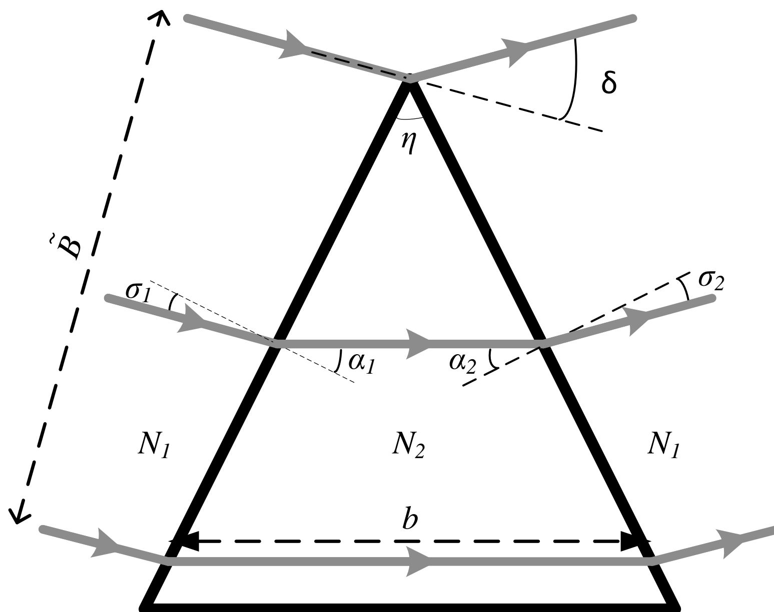

Figure 3.2: Schematic (top view) of a generic prism structure.

In the above $\Delta\lambda_f$ is the FWHM of the far field intensity, assuming that it is not affected by truncation of the Gaussian beam due to the finite size of the prism (or mirrors). As will be discussed in Section 3.2.3 truncation effects are almost negligible if the truncation parameter ς is larger than ~3, with ς defined by $\tilde{B} = \varsigma W$ ($\tilde{B}$ is the width of the output/input beam as defined in Figure 3.2). If we assume, for example, that $\varsigma = 4$, substitute $\tilde{B} = \varsigma W$ into Equation (3.14) it follows from the geometry, with $D' \equiv \partial D/\partial\lambda$:

$$\Delta\lambda_f = \frac{8\ln 2D}{D'\tilde{B}kN_1(1+\tan\sigma)} , \tag{3.15}$$

where $\sigma \equiv \sigma_1 = \sigma_2$ and $\alpha_1 = \alpha_2$, assuming the minimum deviation condition. It is seen from the above that σ should be chosen as large as possible for a smaller device area (so for smaller $\tilde{B}$) and thus optimization of the resolution for given beam width, $\tilde{B}$), comes down to optimizing the quantity $R = N_1D'/D$.

It is seen from Equation (3.9) that for a large angular dispersion (and so for higher resolution) the angle of incidence on the prism facet should be as large as possible (analogue to what we concluded above using Equation (3.15)). On the other hand it should of course not exceed the critical angle for TIR, θ_{crit}, defined by

$$\theta_{crit} = \sin^{-1}(N_2/N_1). \tag{3.16}$$

It is found, as illustrated in Section 3.3.2 with an example, that with proposed adiabatic transitions between areas with a thick and a thin guiding layer there is an abrupt transition from very low reflectance at angles of incidence below θ_{crit} to (of course) full reflectance for angles of incidence above θ_{crit}. This can be employed by choosing

$$\sigma \leq \theta_{crit}, \tag{3.17}$$

such that σ_2 is below θ_{crit} for the whole considered wavelength region.

For later use we give the inequality holding at minimum deviation

$$\partial\delta\ /\partial\sigma|_{MD} > 0, \tag{3.18}$$

which can be derived using the definition for δ and Snell's law (Equation (3.1)) together with the inequality $N_2 < N_1$.

3.2.2 Parabolic Mirrors

Both mirrors, which are identical owing to the assumed symmetric implementation, are parabolic mirrors, which can be designed using Fermat's principle. Figure 3.3(a) shows the schematic of a parabolic collimation/focusing mirror, which has a collimated beam parallel to the *x*-axis. In this figure θ_l and θ_h are the incidence/reflection angles for the start and end points of the mirror respectively, $\tilde{B}$ is the width of the output/input beam and $\gamma\ (= 2\theta_h - 2\theta_l)$ is the angle between the outermost rays and the focal point is chosen to be origin. Fermat's principle dictates that the total optical path lengths between the focal point and points at an arbitrary cross section of the collimated beam, say, at $x = x_h$, are all the same. Denoting the mirror coordinates by (*x*,*y*) it follows:

$$\sqrt{x^2 + y^2} + (x_h + x) = d_0, \tag{3.19}$$

which can be rewritten by defining a new variable $c_m \equiv d_0 - x_h$$c_m = d_o\text{-}x_n$ as

$$\sqrt{x^2 + y^2} - x = c_m. \tag{3.20}$$

Next we will show, for later use, that the parabolic mirror (shape and size) is fully defined by the quantities $\tilde{B}$, θ_l and γ. Using Equation (3.20) and the relation

$$y = -x\tan(2\theta)\,, \tag{3.21}$$

where θ is the incidence angle of an arbitrary point on the mirror, it follows (assuming that $\cos(2\theta) < 0$, as in the device considered by us in Section 3.2)

$$x\left(\sqrt{1+(\tan(2\theta))^2}-1\right) = -\frac{x[1+\cos(2\theta)]}{\cos(2\theta)} = c_m, \tag{3.22}$$

which enables us to write:

$$x = \frac{x_l[1+\cos(2\theta_l)]\cos(2\theta)}{[1+\cos(2\theta)]\cos(2\theta_l)}. \tag{3.23}$$

Then, with Equation (3.21) and $y_h = y_l + \tilde{B} = -x_h\tan(2\theta_h)$ we find

$$y_l = -\tilde{B} - x_h\tan(2\theta_h) = -x_l\tan(2\theta_l). \tag{3.24}$$

Substitution of x_h according to Equation (3.23), with $(x,\theta) = (x_h,\theta_h)$, into the second equality of Equation (3.24) leads after simple manipulations to:

$$\tilde{B} = -2\cos\theta_l\sin(\gamma/2)\,x_l/(\cos(\theta_l+\gamma/2)\cos(2\theta_l)), \tag{3.25}$$

from which the full mirror curve can indeed be derived, also using Equations (3.23) and (3.21).

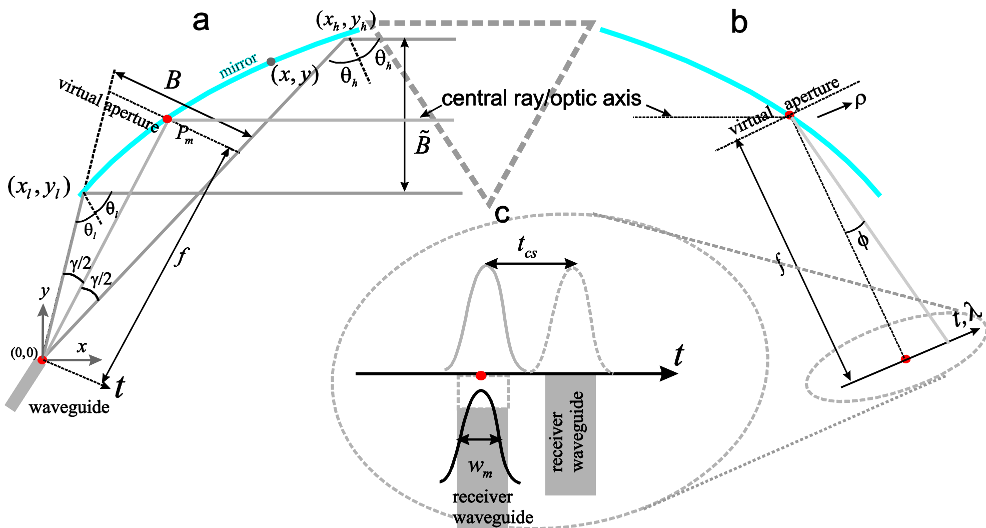

Figure 3.3: Schematic pictures of the collimation mirror (a), the focusing mirror (b) and the focal area (c), introducing the used symbols.

In order to obtain a simplifying picture of the working of the mirror a virtual aperture and a focal length are introduced (see Figure 3.3(a) and (b)). The former is defined by a line piece through the point P_m, which is the intersection point of the bisector of the outermost rays and the mirror curve, perpendicular to the corresponding ray and with end points defined by the (extrapolated) outermost rays. The distance between point P_m and the focus is called f, the focal length. The width of the virtual aperture, B, is equal to the (maximum) beam width, $\tilde{B}$, with a small relative error proportional to γ^2. Note that the point P_m of the collimation mirror (as well as of the focusing mirror) is chosen to be on the optical axis and that it does not correspond to the middle of the parallel beam coming from the input mirror. As a consequence, assuming a symmetrical mode coming from the input waveguide, the field in the collimated beam will be (slightly) asymmetric. But, the asymmetry of this beam (which travels without changing shape

through the prism) is fully compensated by the identical focusing mirror. So, for a certain wavelength, the image of the input field near the receiver waveguides can be considered as the focused far field of the input field, truncated by the mirror owing to a finite (virtual) aperture, as defined by the size of the mirror.

The mirror is designed for the central wavelength λ_c. Light at a nearby wavelength is diffracted by the prism and focusing mirror at a different angle. The latter leads to a small change in focal distance, as indicated in Figure 3.1, and to aberrations, as follows from numerical calculations using ray tracing according to geometrical optics, corresponding to small blurring of the central spot. It is found from geometrical optics that the blurring effect becomes smaller for smaller angles of incidence θ (which then should be chosen to be just above the critical angle) and smaller values of the angle γ.

3.2.3 Imaging of the Input Field

We consider the propagation through the prism spectrometer of the modal field at a certain wavelength, λ_0, launched by the input waveguide. In case of ideal lensing and no truncation by the prism (or mirrors) the light is imaged onto the focal line without any change of shape and at a position according to its wavelength. The imaging process, now including the truncation, can be described numerically by taking the Fourier transform of the transverse distribution of the launched field (to calculate the far field), truncation of the far field, taking the complex conjugate of the result (to account for the lensing effect) followed by again taking the Fourier transform. The above can be expressed analytically as follows.

The transverse distribution of the far field of the launched mode, E_m is given by [13]

$$F(u) = \frac{1}{\sqrt{2\pi}} \int_{-\infty}^{\infty} E_m(t) e^{iut}\, dt, \tag{3.26}$$

where $u \equiv kN_1 \sin\phi$, t is a local coordinate and ϕ is the diffraction angle. The shape of the field E_m is defined by the V parameter [14] given by

$$V = kh\sqrt{N_g^2 - N_a^2} \tag{3.27}$$

with h the width of the waveguide and N_g and N_a are the effective indices of the planar structures corresponding to the guiding and adjacent waveguide sections, respectively. The image in the focal area then follows from [13]

$$E_{im}(t) = \frac{1}{\sqrt{2\pi}} \int_{-\varsigma\Delta u/2}^{\varsigma\Delta u/2} F^*(u) e^{iut}\, du \tag{3.28}$$

with Δu the FWHM of $|F(u)|^2$ and ς is the truncation parameter. The following relations hold:

$$B\left(= \tilde{B}\right) = \varsigma W = \varsigma f \Delta u, \tag{3.29}$$

with W the FWHM of the far field intensity.

A few numerically computed examples of $|E|^2$ and $|E_{im}|^2$, with maxima assumed at $t = 0$, are given in Figure 3.4, using $\varsigma = 3$ and $V = 2, 4$ and 6. The side lobes in the imaged intensities are due to the truncation by the prism and mirrors.

The relative power of the light at a certain wavelength captured by a receiver waveguide at a transverse distance t from the center of the image is given by [14]:

$$O(t) = \frac{\left|\int_{-\infty}^{\infty} E_m(t') E_{im}(t' - t)\, dt'\right|^2}{\left|\int_{-\infty}^{\infty} E_m^2(t')\, dt'\right|^2}. \tag{3.30}$$

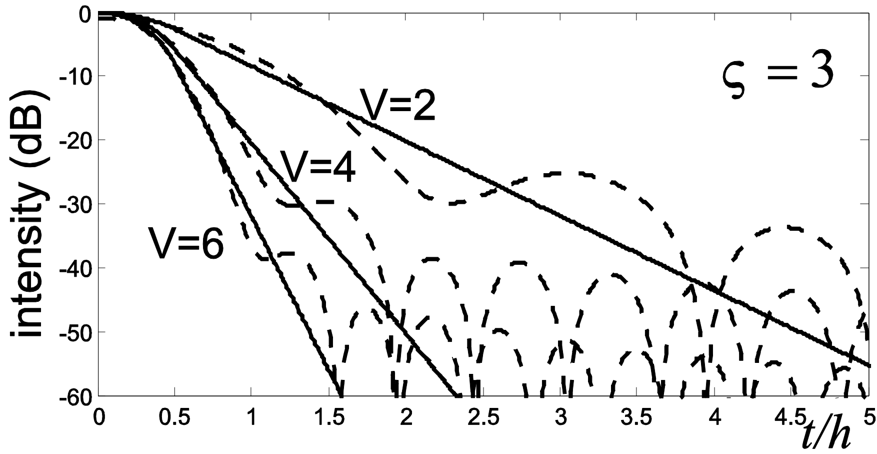

Figure 3.4: Intensity profiles for modal fields (solid lines) and the corresponding images (dashed lines) for indicated parameters, calculated using Equation (3.28).

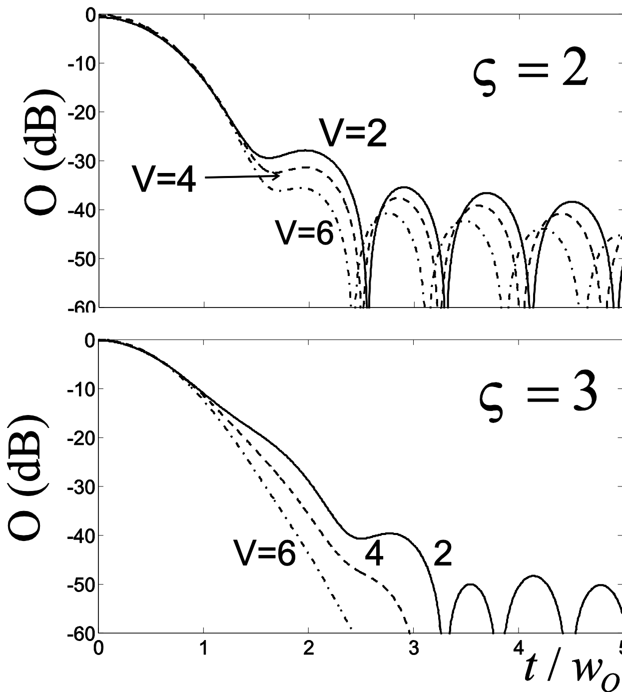

Figure 3.5: Relative power captured by a receiver waveguide at a distance of t/w_O from the maximum of the image.

Results are given in Figure 3.5 for $\varsigma = 2$ and 3 and $V = 2,$ 4 and 6, showing the quantity O as a function of t/w_O, with w_O the FWHM of O. Figure 3.6(a) shows the computed curves of $w_O\,V/h$ versus V. It is seen that for given index contrast (defined by *V/h*; see Equation (3.27)) w_O increases approximately linearly with V. For comparison, the corresponding modal width (corresponding to the FWHM of $|E_m|^2$), in terms of $w_m\,V/h$, is also shown. As expected w_O is larger than w_m, approximately by a factor of $\sqrt{2}$, as would have been the case if E_m would be purely Gaussian and there would be no truncation.

The functional loss $(O(t = 0))$, as depicted in Figure 3.6(b), is relatively low for the considered parameter range.

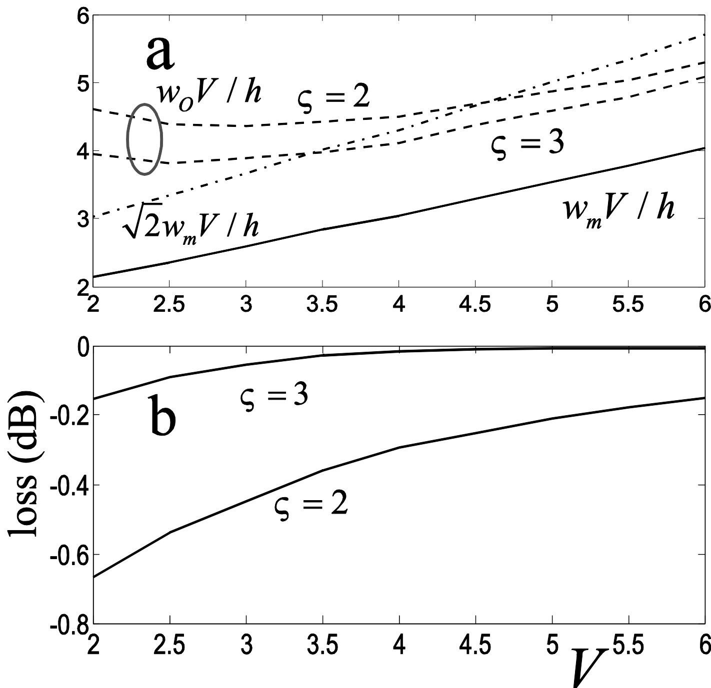

Figure 3.6: Modal width, FWHM of O (a) and the functional loss $O(t = 0)$ as a function of V.

Curves like the ones depicted in Figure 3.5 can be used to determine a number of device parameters as follows. The maximum of the image of $|E_{im}^2(t)|$ corresponds to $t = 0$ for, say, λ_0. Then, the maximum of the image corresponding to $\lambda_0 + \Delta\lambda/2$ (with $\Delta\lambda$ the 3dB bandwidth) should correspond to $t = t_{3dB} = w_O/2$. Knowing the required ratio $\Delta\lambda_{cs}/\Delta\lambda$, the position t_{cs} of the adjacent channel can be obtained from

$$t_{cs} = \Delta\lambda_{cs} w_O/\Delta\lambda \tag{3.31}$$

where the value of w_O can be determined as explained below.

Next, the desired ACCT as well as the global functional CT (owing to the side lobes) can be obtained by selecting the appropriate parameters ς and V from curves as in Figure 3.5, assuming for the moment that there are no constraints on the acceptance angle γ (a large acceptance angle may cause blurring of the focal image as noted in Section 3.2.2). For example, if $\Delta\lambda_{cs}/\Delta\lambda = 2$ (corresponding to $t_{cs}/w_O = 2$ according to equation 31) and if it is required ACCT$< -30dB$ one may choose V slightly larger than 2 ($V = 2.2$) with $\varsigma = 3$, if the corresponding global CT ($-50dB$) is acceptable. A choice of $V = 3$ with $\varsigma = 2$ is also an option. If the required ACCT and CT are not attained one may choose for a smaller 3 dB bandwidth than required. One may choose among the above options by considering also the device area as discussed in Section 3.3.

Knowing ς and V one can find h (for given contrast and wavelength, using Equation (3.27)), E_m, E_{im}, w_O and the channel spacing, t_{cs}, using Equation (3.31). The required focal distance f follows from $w_O = f\sigma_2'\Delta\lambda$ (which follows from the fact that $t_{3dB} = w_O/2$ should correspond to $\lambda_0 + \Delta\lambda/2$), and is is given by

$$f = w_O/(\sigma_2'\Delta\lambda). \tag{3.32}$$

Knowing also f the fields at the virtual aperture can be calculated, the FWHM of the corresponding intensity, W, and so $\tilde{B}$, via $\tilde{B} = \varsigma W$.

3.2.4 Effect of Phase Shift upon Reflection

As is well known on TIR of a planar mode by a mirror a phase shift upon reflection (PSR) will occur which depends on structural properties, wavelength and angle of incidence. For the considered parabolic mirror this means that the PSR is position dependent and these variations along the mirror lead to both (extra) beam deflection and (de)focusing effects for which we will present useful expressions next. Thereafter, we will present a formula for the well-known Goos-Hänchen shift (GHS) [14].

First deflection, due to PSR, with phase shift $\varphi(s)$, with s a local coordinate directed along the mirror, and modal reflection coefficient $r = |r|e^{i\varphi}$, for a flat non-uniform (via $\varphi = \varphi(s)$) mirror (see Figure 3.7) will be considered. The figure shows two incoming rays, both at an angle of incidence θ, which are refracted by the mirror at a slightly different angle θ'. The phase shifts corresponding to trajectories 1 and 2 in between the dashed lines indicating the wave fronts should be equal, so

$$\Delta s k N_1 \sin\theta - \varphi_1 = \Delta s k N_1 \sin\theta' - \varphi_2. \tag{3.33}$$

From Equation (3.33) one may derive

$$\Psi(\theta) \equiv \theta' - \theta = \frac{\partial \varphi}{\partial s} \frac{1}{k N_1 \cos\theta} = \frac{\partial \varphi(\theta)}{\partial y} \frac{1}{k N_1}, \tag{3.34}$$

with Ψ the PSR induced deflection angle, which varies along the parabolic mirror. It can be expanded according to

$$\Psi = \Psi_m + \chi(\theta - \theta_m) + \cdots, \tag{3.35}$$

where Ψ_m and $\chi \equiv \partial\Psi/\partial\theta$ are both evaluated (numerically) at $\theta_m \equiv (\theta_l + \theta_h)/2$. The first term at the right hand side of Equation (3.35) corresponds to a uniform deflection leading to both a small angular shift of the focal point and a change in focal distance (as follows from geometrical optics). The second term leads to a change of the focal distance. The GHS leads to an apparent shift of the reflected ray along the reflecting interface, given by [14]:

$$GHS = \frac{\partial\varphi}{\partial\theta}\frac{1}{kN_1\cos\theta}. \tag{3.36}$$

In calculations based on ray tracing one should take into account the effect of the PSR and use both the expressions for GHS (Equation (3.36)) and for the tilt (Equation (3.34)) to simulate a ray reflected by a curved mirror.

As an alternative to the above approach (in which the PSR induced shift of the focal point is calculated) one could shape the parabolic mirror via numerical calculations such that the PSR induced deflection is fully compensated (for λ_c).

In order to obtain the magnitude of the PSR one could most conveniently use existing software for channel mode solving, as illustrated by the example in Section 3.3.2.

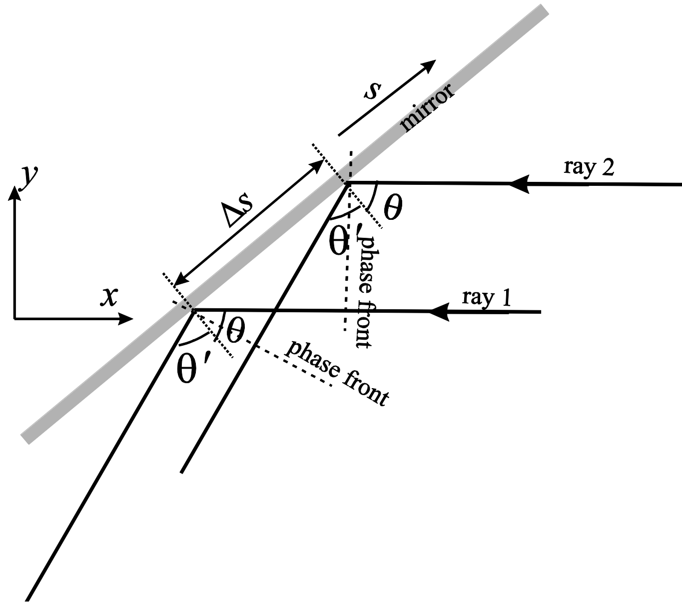

Figure 3.7: Illustration to the derivation of the effects of PSR.

3.3 Design

In this section we will first sketch a general optimization strategy for considered device on the basis of the theoretical considerations given above. Thereafter, the scheme will be applied for the design of an actual device as an illustration. As mentioned above, only the case of minimum deviation (for the central wavelength, λ_c), corresponding to a symmetric set up, will be considered.

It is assumed that the wavelength channel spacing $\Delta\lambda_{cs}$ and the 3 dB band width ($\Delta\lambda$) are fixed, as well as the maximum allowable ACCT and CT, and that it is our task to design the device such that the device area G (apart from the waveguides) is minimized. As a reasonable measure for G we will take the following approximate expression (see also Figure 3.8; G corresponds to the grey rectangle):

$$G \approx f^2 \sin(2\vartheta) + bf \cos\vartheta, \quad 2\vartheta \equiv 4\theta_l - \pi - \delta. \tag{3.37}$$

Here δ $(= \eta - 2\sigma)$ is the deviation angle and we assumed in Figure 3.8 that $\vartheta > 0$ (typically $\vartheta \approx 20^{\circ}$). It is seen from the equation that f, occurring in both terms, has a slightly larger impact on the device area than base length b. With $\vartheta \approx 20^{\circ}$ and assuming that b is smaller or not very much larger than f it can be shown from Equation (3.37) that the area becomes smaller if δ increases, i.e., $\partial G/\partial\delta < 0$.

As is also seen from Equation (3.37), the orientation of the prism has a considerable impact on the device area, as with the opposite orientation $-\delta$ would have to be replaced by $+\delta$, which would lead to a much larger value for ϑ and so for *G*. In most practical cases (like in the example discussed in Section 3.3.2) the orientation has to be chosen as indicated in Figure 3.8 to attain a lower device area.

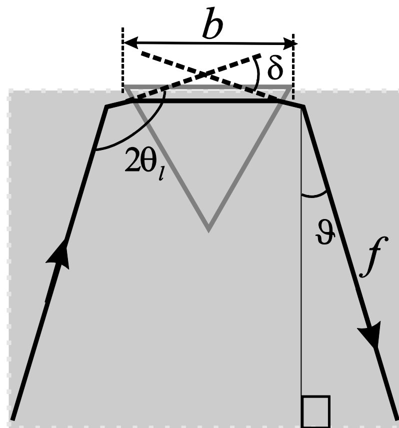

Figure 3.8: Illustration to Equation (37) giving the approximate device area (indicated by the grey rectangle).

3.3.1 Scheme

The optimization scheme proceeds along the following steps, for which it is assumed that the materials for guiding, cladding and cover layers have been chosen already. The required values for λ_c, $\Delta\lambda_{cs}$, $\Delta\lambda$, the ACCT and the CT

are assumed to be given. It is also assumed that the effective index contrast for the ridge waveguide has been chosen.

1. Choose the two thicknesses (h_1 and h_2) for the thick and thin slabs (corresponding to N_1 and N_2, respectively) such that the quantity R (defined in Section 3.2) is maximized, taking into account, if required, constraints defined by the technology. According to Equation (3.15) a larger R leads to a larger resolving power for given lay-out (and so to a lower required device area for given required resolving power). The above choice determines the quantities N_1, N_2, D' and D as well as the critical angle θ_{crit} (see Section 3.2).

2. Determine the angles σ, η and θ_l. Inspecting Equation (3.9), it follows that σ should be as large as possible for a larger value of σ_2' and so a smaller value of $\tilde{B}$ (and so a smaller device area), according to Equation (3.15), for fixed $\Delta\lambda_f$. On the other hand the angle σ should be below the critical angle, θ_{crit} for small reflection loss at the prism boundaries. The choice of σ may be checked with (approximate) calculations of this loss as in the example below. Knowing σ the angle η of the prism is defined according to Equation (3.2) and the property $\eta = \alpha_1 + \alpha_2$. The angle θ_l should be chosen above θ_{crit} for 100% modal reflection but not too far above θ_{crit} to avoid the aberrations mentioned in Section 3.2.2.

3. Determine the parameters V and ς such that the required device performance is obtained with minimum device area, using graphs like the ones in Figures 3.5 and 3.6. On doing so, one may use that $b \propto \varsigma$ and that $f \propto w_0 \propto V$ (if $V \geq 4$) as is seen from Equation (3.32) and Figure 3.6(a). Note also that generally a smaller ς leads to larger functional losses according to Figure 3.6(b). Next, from V and ς one may determine $\tilde{B}$ and f via the procedure outlined in Section 3.2.3. The quantities $\tilde{B}$, η and σ determine the prism size and shape. Using $\tilde{B} = f\gamma$ fixes the angle γ and so, with θ_l and $\tilde{B}$ the parabolic mirrors. The orientation of the mirrors with respect to the prism follows from the angle σ.

4. The positioning of the input and receiver waveguides can now be calculated with the mirror parameters and geometrical optics, including the PSR effect, as discussed in Section 3.2.4.

5. It has to be checked if the thus obtained device structure leads to (too large) aberrations (as an effect of the parabolic mirrors) for the outermost wavelengths of considered region. If so a larger V value has to be chosen implying a lower acceptance angle for the mirrors and lower aberrations; the adaptation will generally lead to (harmless) over-performance with respect to ACCT and CT.

It is noted from the discussions in Section 3.2.3 and above that, for given $\Delta\lambda_{cs}/\Delta\lambda$ and ACCT, both f and b are inversely proportional to the 3 dB bandwidth $\Delta\lambda$ and so that G, is roughly inversely proportional to $\Delta\lambda^2$.

3.3.2 A Numerical Example

The spectrometer that will be discussed in this section is planned to be used for determining the natural moisturizing factor (NMF) in human skin [7]. This application requires a value for $\Delta\lambda_{cs}$ of 5 nm at $\lambda_c = 850\ nm$ with an operating bandwidth of $100\ nm$. The device will be operated with TE polarization. We assume a 3 dB bandwidth of $\Delta\lambda = 2.5\ nm$, implying that $\Delta\lambda_{cs}/\Delta\lambda = 2$, and values for the cross talk as follows: ACCT $< -40\ dB$ and CT $< -50\ dB$. The guiding layer will be a Si_3N_4 layer (index 2.008), which is sandwiched between two SiO_2 layers (index 1.452). The height of the input/output waveguides is chosen equal to that of the thicker slab waveguide in order to decrease the losses at the exit of the input waveguide and entrance of the receiver waveguides. The ridge height is chosen such that the lateral index contrast of the waveguide is 0.01, which is sufficiently small to arrive at single mode waveguides with the available fabrication processes (minimum feature size 1 μm).

The desired spectrometer is designed by following the optimization scheme explained in the previous section.

1. The quantities N_1 and D' depend on the thicknesses used for the two waveguiding slab regions. We have optimized R by varying the two slab thicknesses between 40 nm, which is a safe lower limit to prevent leakage to the Si substrate, and 170 nm, which is a safe upper limit for the thickness of the Si_3N_4 layer made with our fabrication facility (there may be cracks in the layer if the thickness exceeds 170 nm). As can be seen from Figure 3.9, R is maximized to a value of $2.34\,x\,10^{-4}\,/nm$ by choosing a thickness of 170 nm, which corresponds to $N_1 = 1.6931$ at λ_c, for the thicker layer (field outside the prism) and a thickness of 40 nm, which corresponds to $N_2 = 1.4785$ at λ_c, for the thinner layer (prism). Note that, as is seen from Figure 3.9, the optimum thickness for the thicker layer would have been 190 nm if there would be no upper limit for the thickness of the Si_3N_4. The height of the Si_3N_4 waveguides is chosen to be 170 nm, which corresponds to $N_g\,(= N_1) = 1.6931$ and the ridge height is chosen as 7 nm, which corresponds to $N_a = 1.6831$. The critical angle corresponding to the two slab regions is given by $\theta_{crit} = 60.84^{\circ}$.

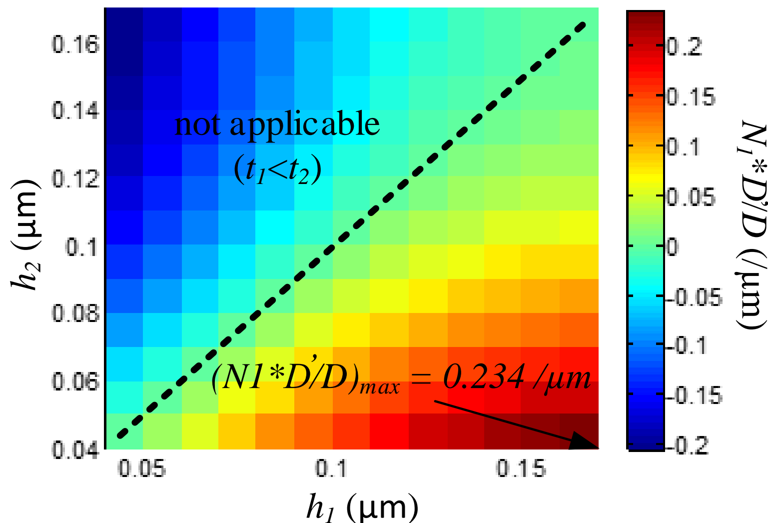

Figure 3.9: Value of the quantity R as a function of layer thicknesses h_1 and h_2.

2. Figure 3.10 shows the modal transmittance at the adiabatic interface, of which the structural parameters are given in the inset, as an angle of incidence (from the high thickness side), as calculated by transforming the 3-D scattering problem (scalar approximation) to an effective 2-D Helmholtz problem [2], where the incidence angle appears as a parameter as it will be explained in Chapter 6. This effective equation is then solved by a quasi-analytic 2-D method, applying a fine staircase approximation of the taper profile [15]. Owing to the adiabaticity the curve changes abruptly from nearly unity to zero at an angle equal to θ_{crit}. The angle σ is chosen somewhat below θ_{crit}, at $\sigma = \theta_{crit} - 5°$. This choice leads to $\eta = 142.7°$, $\sigma_2' = 0.4072\ \mathrm{rad/\mu m}$ (see Sec. 3.2.1). The smallest angle of incidence on the mirror is chosen as $\theta_l = \theta_{crit} + 1°$.

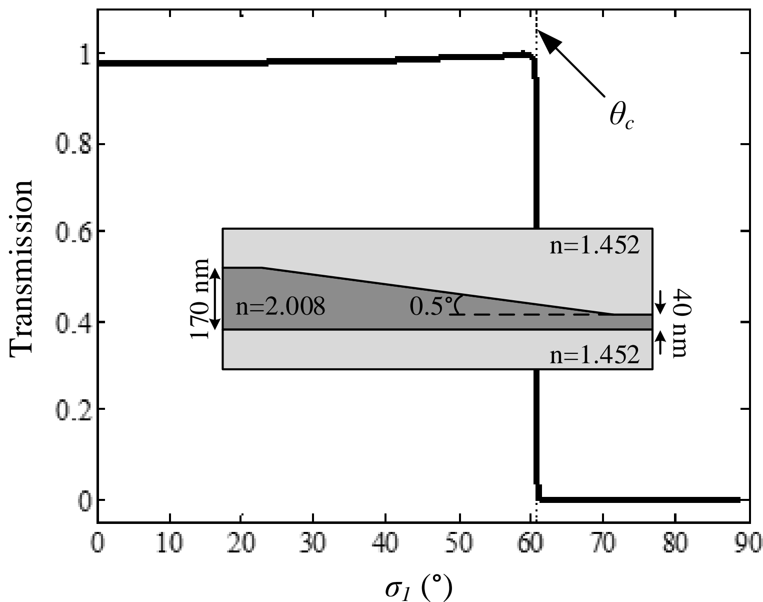

Figure 3.10: Transmittance vs. angle of incidence on the adiabatic taper. The inset depicts the taper structure.

3. Considering Figure 3.5 with the above performance conditions in mind it is seen that the combination $V = 6$ and $\varsigma = 3$ fulfills all the requirements: the ACCT (=$O(t/w_O = 2)$) is well below $-40\ dB$ and the global CT is sufficiently low. A combination of $V \geq 6$ and $\varsigma = 2$ would also be suitable and lead to a comparable device area, but the losses will be a bit higher, ~4% according to Figure 3.6(b). From the formulae presented earlier, it now follows: $w_O = 3.74\ \mu m$ (from Figure 3.6(b)), $f = 3.674\ mm$ (from Equation (3.32)), $W = 307\ \mu m$ and $B = 921\ \mu m$ (from Equation (3.29)) and $\gamma = 14.34°$. Note that, as a consistency check, f also has been calculated using both the formula $\tilde{B} = f\gamma$ and the geometrical parameters of the mirror; it was found that all three approaches led to virtually the same result.

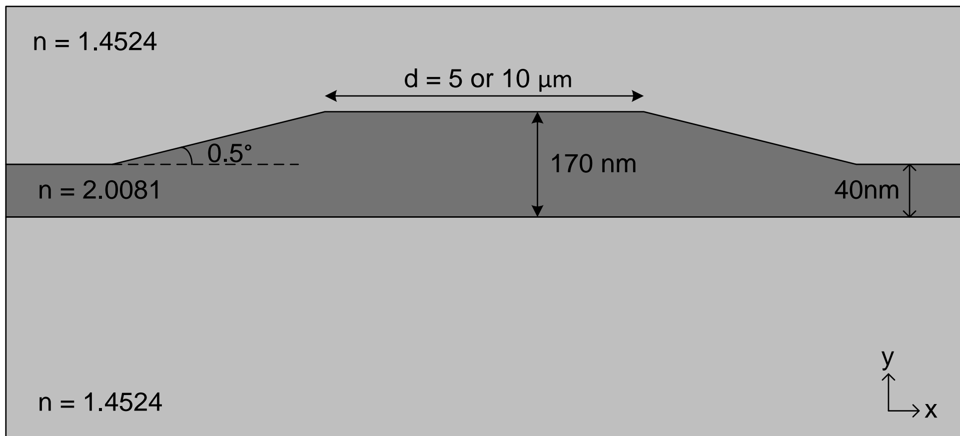

Figure 3.11: Structure of the imaginary channel waveguide used to calculate phase change upon total internal reflection of slab TE modes.

4. We propose a new method to calculate the phase shift upon TIR at slab waveguide interfaces. In this method an imaginary waveguide structure

with symmetric tapered edges, which are identical to the tapered profiles to be used in the mirror and prism interfaces, is considered. Figure 3.11 shows the structure of this imaginary waveguide, which is a ridge waveguide with $40\ nm$ equal to prism slab thickness) and $170\ nm$ (equal to field slab thickness) slab waveguide thicknesses and the taper between these thicknesses has an angle of 0.5°, as defined by the fabrication process. Analysis of the field of the channel mode in the center of the imaginary waveguide shows that it is composed of virtually only the TE slab mode for not too narrow channel waveguides, i.e., the overlap between this field and the $170\ nm$ thick slab mode is close to unity. Therefore, the structure can be pictured as a simple waveguide in which the TE slab mode is bouncing between the tapered edges (see Figure 3.12).

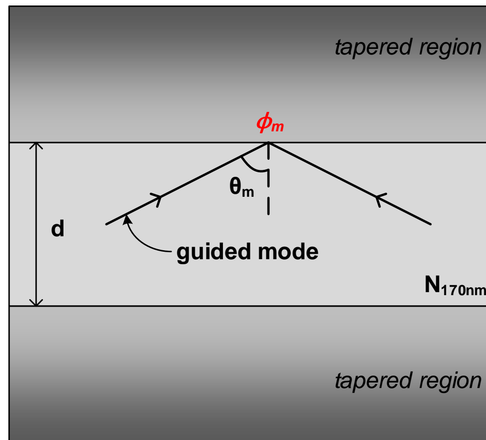

Figure 3.12: Simplified 1D view of the imaginary waveguide structure.

In order to find the phase change (ϕ) resulting from total internal reflection with an angle of incidence of θ the transverse resonance condition can be used

$$2dN_{170nm}\frac{2\pi}{\lambda}\cos\theta_m - 2\phi_m = m2\pi, \tag{38}$$

where m denotes the mode number, d is the width of the non-tapered waveguide part, N_{170nm} is the effective index of the $170\ nm$ slab. The phase shift upon TIR, θ_m, for a specific channel mode can be calculated by using the following formula;

$$N_m = N_{170nm} \sin \theta_m, \tag{39}$$

where N_m is the effective index of the mth channel waveguide mode, calculated using appropriate software. For each channel mode one thus obtains a sample value ϕ_m for the phase shift upon TIR of the incidence angle θ_m. Figure 3.13 shows the calculated phase shift upon TIR at the considered tapered interface for two different non-tapered waveguide widths (d) at $\lambda = 850\ nm$ for a number of angles of incidence and the polynomial fit of the data for $d = 5\ \mu m$. The incidence angle range $(\Delta\theta)$ used in the designed mirror is also depicted in the figure. It can be seen from the figure that the results for different d values are in good agreement. θ_m values of the data points on this figure correspond to discrete channel waveguide modes. In order to calculate a smooth curve $\phi(\theta)$ these data points can be fitted to a polynomial function. Knowing the relation $\phi(\theta)$ the full lay-out of the spectrometer can be designed using ray tracing together with Equation (34) and Equation (36), to account for the PSR effect.

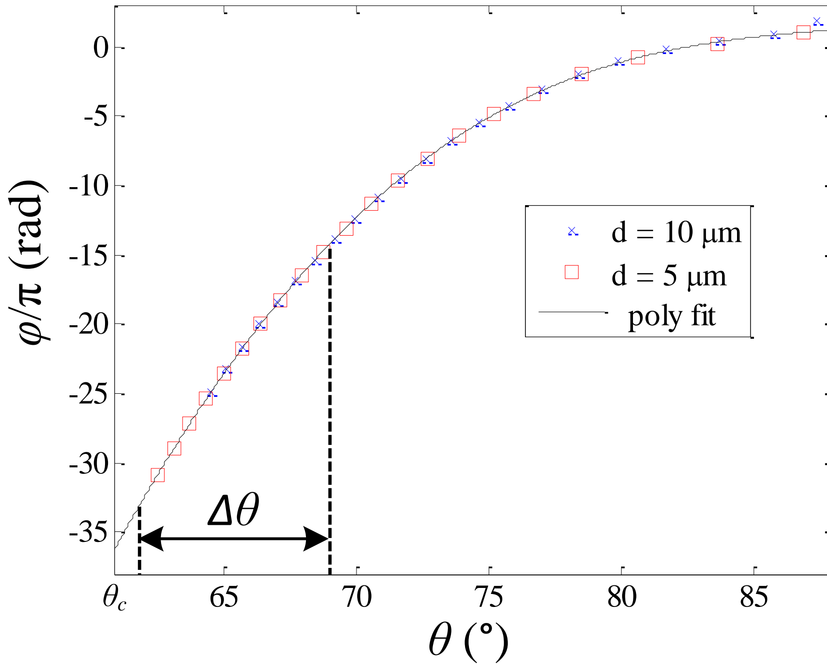

Figure 3.13: Phase shift upon TIR vs. incidence angle for the considered interface with 0.5° taper angle at λ = 850 nm. $\Delta\theta$ is the used incidence angle range for the designed mirror.

As an example of the effect of the applied correction for waveguide positions we present some results calculated using ray tracing based numerical calculations: the input waveguide is shifted $74.9\ \mu m$ along the x-axis, $29.7\ \mu m$ in y-axis and turned by $0.64°$ ($0.011\ rad$) CCW. For the receiver waveguides the effect corresponds to a considerable wavelength shift being $(0.011/\sigma_2' =)\ 27.38\ \ nm$.

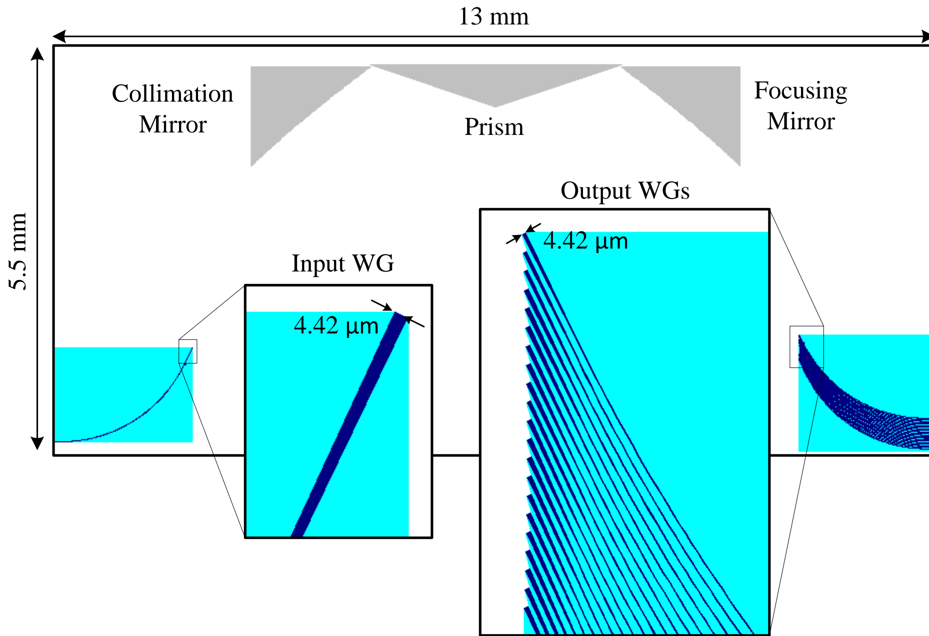

Figure 3.14: Full layout of the designed prism spectrometer, which has a size of $5.5\ x\ 13\ mm^2$; the inset shows the input and receiver waveguides in more detail.

5. With geometrical optics we have, for the structure resulting from the above steps, calculated the broadening of the image field for the outermost wavelengths of the considered region ($\lambda = 800$ and $900\ nm$). Considering only the rays in-between the two rays corresponding to the FWHM of the field coming from the focusing mirror (representing the major part of the power of the beam) a focal spot broadening of $0.6\mu m$ was found. This is equal to around 20.1% of the un-blurred image implying an approximate broadening as small as 2% $(\sqrt{1+0.2^2}-1=0.02)$ and a minor extra functional loss of around 1%. Here we assumed for simplicity Gaussian shapes for the beam cross section and the broadening. So, the aberration effect is minor and requires no structural adaptations.

The resulting layout of the spectrometer is presented in Figure 3.14. The size of the device is $5.5\ x\ 13\ mm^2$ including the input and output waveguides.

3.4 Conclusions

This chapter presented a general approach for the design of a planar prism-based spectrometer, utilizing dispersion effects in two slab waveguiding areas having different thicknesses of the guiding layer. Here, the different regions are assumed to be adiabatically connected via vertical tapering. Part of the design strategy is generally applicable and can be used for also for the design of for example arrayed waveguide gratings. A new method to cope with the effect of modal phase shifts upon modal reflection by (parabolic) mirrors defined by the interface between area of different slab thicknesses has been presented.

The design strategy was illustrated by a numerical example assuming SiON technology. Assuming a central wavelength of 850 nm, a channel spacing of $5\ nm$, an adjacent channel cross talk of $-40\ dB$ and a cross talk of $-50\ dB$ lead to a required device area of $5.5\ x\ 13\ mm^2$ and a minor functional loss of a few percent over a wavelength range of $100nm$.

3.5 References

[1] P. Tien, "Integrated optics and new wave phenomena in optical waveguides," *Reviews of Modern Physics,* vol. 49, pp. 361-420, 1977.

[2] R. Martin and R. Ulrich, "Geometrical optics in thin film light guides," *Applied Optics,* vol. 10, pp. 2077-2085, 1971.

[3] C. Tseng, W. Tsang and S. Wang, "A thin-film prism as a beam seperator for multimode guided waves in integrated optics," *Optics Communications,* vol. 13, pp. 342-346, 1975.

[4] M. Gibbon, G. Thompson, S. Clements, D. Moule, C. Rogers and C. Cureton, "Optical performance of integrated 1.5 um grating wavelength-

demultiplexer on InP-based waveguide," *Electronics Lett.,* vol. 25, pp. 1441-1442, 1989.

[5] C. Chen and R. Jang, "Polymer-based 1x6 thermooptic switch incorporating an elliptic TIR waveguide mirror," *Journal of Ligthtwave Technology,* vol. 21, pp. 1053-1058, 2003.

[6] M.K. Smit and C. van Dam, "Phasar-Based WDM-Devices: Principles, Design and Applications," *IEEE J. Selected Topics in Quant. Electron.,* vol. 2, pp. 236-250, 1996

[7] N. Ismail, F. Sun, G. Sengo, K.Wörhoff, A. Driessen, R. de Ridder and M.Pollnau, "Improved arrayed waveguide grating layout avoiding systematic phase errors," *Optics Express,* vol. 19, pp. 8781-8794, 2011.

[8] B.I. Akça, V. Duc Nguyen, J. Kalkman, N. Ismail, G. Sengo, Fei Sun, A. Driessen, T.G. van Leeuwen, M. Pollnau, K. Wörhoff, and R.M. de Ridder, "Toward spectral-domain optical coherence tomography on a chip," *IEEE Journal of Selected Topics in Quantum Electronics*, vol. 18, pp. 1223-1233, 2012.

[9] S. Janz, A. Balakrishnan, S. Charbonneau, P. Cheben, M. Cloutier, A. Delâge, K. Dossou, L. Erickson, M. Gao, P.A. Krug, B. Lamontagne, M. Packirisamy, M. Person, and D.-X. Xu, "Planar Waveguide Echelle Gratings in Silica-On Silicon," *IEEE Photon. Electron. Lett.*, vol 16, pp. 503-505, 2004.

[10] P.J. Bock, P. Cheben, J.H. Schmid, A.V. Velasco, A. Delâge, S. Janz, D.-X. Xu, J. Lapointe, T.J. Hall, and M.L. Calvo, "Demonstration of a curved sidewall grating demultiplexer on silicon," *Opt. Express*, vol. 20, pp. 19882-19892, 2012.

[11] Y. Zhang, W. Huang, X. Wang, H. Xu, Z. Cai, "A novel super-high extinction ratio comb-filter based on cascaded Mach-Zehnder Gires-

Tournois interferometers with dispersion compensation," *Opt. Express*, vol. 17, pp. 13685-13699, 2009.

[12] F. Xia, M. Rooks, L. Sekaric, and Y. Vlasov, "Ultra-compact high order ring resonator filters using submicron silicon photonic wires for on-chip optical interconnects," *Opt. Express*, vol. 19, pp. 11934–11941, 2007.

[13] E. Hecht, "Optics (4th edition)," New York: Addison-Wesley, 2002.

[14] H. Kogelnik, "Theory of optical waveguides," in Guided-wave optoelectronics, ed: Springer, 1988, pp. 7-88.

[15] M. Hammer, "Quadridirectional eigenmode expansion scheme for 2D modeling of wave propagation in integrated optics," *Optical Communications,* vol. 235, pp. 285 – 303, 2004.

4 Integrated Optics Prism Spectrometer: Fabrication and Testing

In the previous chapter, the design of a fully integrated prism spectrometer in adiabatically connected slab WGs was described and a numerical example has been given to the presented design strategy. In this chapter, the design, fabrication and characterization of an on-chip prism spectrometer to be used for determining the natural moisturizing factor concentration of the human skin is described. As mentioned in the previous chapter, for this application the spectrometer should be operated with TE polarized light in a range of 100 nm around the central wavelength of λ_c = 850 nm with a channel spacing of $\Delta\lambda_{cs}$ = 5 nm. Although the spectrometer presented in the numerical example section of the previous chapter was designed for the same application, the spectrometer presented in this chapter does not have the same (optimized) layout because of time limitations as discussed later.

4.1 Introduction

An introduction into the field of micro spectrometers has been given in the previous chapter, where also a detailed design strategy was presented. This strategy has not been followed for the present device owing to the relatively long fabrication period for such devices, so that the fabrication of the device had to be started prior to finishing the full design strategy. The main aim of the here presented research was to experimentally test the various parts of the prism spectrometer. Also for this reason the device parameters were chosen to lead to a functioning yet not necessarily fully optimized device.

The rest of this chapter is organized as follows. First, after a short introduction we will present the design and fabrication of the prism spectrometer in Sections 4.2 and 4.3. It is followed by an explanation of the

experiments for characterizing the fabricated device in Section 4.4. The chapter ends with conclusions (Section 4.5).

4.2 Design

A schematic picture of the fabricated spectrometer is shown in Figure 4.1. The working principle of the device is identical to the one explained in the previous chapter. The device is composed of a tapered input WG, a collimation mirror, a prism slab, a focusing mirror and tapered receiver WGs corresponding to different wavelengths. The regions of different guiding slab thicknesses defining the prism and the mirrors are made by one technological step (for simplicity of fabrication) and are connected via adiabatic vertical tapers to minimize reflection losses at the prism interfaces. As can be seen from the figure, the prism is not chosen to be operated at minimum deviation (MD) condition. In this asymmetric layout the collimated light beam enters the right angled triangularly shaped prism with an incidence angle of 0°, which guarantees that the reflection loss is minimized at the prism entrance. Owing to the above perpendicular incidence, no dispersion takes place inside the prism. The light is dispersed only at the output interface of the prism. The inset of Figure 4.1 shows a detailed schematic (the ray trajectories and used symbols are also indicated) of the prism region. Using the geometry of this right angled prism it can be shown that the angular dispersion ($\sigma' \equiv \partial\sigma/\partial\lambda$, where λ is the wavelength) can be written as

$$\sigma' = D' \frac{\sin\eta}{\cos\sigma} \quad , \tag{4.1}$$

where we defined $D = N_2/N_1$, with N_1 and N_2 the effective indices of the thick and thin slabs, respectively and $D' = \partial D/\partial\lambda$.

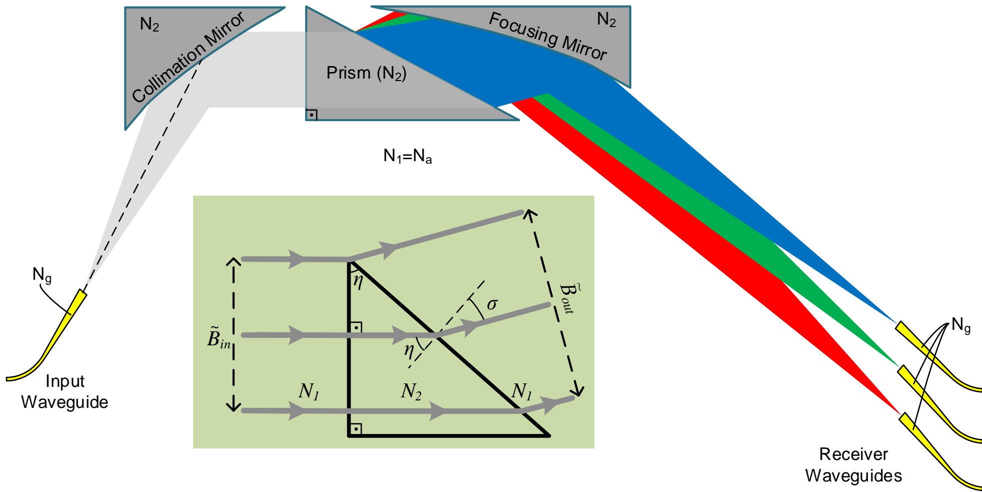

Figure 4.1: Schematic of the fabricated spectrometer. The white and dark grey areas correspond to thick and thin slabs, respectively. Ridge waveguides are indicated by the color yellow. The symbols *N* refer to the effective index of the planar structures corresponding to the regions indicated by the position of these symbols.

An expression for the spectral resolution can now be derived by inserting Equation (3.1) into Equation (3.14) of Chapter 3 and assuming that there are only minor truncation effects by choosing truncation parameter $\varsigma = 4$, which leads to

$$\Delta\lambda_f = \frac{16 \ln 2\, D \cos\sigma}{N_1 D' \sin\sigma\, \tilde{B}_{out} k_0} \quad , \tag{4.2}$$

where $\tilde{B}_{out} = \tilde{B}_{in}(\cos\sigma / \cos\eta)$ is the beam width at the output of the prism and $\tilde{B}_{in}$ is the beam width at the entrance of the prism. It can be seen from Equation (4.2) that the resolution can be optimized by choosing $N_1 D'/D$, which is defined by the Si_3N_4 thicknesses of the waveguiding slab regions, as large as possible and geometry related part of Equation (4.2) ($F_p \equiv \cos\sigma \,/\, \sin\sigma$) as small as possible. Once $N_1 D'/D$ and F_p values are chosen,

$\tilde{B}_{out}$ can be calculated for the desired $\Delta\lambda_f$. As mentioned in the introduction the device parameters were chosen to lead to a functioning yet not fully optimized device. Therefore, the other parameters related to the waveguides and mirrors were chosen by using an unoptimized version of the scheme explained in the previous chapter. Below, the choices done for all these parameters will be given and differences between the schemes will be discussed.

For the fabricated spectrometer, a Si_3N_4 layer (index 2.008) sandwiched between thermal SiO_2 (index 1.452) and PECVD coated SiO_2 (index 1.458) layers is used as the guiding layer. As we mentioned in the previous chapter the parameters N_1, D and D' depend on the indexes of the guiding and cladding layers and thicknesses used for the two waveguiding slab regions. Therefore, as is seen from Equation (4.2), the quantity N_1D'/D should be optimized by varying the slab thicknesses h_1 and h_2. For the fabricated spectrometer, the choice of h_1 and h_2 was done in an early stage of the design by maximizing the quantity D' (which leads almost to the same result as optimizing the quantity N_1D'/D). The optimization is done by varying the thickness of the guiding layer in the range between 40 nm, which is a safe lower limit to prevent leakage to the Si substrate, and 170 nm, which is the upper limit for the thickness of Si_3N_4 layer for our fabrication facility (there can be cracks in the layer after annealing the cladding oxide if the thickness exceeds 170 nm). The result does not differ very much from that of the more correct approach of previous chapter. As can be seen from Figure 4.2, D' is maximized to a value of 1.21 x 10^{-4} /nm by choosing a thickness of 160 nm and 40 nm for field outside the prism and prism, respectively. These thicknesses correspond to N_1 = 1.6785 and N_2 = 1.4785. The critical angle for total internal reflection (TIR) corresponding to the two slab regions is given by θ_{crit} = 61.75°. The length of the vertical taper between these slab regions is assumed to be 13.75 μm, based on available data for the technology (see Section 4.3). The height of the Si_3N_4 WGs is chosen to be 175 nm, which corresponds to N_g = 1.7003 and the ridge height is chosen as 15 nm, which corresponds to an effective index of the regions next to the

ridge of N_a (= N_1) = 1.6785. Therefore, the height of the input/output WGs is not the same as that of the free propagation area corresponding to N_1 and this will result in scattering loss at the interface between the input/output WGs and the free propagation area. It is noted that the waveguide height is slightly above the maximum allowable height of 170 nm in the fabrication process. However, it does not cause cracking during the annealing of cladding oxide, since the total area occupied by the input and receiver waveguides is very small.

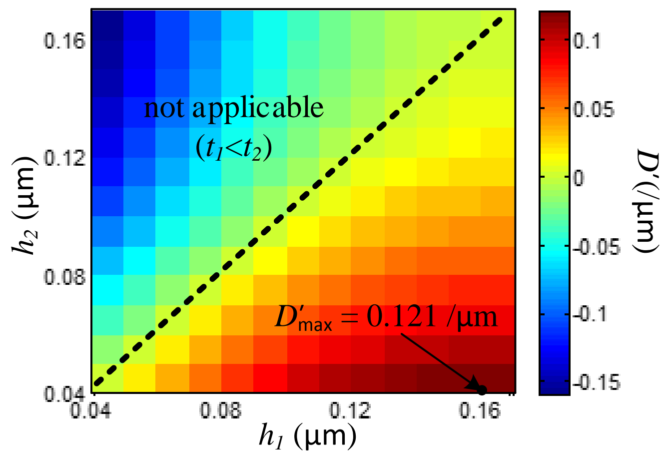

Figure 4.2: Prism dispersion (D') as a function of t_1 and t_2.

The optimization of F_p is done by using the chosen effective refractive indexes for expressing F_p as a function of η and varying η between 30° and 90° (see Figure 4.3). The boundary angles have been chosen for the following reasons. Below 30° F_p is too large which would result in a very large device; and 90° is the upper limit for η (the beam will not hit the output facet of the prism if η exceeds 90°). As is seen from Figure 4.3, η should be chosen as large as possible for optimizing the far field resolution. However, if it is too close to 90°, the reflection loss could be high at the output of the prism and $\tilde{B}_{out}/\tilde{B}_{in}$ (= $\cos\sigma/\cos\eta$) ratio will be too high, making $\tilde{B}_{in}$ impractically low such that it is close to the wavelength and not collimated

anymore (owing to diffraction). Moreover, increasing η further up from 75° increases the resolving power only by a factor of 1.2 at maximum (when η = 90°). Considering all these details, angle η is chosen as 75°. This choice leads to σ = 58.3° and σ' = 2.22x10^{-4} rad/nm. Here, the angular dispersion is considerably lower than the value (4.07x10^{-4} rad/nm) reported in the previous chapter. This drop is due the geometry chosen for the prism.

As mentioned before, our aim was to fabricate a functioning device, which does not have to be fully optimized. Therefore, for the choices of parameters, functionality was our main concern. The lowest angle of incidence/reflection to the mirrors (θ_l) is chosen well above θ_{crit} as $\theta_l = \theta_{crit}$ + 10° while it is chosen θ_{crit} + 1° in the optimized scheme explained in the previous section. By choosing θ_l high, the effect of phase shift upon reflection (PSR) is reduced for a given range of incidence/reflection angles ($\Delta\theta$) since the derivative of the phase shift upon TIR (φ) with respect to θ is lower for higher θ values as can be seen from Figure 3.13 of the Chapter 3. This lowers the PSR effect (tilt and Goos-Hänchen shift (GHS)) according to the formulae of Section 3.2.4 of Chapter 3. Besides, $\Delta\theta$ is chosen rather low as 2.5° for further reduction of the PSR effect. The parameters V and ς, where V has been defined in reference [1] (see also equation 27 of chapter 3) and ς is the truncation parameter defined as $\tilde{B}_{in} = \varsigma W_{in}$ (W_{in} is the full width at half maximum of the beam at the output of collimation mirror) are chosen by considering the geometrical broadening in the image field. The broadening of the image field (calculated by ray tracing) for the outermost wavelengths of the considered region ($\lambda = 800$ and $900\ nm$) is chosen to be below 20 % of the FWHM of un-blurred image as it will be discussed later in this chapter. A parameter set satisfying the above criterion is: V = 19.06 and ς = 1.56.

As explained in the Section 4.3.1 of the previous chapter a parabolic mirror is fully defined by the parameters θ_l, γ (which is the angle between the outermost rays and defined by the parameter set V and ς) and $\tilde{B}$ (the beam width). The mirrors are arranged such that the parameters θ_l and γ are exactly

the same for the two mirrors. The beam width at the output of the prism is determined by choosing $\Delta\lambda_f$ =1.6 nm (an approximation for $\Delta\lambda$) and using a modified version of Equation (4.2) with ς = 1.56 to choose the beam width, $\tilde{B}_{out}$. The above choices lead to; $\tilde{B}_{in}$ = 500.0 µm by using Equation (4.2), $\tilde{B}_{out}$ = 1015.1 µm by using prism geometry, a focal length of the input mirror f_{in} = 5.726 mm, a focal length of the output mirror f_{out} = 11.627 mm by using $\tilde{B} = f\gamma$, W_{in} = 320.5 µm and W_{out} = 650.7 µm by using Equation (3.12) of Chapter 3. As can be seen from the above values, the fabricated spectrometer differs from the optimized spectrometer explained in the previous chapter. The expected angular dispersion at the output of the prism and numerical aperture of the waveguides are lower (due to the higher V value) in the fabricated one. Therefore, the size of the fabricated device is larger than the optimized one as can be seen later in this section.

The mirrors are designed for the central wavelength and will introduce imaging errors at other wavelengths. To estimate the magnitude of the blurring effect we have considered the field image corresponding to the outermost wavelengths of considered wavelength region using ray tracing as follows: Considering only the rays in-between the two rays corresponding to the FWHM of the field coming from the focusing mirror (representing the major part of the power of the beam) a focal spot broadening of 0.81 µm was found. This is equal to around 15.4 % of the un-blurred image implying an approximate broadening as small as 1.2 % ($\sqrt{1 + 0.154^2} - 1 = 0.012$).

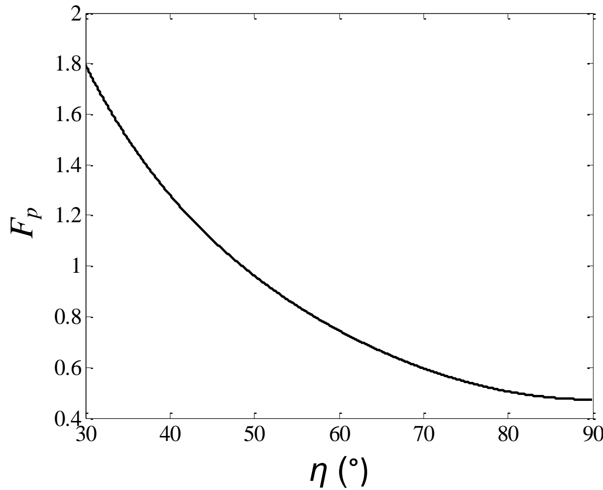

Figure 4.3: Graph of the quantity $F_p(\eta)$.

The resulting layout of the fabricated spectrometer chip, which has a size of 8 x 29.5 mm^2 including the input and output waveguides, is shown in Figure 4.4. There are 31 receiver waveguides corresponding to the wavelengths between 775 nm and 925 nm with a channel spacing of 5 nm. It should be noted that, the positions of these waveguides are not corrected for the PSR effect, which was underestimated during the design of the device since there were no theory available (only approximate models) at that time. The reference waveguides, which can be seen in Figure 4.4, are placed for measuring losses in the spectrometer but the loss measurements cannot be performed since the device does not work properly as discussed in the next section. The layout, with 90° bends in the input WGs, has been chosen such that only a small part of the stray light generated at the input interferes with the spectrometer.

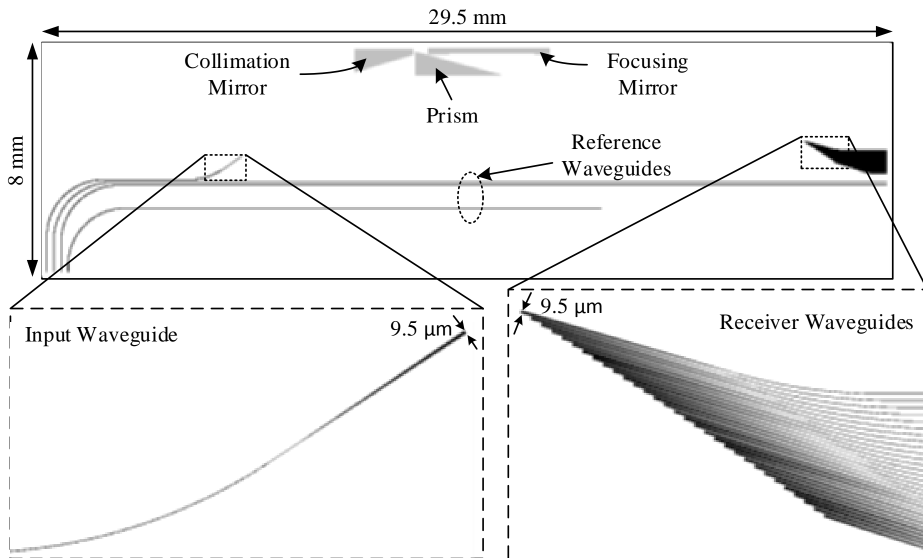

Figure 4.4: Full layout of the fabricated spectrometer, which has a size of 8 x 29.5 mm^2. The figures at the bottom show the input and receiver waveguides in detail.

4.3 Fabrication

The proposed device is implemented in Si_3N_4 (nitride) layer sandwiched between buffer and cladding SiO_2 (oxide) as mentioned before. The wafer cross-sections corresponding to different steps in fabrication process flow, which will be discussed next, are shown schematically in Figure 4.5.

The following steps can be discerned:

(a) The fabrication process starts with deposition of 178.7 nm stoichiometric nitride (by using LPCVD) on top of an 8 µm thermal oxide coated Si wafer. The deposition is followed by an annealing step, which is essential for avoiding the cracks at the annealing step of the top cladding layer, at 1100 °C for 3 hours. The thickness of the nitride layer is decreased to 175.0 nm after the post-deposition annealing by using BHF etching.

(b) This is followed by patterning of ridge waveguides using 15 nm deep nitride etching in BHF solution. In this step the thickness of the field outside the ridge waveguides decreased to 160 nm.

(c) Next, a sacrificial oxide layer, which is used in the adiabatic etching process of the nitride layer for under-etching, is deposited in oxygen plasma (10 min at 300 W RF power and 1.25 mbar chamber pressure). Subsequently, the prism and mirror trenches are patterned by 120 nm deep nitride in BHF. This etching process is done in several steps (each step takes approximately 1 hour); the masking photoresist is annealed at 120 ˚C after each step in order to prevent peeling off the photoresist. Thereafter, the sacrificial oxide is removed.

(d) Finally, cladding oxide is deposited by using PECVD (substrate temperature of 300 ˚C, RF power of 300 W, chamber pressure of 650 mT and gas mixture of 710 sccm N_2O and 200 sccm 2% SiH_4/N_2) and annealed at 1100 °C for 3 hours. This annealing step is essential for decreasing the refractive index of the PECVD oxide layer in order to prevent that the cladding layer supports a guided mode, with virtually no field in the buffer layer, which would for this reason not be damped by the Si substrate [2].

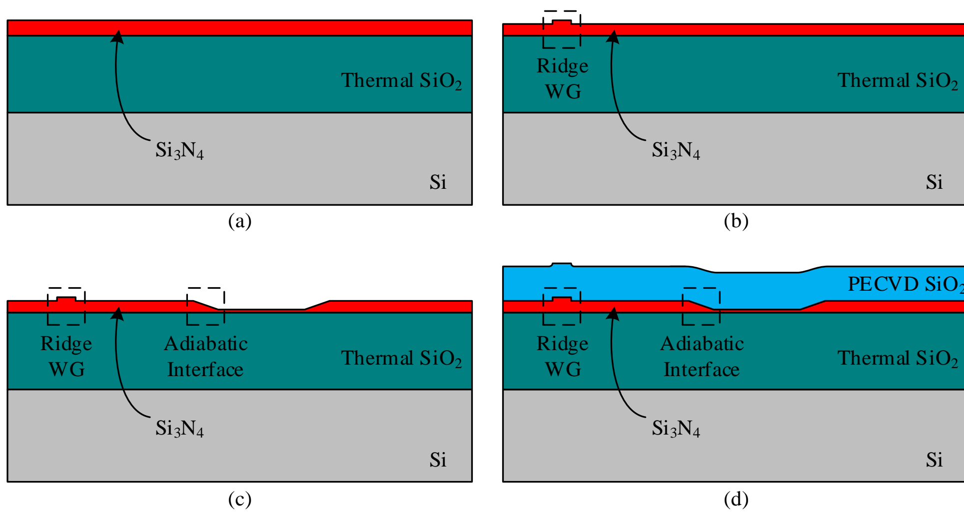

Figure 4.5: Wafer cross-sections corresponding to different steps in the fabrication process flow.

A top view photograph (taken with a microscope) of the fabricated device can be seen in Figure 4.6, which shows the prism (almost completely) in the middle and the mirrors (partly) on the left and right hand sides. The length of the adiabatic transition section, which is expected to be 13.75 μm by considering the etching process of as deposited nitride in BHF solution, is approximately measured as 65 μm from Figure 4.6. This unexpected increase in the taper length is attributed to unforeseen lower etch rate of annealed nitride in the BHF solution: At first we optimized and calibrated the etching of the adiabatic tapers on dummy wafers for as deposited nitride and prepared the masks accordingly. After the actual process, we found out that the nitride should be annealed in the beginning and that the etch rate of annealed nitride is considerably lower than that of the as deposited nitride. Therefore, the fabricated adiabatic tapers are much longer than expected. As explained in Section 3.3 (Chapter 3), the PSR effect of the tapered mirrors leads to imaging errors if it is ignored. For the fabricated device, another

imaging error comes from the fact that the mirror interfaces are shifted approximately by 51.5 μm (excessive under-etch) towards the waveguides since the length of the tapered interface is 51.5 μm longer than the expected length of 13.5 μm.

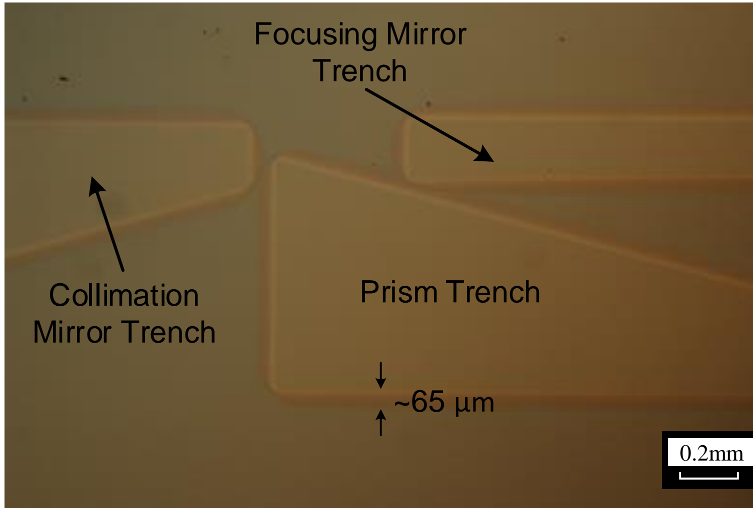

Figure 4.6: A top view photograph of the fabricated device. The main part of the prism in the middle and parts of the mirrors on the left and right hand sides are shown.

4.4 Characterization

We first consider the top view photographs of the fabricated chip made by capturing the light scattered out of the guiding layer, while laser light at 850 nm is coupled into the input waveguide. Figure 4.7 shows the scheme of the optical setup used for taking these photographs. The light of a laser light source at 850 nm is coupled into a single mode optical fiber. Light at the output of this fiber is collimated by a thin lens and then polarized by a polarization beam splitter (PBS). TE polarized light at the output of the PBS excites the input WG of the chip via a microscope objective lens. A camera, which is mounted on a 3-axis translation stage, is used for the photographs of the chip.

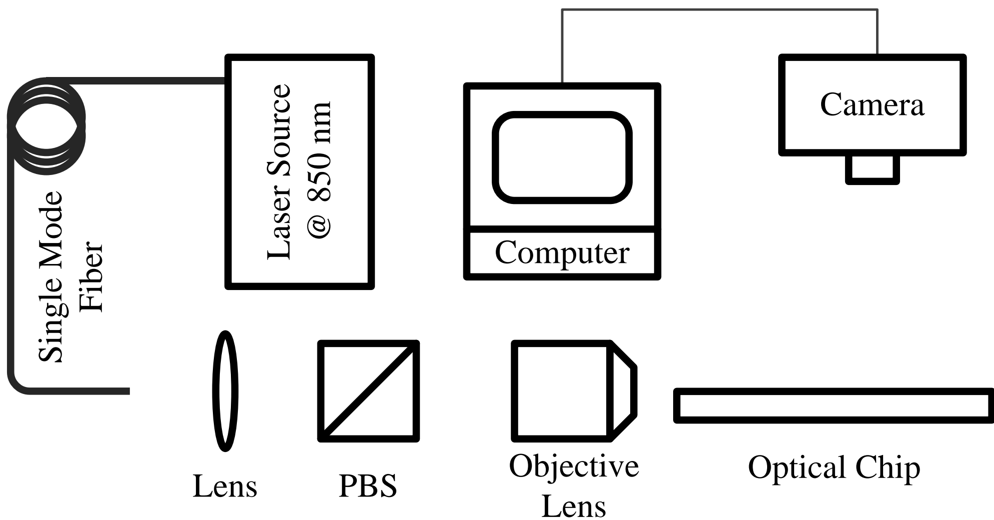

Figure 4.7: Schematic view of the optical setup used for taking the top-view photographs of the fabricated chip.

A set of photographs (all at the same magnification) taken from the different regions of the fabricated chip by is shown in Figure 4.8. The bright dots (except those corresponding to the exit/entrance of input/receiver waveguides) in the pictures are attributed to fabrication errors (either particles formed in the deposition process or regional etching of the guiding layer due to the defects in the masking photoresist), which generate scattering points. The following comments apply to the presented pictures:

(a) The exit of the input waveguide is the bright dot inside the circle. The light starts to diverge after it leaves the waveguide.
(b) The light continues to diverge towards the collimation mirror.

(c) The collimation mirror reflects the light directed to it. A part of the light (left side of the beam) does not reflect from the mirror since the width of the beam is a bit too larger for the size of the collimation mirror.
(d) The light enters the prism. Some scattering is visible at the starting and ending of adiabatic interface.
(e) The light exits from the prism and hits the collimation mirror.
(f) The remaining part of the focusing mirror is seen. It can be seen at the right end of the picture that the light is focused.
(g) The light continues to focus down towards the receiver waveguides. The bright points correspond to scattering defects.
(h) The beam gets narrower towards the receiver waveguides as expected. However, the Gaussian-like profile of the beam is (unexpectedly) not maintained; the upper side of the focused beam is brighter than the other parts. This is attributed to the device imperfections that will be discussed next.
(i) The light reaches the receiver waveguides and it mainly couples into 5 of the waveguides (instead of a single one) as can be seen from the bright points corresponding to the entrance of waveguides. This shows that the positioning of the receiver waveguides is not correct owing to not taking into account the PSR effect and the fabrication error in the taper sections.

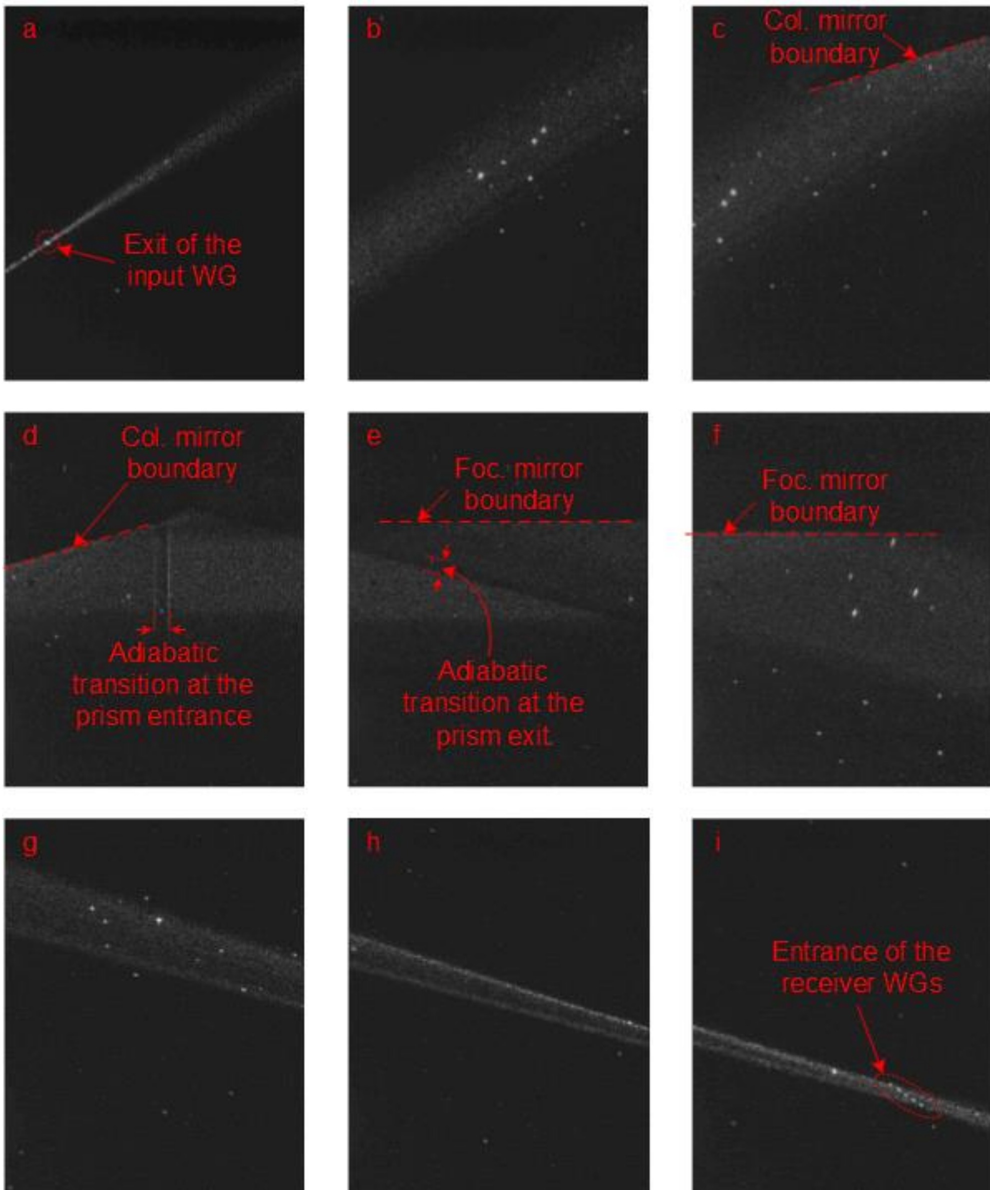

Figure 4.8: The set of photographs taken from the different regions of the fabricated chip while a laser source at 850 nm is coupled into the input waveguide.

We also consider the output spectrum of the receiver waveguides for a white light input to the chip [3]. Figure 4.9 shows the scheme of the setup used for

acquisition of the spectrums. The light of a broadband laser light source (output spectrum between 450 nm to 1700 nm) is coupled into an optical fiber, which is single mode for the operating wavelength range of the chip. Light at the output of this fiber is collimated by a thin lens and then polarized by a PBS. TE polarized light at the output of the PBS excites the input WG of the chip via a microscope objective lens. The light propagating in the waveguide is collimated and goes through the prism. Then it is coupled into the receiver waveguides. The spectrum of a single receive waveguide is obtained by coupling the light inside the waveguide to an optical spectrum analyzer, which is connected to a computer, via a single mode optical fiber. Then the same procedure is applied to the other receiver waveguides.

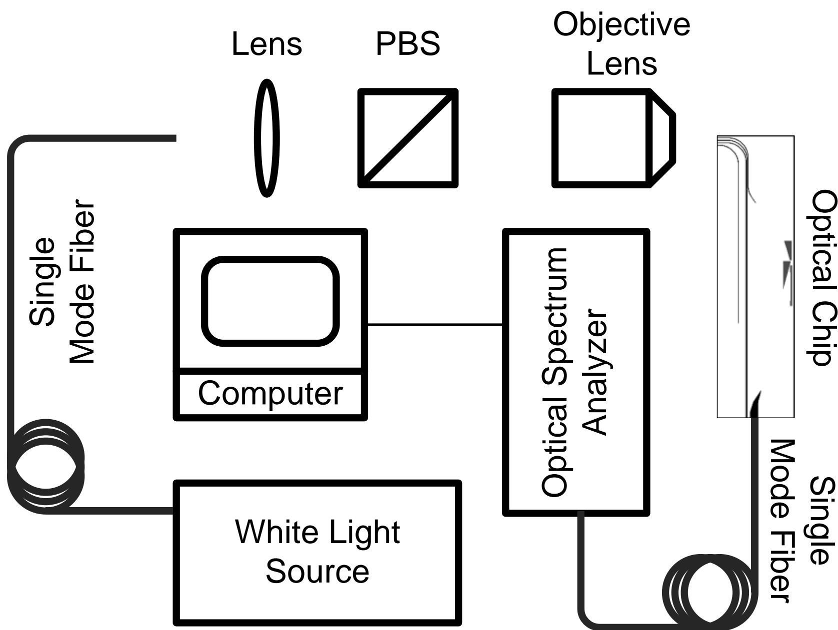

Figure 4.9: Scheme of the setup used for acquisition of the output spectrums from the receiver waveguides for a white light input to the chip.

The experimental results depicted in Figure 4.10, presenting the spectrum of three adjacent waveguides corresponding to the uppermost receiver

waveguides in Figure 4.4, show that the spectrum of each waveguide consists of one major peak and some smaller peaks at the right side of the major peak. The major peaks are found at around 773.7 nm, 778.2 nm and 782.7 nm; the measured channel spacing is about 4.5 nm. Note that, the channel spacing should be 5 nm according to the design as explained above. The decrease in the channel spacing is attributed to the unwanted change in σ' due to un-optimized fabrication process: Considering the material properties (refractive index, thickness, etc.), we rely on the optimizations on dummy wafers but there might be slight differences (due to the tolerances in the deposition and etching processes) in the fabricated device that we were not able to measure. The locations of the major peaks are shifted for this wavelength range by ~2 nm from the expected values (775 nm, 780 nm and 785 nm). For the central wavelength the shift is measured as 10 nm (not shown here), which means that the major peak of λ_c = 850 nm is observed in the waveguide supposed to receive λ = 860 nm. This spectral shift is tried to be understood by considering the aberrations induced by unexpectedly long taper length as discussed next.

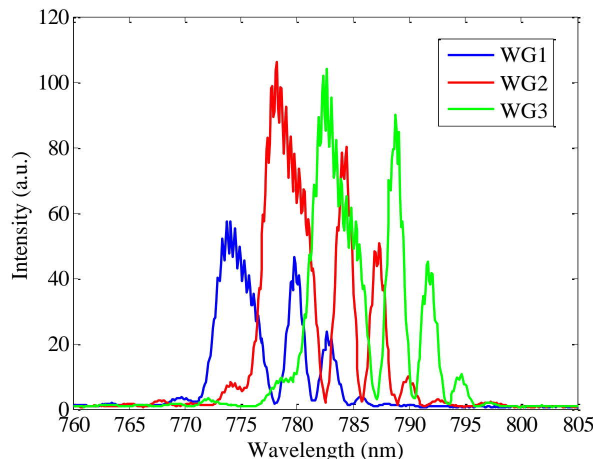

Figure 4.10: The output spectrum of the three receiver waveguides corresponding to the lowest three wavelengths of the considered wavelength region (775 – 925 nm).

The spectral shift mentioned above is estimated for the central wavelength λ_c = 850 nm by considering displacement (due to longer taper length) of the mirror and prism boundaries, and the PSR effect (tilt and GHS) (using the correct (much larger) taper length) of collimation and focusing mirrors. The calculations for estimating the PSR are made by using a 2D layer model for the tapered interface, which is approximated by a staircase (with a sufficiently fine grid for convergence) using indices for the layers equal to the effective indices of the planar structures corresponding to the different thicknesses. The procedure based on channel mode solving, as reported in the previous chapter could not be applied here because the taper length is so long that the mode-solver software cannot properly handle the required computational area. Figure 4.11 shows the phase shift upon TIR vs. incidence angle for the fabricated taper (65 μm long) at λ_c. In applying the 2D ray tracing method, which accounts for the PSR effect by using Equations (3.34) and (3.36) of previous chapter, only to the central ray coming from the input waveguide is considered, corresponding to the modal maximum, in order to find the spectral error. The displacements of the ray at the prism interfaces are also considered in the calculations, using a staircase approximation for the taper section. The ray tracing result, where considered ray hits the waveguide next to that for the central wavelength, shows that the spectral error for λ_c is 5 nm whereas it is 10 nm in the measurements. This difference is attributed to small errors in the fabrication process (refractive index or thickness of nitride layer can be slightly different than the values used in the design).

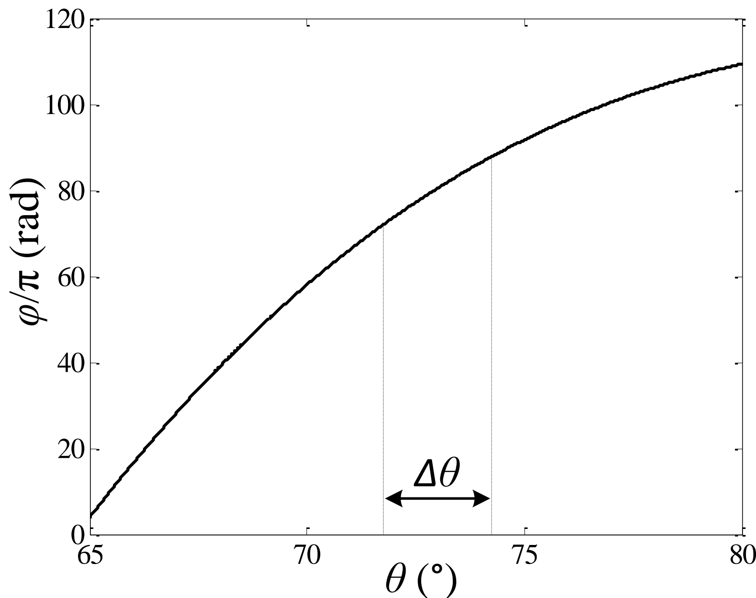

Figure 4.11: Phase shift upon TIR vs. incidence angle for the fabricated interface with 65 μm taper length at λ = 850 nm. $\Delta\theta$ is the used incidence angle range for both the mirrors.

The image break up as can be observed in Figure 4.10 cannot be explained by ray tracing calculations. The image break up observed in the experiments could be due to device imperfections (of which we do not know the origin). The excitation of higher-order modes within the high V-number waveguides as a cause for the image break-up seems not likely owing to the adiabatic tapering (taper angle 0.1˚).

4.5 Conclusions

We have designed, fabricated and characterized a prism spectrometer based on adiabatically connected waveguiding slabs having different thicknesses. The device is designed to work for TE polarized light at a central wavelength of 850 nm over a wavelength range of 100 nm with a channel spacing of 5

nm. At the time that the design of the device was made the PSR effect was underestimated and not taken into account.

It was found from photographs that the length of the adiabatic tapering, connecting the applied waveguiding slabs, was too long, owing to an error in the etching process. The consequence of this is an enhanced PSR effect (according to calculations) and a displacement of (among other things) the used parabolic mirror interfaces.

Exciting the structure with light at the central wavelength and taking photos of the light scattered from the various parts of the chip it was found that, as anticipated based on the above over length of the tapering, that the light was not well focused onto the output waveguide. Measuring the output spectra of a few output waveguides confirmed the latter and also showed an unexpected and unexplainable peak break-up in addition to peak broadening. The wavelengths captured by the different output waveguides were approximately the correct ones. The angular dispersion of the beams emerging from the prism was found to have approximately the design value with an error of 10%.

4.6 References

[1] H. Kogelnik, "An introduction to integrated optics." *Microwave Theory and Techniques, IEEE Transactions on,* vol. 23, pp. 2-16, 1975.

[2] K. Wörhoff, P. V. Lambeck, and A. Driessen, “Design, tolerance analysis, and fabrication of silicon oxynitride based planar optical waveguides for communication devices,” *J. Lightwave Technol.,* vol. 17, pp. 1401-1407, 1999.

[3] B. I. Akca, “Spectral-domain optical coherence tomography on a silicon chip,” PhD thesis, Univ. of Twente, 2012.

5 Integrated Optics Polarization Splitter: Design, Fabrication and Testing

We describe the design, fabrication and characterization of an on-chip polarization splitter in adiabatically connected slab WGs. The polarization splitter is operated at a central wavelength of λ_c = 850 nm, which is chosen such that the device is compatible with the prism spectrometer described in the previous chapter. The device is implemented in a Si_3N_4 layer sandwiched between SiO_2 layers and it can be fabricated with the same fabrication procedure as for the integrated prism spectrometer described in the previous chapter.

5.1 Introduction

In a single mode waveguide, two orthogonally polarized modes can be present at the same time. This simultaneous presence of the two modes can cause problems due to polarization sensitivity of optical components in the system [1]. Discrete processing of TE and TM polarization components via polarization splitters, which may also serve as combiners, can solve this problem [2]. Planar polarization splitter devices are very advantageous since they can be combined with integrated optical (IO) systems on the same substrate. A number of planar polarization splitter devices with different working principles have been studied in the literature such as directional coupler and asymmetric Y junction based structures [3, 4]. In addition, birefringent Mach-Zehnder interferometers and multimode interference couplers are being used as planar polarization splitters [5, 6]. Slab waveguide based polarization splitting trenches are also implemented but were never fully integrated with input and receiver waveguides [7].

In this chapter, we will introduce the design, fabrication and characterization of on-chip polarization splitters in adiabatically connected slab waveguides (having two different thicknesses). The principles of 2D geometrical optics and diffraction theory are used to model the device. As it is the case for the fabricated prism spectrometers explained in the previous chapter, the main aim of this research was to demonstrate experimentally the polarization splitting capability of the presented. Therefore, the device parameters were chosen to lead to a functioning yet not necessarily fully optimized device. Here, the fabrication process will not be discussed in detail since the devices were fabricated using exactly the same process that we use to fabricate the prism spectrometers.

The rest of this chapter is organized as follows. First, we will introduce the principle related to the polarization splitter in Section 5.2. Then, the design of this device will be presented in Section 5.3, where the fabrication process of the device will also be mentioned briefly. This is followed by a description of the experimental characterization of the fabricated device in Section 5.4. The chapter ends with conclusions (Section 5.5).

5.2 Device Principle

A schematic of the considered polarization splitter device is shown in Figure 5.1. It is composed of an input waveguide, an elliptical mirror, a polarization splitting trench and two receiver waveguides, corresponding to the two polarizations. The input and receiver waveguides are ridge WGs with an effective index of N_g for the slab corresponding to the ridge section. The polarization splitter and the mirror are made at the same technological step (nitride etching in BHF) for simplicity of fabrication. The regions of different slab thicknesses are connected via adiabatic vertical tapers, which minimize reflection losses at the polarization splitting trench interfaces and minimize polarization conversion on reflection from the elliptical mirror as it is explained in chapter 3 for the parabolic mirror.

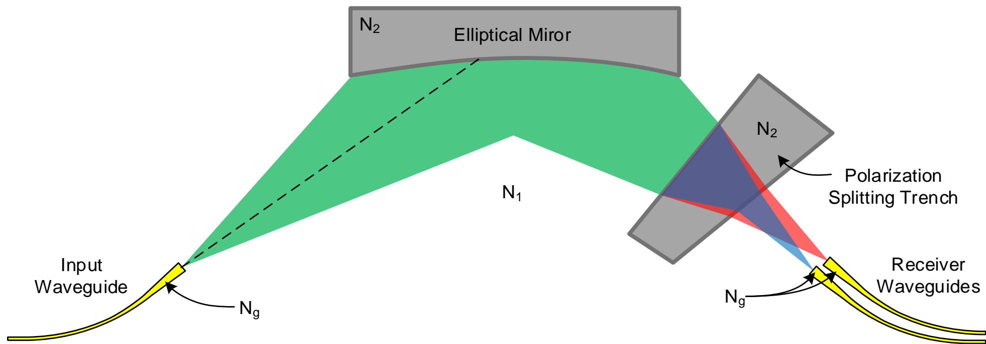

Figure 5.1: Schematic of the polarization splitter. The white and grey areas correspond to thick and thin slabs, respectively. Ridge waveguides are indicated by yellow lines. The capitals N refer to the effective index of the planar structures corresponding to the indicated regions.

The working principle of the proposed polarization splitter is as follows. The input WG is tapered up over a length of 1 mm from the width of a single mode WG (1 μm in the present case) to a certain width corresponding to the desired modal width chosen such that the geometrical aberrations for focused fields at the entrance of the receiver waveguides are minimized as it is explained below, in Section 5.3. Light carried by the waveguide diverges in the thick slab and then starts converging after reflection from the elliptical mirror. The latter is an elliptical total internal reflection (TIR) mirror for slab modes defined by the interface between thick (high modal index, N_1) and thin (low modal index, N_2) slab sections. The converging light beam enters the polarization splitting trench where the different polarization components are angularly dispersed. The polarization splitter slab shown in the figure is similar to the thin film polarizer described in [7], but here we use a trench with non-parallel edges in order to minimize geometrical aberrations at the output as will be explained in the next section. The output beams leaving the polarization splitter slab are then further converging onto receiver waveguides, corresponding to the different polarizations. The receiver waveguides are tapered down to a width corresponding to single mode

operation for preventing the unwanted occurrence of higher order guided modes and optical coupling between the receiver waveguides.

5.3 Design

The proposed device is implemented in SiON WG technology by using a Si_3N_4 layer sandwiched between buffer and cladding SiO_2 (oxide). The fabrication process steps are exactly the same as the ones used for the prism spectrometer and will not be described here. Although the nitride deposition and etching thicknesses in the fabrication can be optimized specifically for the polarization splitter, these thicknesses are chosen equal to those for the prism spectrometer, for convenience of fabrication. So, the polarization splitters have been fabricated together with the prism spectrometers on the same substrate. The nitride thicknesses and corresponding effective refractive indexes for TE and TM polarizations at λ_c can be seen in Table 5.1.

Table 5.1: Thicknesses for the different chip regions indicated in Figure 5.1 and the effective refractive indexes of the corresponding slabs, for TE and TM polarizations at λ_c.

Thickness	TE N_{eff}	TM N_{eff}
t_1 = 160 nm	N_{1TE} = 1.6785	N_{1TM} = 1.5717
t_2 = 40 nm	N_{2TE} = 1.4785	N_{2TM} = 1.4611
t_g = 175 nm	N_{gTE} = 1.7003	N_{gTM} = 1.5919

5.3.1 Elliptical Mirror

An ellipse can be defined as the set of all points in a plane, for which the sum of the distances from two fixed points in the plane (the foci) is constant [8]. Therefore, according to Fermat's principle, all rays originating from one of the foci of an elliptical mirror and travelling via the mirror will pass through the other focus [9]. Figure 5.2 shows the schematic of the elliptical mirror, which is the portion of a full ellipse and symmetric around point A, corresponding to the centre of the mirror. The exit of the input waveguide is at one of the foci, which is at (0,0), and the other focus is at (x_f,0). In this figure (x_1,y_1) and (x_n,y_n) are the first and last points on the mirrors, respectively, θ_l and θ_h are the smallest and largest incidence/reflection angles on the mirror, γ is the angle between the outermost rays, α is the angle between the lower outermost ray from the input waveguide and the x-axis, $\tilde{B}$ is the width of the reflected part of the diverging beam at the entrance of the mirror and it is equal to the width of the converging beam at the exit of the mirror, f is the distance between point (0,0) and B and it is equal to the distance between point C and (x_f,0), for reasons of symmetry. Here, w_o can be considered as a virtual aperture, which defines the truncation of the input field by the finite size of the mirror, for the input field at a distance of f. The far field of the input beam with a full width at half maximum (FWHM) of W at a distance of f can be found via the V parameter of the input waveguide and the truncation parameter ς, defined by $\tilde{B} = \varsigma W$. Note that a combination of two parabolic mirrors can also be used instead of elliptical mirror for the polarization splitter. The advantage of using only one elliptical mirror is reduction of the PSR (phase shift upon reflection) effects since there is only one mirror involved in the device. Futhermore, PSR effect are reduced due to a smaller incidence angle range ($\Delta\theta = \theta_h - \theta_l$), implying a smaller range for the PSR ($\varphi(\theta_h) - \varphi(\theta_l)$; see Figure 3.13 of Chapter 3).

The equations related to the elliptical mirror design can be derived as follows. Denoting the mirror coordinates by (x, y) it follows [10]:

$$\sqrt{x^2 + y^2} + \sqrt{(x_f - x)^2 + y^2} = d_0, \tag{5.1}$$

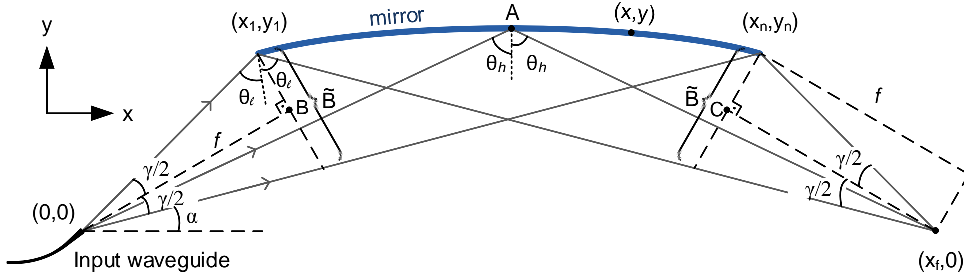

Figure 5.2: Schematic of the elliptical mirror introducing the used symbols.

where d_0 is a constant (equal to the path length between the two foci for a ray reflected by the mirror). Next we will show that the elliptical mirror (shape and size) is fully defined by the quantities γ, θ_l and f. It follows from geometry by considering the triangle formed by the two foci and the point (x_1,y_1) that

$$\alpha = \frac{180^\circ - 2\theta_l - \gamma}{2}, \tag{5.2}$$

$$\frac{y_1}{x_1} = \tan(\alpha + \gamma), \tag{5.3}$$

and

$$\sqrt{(x_1{}^2 + y_1{}^2)}\cos(\gamma/2) = f. \tag{5.4}$$

By using Equations (5.2), (5.3) and (5.4) expressions for x_1 and y_1 can be found. Then, with $x_f = (y_1/\tan\alpha) + x_1$ we find

$$x_n = x_f - x_1. \tag{5.5}$$

Substituting x_1, y_1 and x_n in Equation (5.1), d_0 can be found. Then, the mirror curve can be derived since both x_n and d_0 are known.

As explained in the introduction of this chapter, our focus was to make a functioning device that does not have to be fully optimized. At the time that the design of the device was made the PSR effect was underestimated (there were no models available back then) and not taken into account. Therefore, the design parameters for mirror (γ, θ_l, f) and input waveguide (V) are varied to minimize the geometrical aberration effects caused by the trench. To that end the lowest angle of incidence/reflection (θ_l) is chosen well above θ_{crit} (for TM polarization; guaranteeing also TIR for TE polarization) $\theta_l = \theta_{crit} + 10°$. By choosing θ_l large, the effect of the PSR (although the PSR effect was not taken into account it was known, from a rough estimation, that the PSR effects exist) is reduced as explained in the Section 3.3 of Chapter 3. The other parameters related to the mirror being γ and f are chosen such that $\Delta\theta$ is rather low to reduce the geometrical aberration effects. The origin of these aberrations can be explained as follows: The rays are reflected from the elliptical mirror such that they converge without any aberrations (ignoring the PSR effect) if there would be no polarization splitting trench. However, since each ray enters the trench with a different angle, the relative angles between the rays change at the output of the trench. Therefore, there is a focal spread at the entrance of the receiver waveguides causing imperfect imaging. The V parameter of the input waveguide is chosen rather high for further reducing the geometrical aberration effects. By choosing a large V parameter the FWHM of the modal intensity (w_m) of the input waveguide at the taper end is increased which leads to a lower angular spread and so to less effect of the geometrical aberrations. Here, a full optimization for the device parameters has not been done as explained previously, they were chosen to attain a reasonably well device performance as to the losses due to geometrical aberrations. The chosen parameters for

the mirror and input waveguide are listed in Table 5.2. These choices lead to $\Delta\theta = 0.6°$, $\varsigma = 1.28$, $w_m = 4.98$ µm for TE and $w_m = 5.05$ µm for TM.

Table 5.2: Design parameters chosen for the elliptical mirror and input waveguide.

	Parameters	**Values**
Elliptical Mirror	γ	7.85°
	θ_l	77.9°
	f	2.076 mm
Input Waveguide	V	13

It should be noted that the elliptical mirror is not a perfect imaging device for the following reason. As is seen from Figure 5.2, the central ray coming from the input waveguide does not hit point A, which is the midpoint of the mirror. Consequently, the central ray at the output focus does not originate from the central ray of the input field. Therefore, overlap losses will occur at the input of the receiver waveguides due to a asymmetric image field at the output focus. This loss is estimated by making a 2D beam propagation method (BPM) based simulation, in which the polarization splitting trench is omitted for convenience. The simulations have been done only for TE polarization and the effective index method is used for dimensionality reduction to 2D. We assumed a device lay-out according to the parameters given in Table 5.2. We put a receiver waveguide at $(x_f,0)$ with the same V number as used for the input waveguide. The mirror is defined such that the

adiabatically tapered mirror region has a width of 14 μm, which is the expected vertical taper length before starting the fabrication. The simulation results show that the optical power in the input waveguide couples into the receiver waveguide with a functional loss of 0.86 dB including the truncation losses.

5.3.2 Polarization Splitting Trench

The polarization splitting principle of the considered device is based upon the birefringence of slab waveguides, meaning that in each slab the effective refractive indexes of the (zero-order) guided modes for TE and TM polarizations are different. Figure 5.3 shows the schematic of the polarization splitting trench, a crucial part of the splitting device. The rays depicted in Figure 5.3 initiate from the output part of the elliptical mirror with a virtual aperture of $\tilde{B}$ and the distance between the starting point of the central ray and original (i.e., without trench) focal point of the mirror is f. The polarization splitting trench can be configured either with an exit interface, which is parallel to the entrance interface [7], or a rotated one. In this study, we have chosen the parameters related to the polarization splitter trench by first considering the parallel exit interface condition. After the trench has been optimised for that situation (orientation and width) the rotation angle (η) of the exit interface is empirically optimized by using ray tracing to minimize the geometrical aberrations induced by the trench. The geometrical aberrations are caused by the unequal change in optical path difference of the rays inside the trench. The complete design procedure of the polarization splitting trench will be given next.

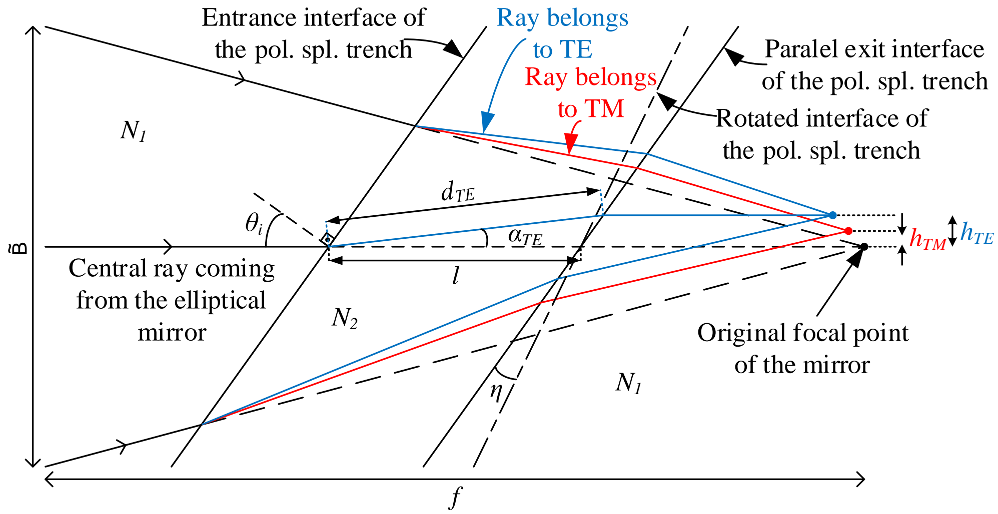

Figure 5.3: Schematic of the polarization splitting trench and used symbols. The rays correspond to the situation with a parallel exit interface.

We will first derive the expression for the optimal distance between the two foci for the case with the parallel exit interface. In Figure 5.3, the blue and red coloured rays correspond to TE and TM polarizations, respectively. All the rays entering the polarization splitting trench will leave the trench with a direction parallel to its original direction. Therefore, the central rays of different polarization components will be parallel to each other at the output of the trench. The vertical distance ($w_s = h_{TE} - h_{TM}$) between the TE and TM focal points can be found by tracing only the central rays of different polarizations components for the parallel exit interface case as follows. The refraction angles at the entrance interface of the polarization slab can be found by using Snell's Law:

$$\alpha_{TE} = \sin^{-1}(N_{1TE} \sin \theta_i / N_{2TE}) - \theta_i, \tag{5.6}$$

$$\alpha_{TM} = sin^{-1}(N_{1TM}\, sin\, \theta_i / N_{2TM}) - \theta_i\,, \tag{5.7}$$

where, θ_i is the angle of incidence of the central incoming ray, α_{TE} and α_{TM} are refraction angle at the entrance interface for TE and TM polarizations, respectively, N_{1TE} and N_{1TM} are effective refractive indexes of the region outside the polarization splitting trench for TE and TM polarizations, respectively, N_{2TE} and N_{2TM} are effective refractive indexes of the region inside the polarization splitting trench for TE and TM polarizations, respectively. It follows from the geometry that

$$h_{TE} = \frac{l\cos\theta_i}{\cos(\theta_i + \alpha_{TE})}\sin\alpha_{TE}, \tag{5.8}$$

$$h_{TM} = \frac{l\cos\theta_i}{\cos(\theta_i + \alpha_{TM})}\sin\alpha_{TM}\,. \tag{5.9}$$

The vertical distance (w_s) between TE and TM outputs can be expressed by,

$$w_s = \frac{l\cos\theta_i}{\cos(\theta_i + \alpha_{TE})}\sin\alpha_{TE} - \frac{l\cos\theta_i}{\cos(\theta_i + \alpha_{TM})}\sin\alpha_{TM}. \tag{5.10}$$

This equation shows that w_s is defined by two parameters; l and θ_i. Equation (5.10) shows that w_s changes linearly with l. Figure 5.4 shows w_s as a function of θ_i, up to a value of around 2° below the critical angle for reflection (61.7°). For this graph, l is taken as 1 μm. Considering for the moment only the vertical separation between foci it follows that for a large focal separation the values for l and θ_i should be chosen as large as possible. However, the focal spread (w_{fs}), due to geometrical aberrations (caused by the polarization splitting trench owing to the fact that the rays corresponding to a certain polarization do not go exactly through the same (focal) point), at the output increases when l and θ_i are increased for the parallel exit interface case. By empirically optimizing η after choosing l and θ_i, geometrical aberrations can, to a certain extent, be decreased at the expense of a small decrease in w_s. The optimization of η can be explained as follows. The focal

spreads at the foci corresponding to different polarizations are calculated for different η values by using ray tracing. Then, η is chosen such that the focal spreads are minimized without a significant decrease of w_s.

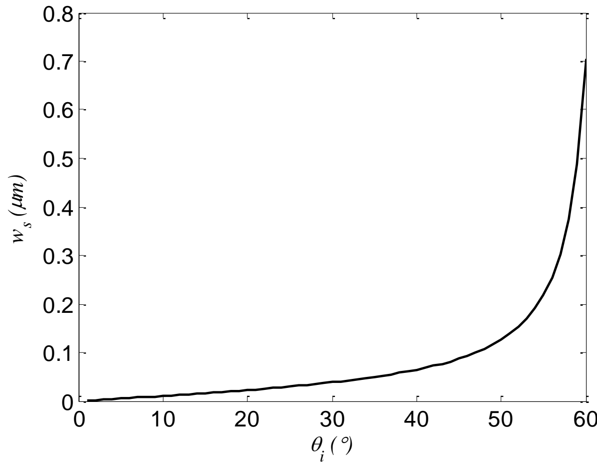

Figure 5.4: Vertical separation between TE and TM focal points (w_s) as a function of incidence angle of the central ray (θ_i) up to the angle 2° below critical angle for reflection (61.7°).

As mentioned in the previous section, our focus was to make a functioning device that does not have to be fully optimized. The parameters for the polarization splitter trench are chosen such that the separation between the output waveguides corresponding to different polarization components is wide enough to have negligible cross talk, which is confirmed by mode solver based calculations of the waveguide coupling.

Table 5.3 shows the chosen design parameters for the polarization splitting trench. For the parallel exit interface condition these choices lead to w_s = 33.6 μm, w_{fs} = 1.05 μm for TE and w_{fs} = 0.51 μm for TM. For angled (with given η in Table 5.3) exit interface case, w_s decreased to 28.9 μm, w_{fs} reduced to 0.95 and 0.36 for TE and TM, respectively. Note that the focal

spread for the two polarizations is negligible with respect to the width of the waveguide modes ($w_m = 5.1$ µm).

The resulting layout of the fabricated polarization splitter chip, which has a size of 4.2 x 13.8 mm^2 including the input and output waveguides, is shown in Figure 5.5. There are two receiver waveguides corresponding to the TE and TM polarizations. The reference waveguides, which can be seen in Figure 5.5, are placed for measuring losses in the spectrometer but these loss measurements have not be performed due to lack of time. By applying bends in the input WGs only a small part of the stray light generated at the input of the chip interferes with the polarization splitter.

Table 5.3: Parameters chosen for the polarization splitter slab.

Parameter	Value
θi	22.6°
l	1250 µm
η	12.9°

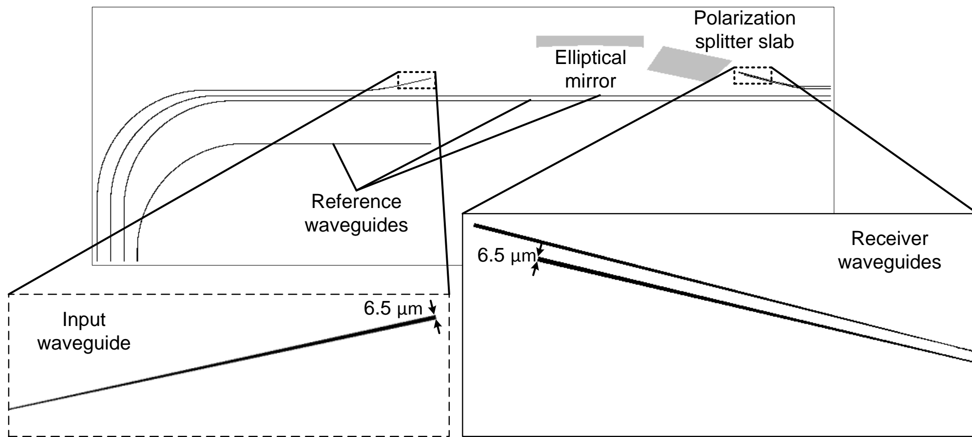

Figure 5.5: Full layout of the fabricated polarization splitter, which has a size of 4.2 x 13.8 mm^2. The figures at the bottom show the input and receiver waveguides in detail.

5.4 Characterization

Top view photographs of the fabricated chip were obtained by capturing the light scattered out of the structure, while laser light at 850 nm is coupled into the input waveguide. Figure 5.6 shows the schematic of the optical setup used for taking these photographs. The light of the laser is coupled into a single mode optical fiber. Light at the output of this fiber is collimated by a thin lens and then polarized by a polarization beam splitter (PBS). The polarized light then travels through a λ/2 plate in order to choose the desired polarization of the light that will be coupled into the chip. The polarized light at the output of the λ/2 plate excites the input WG of the chip via a microscope objective lens. A camera, which is mounted on a 3-axis translation stage, is used for the photographs of the chip.

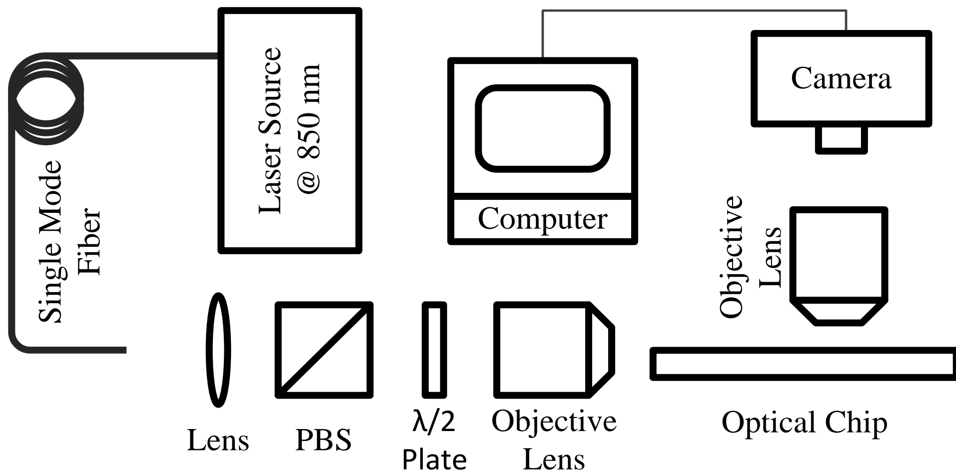

Figure 5.6: Schematic view of the optical setup used for the taking top view photographs of the fabricated polarization splitter chip.

A set of photographs (all at the same magnification) taken from the different regions of the fabricated chip is shown in Figure 5.7. The first four photos (a-d) were taken while the input is mixed polarized light, (e, f) were taken while the input is TE polarized light and (g, h) were taken while the input is TM polarized. Here, (e) and (g) were taken without changing the position of camera and (i) is obtained by placing a transparent version of (e) on top of (g). The bright dots (except for those corresponding to the exit/entrance of input/receiver waveguides) in the pictures are attributed to fabrication errors (either particles formed in the deposition process or local etching of the guiding layer due to the defects in the masking photoresist), which generate scattering points. The following comments apply to the presented pictures:

(a) The exit of the input waveguide is indicated by the dashed circle, marking the place where the light starts to diverge after it leaves the waveguide.

(b) The elliptical mirror reflects the light. Then, the light starts to focus toward the polarization splitting trench.

(c) The focusing light enters the polarization splitting trench through the adiabatic vertical taper. Some increased scattering is visible at the entrance and exit of the adiabatic taper.

(d) The light exits from the polarization splitting trench. The beam gets narrower towards the receiver waveguides as expected. However, the Gaussian like profile of the beam is not maintained (similar as in the case for fabricated spectrometer (Section 4.4 of Chapter 4)): the lower side of the focused beam is brighter than the other parts for unknown reasons.

(e) TE polarized light is focused towards the receiver waveguides and excites the one corresponding to TE polarization. As can be seen, part of the light does not couple into any of the receiver waveguides as a result of overlap losses at the entrance of the waveguide. These losses are attributed to defocusing and tilt errors due to the unexpected vertical taper length and not taking into account the PSR effect.

(f) The light that excites the TE receiver waveguide is coupled out of the chip through the exit of the TE receiver waveguide. The part of the light that does not couple into any of the receiver waveguides propagates in the slab and couples out via an end-facet of the chip.

(g) TM polarized light is focused towards the receiver waveguides and excites the one corresponding to TM polarization. By visual inspection of the photographs it seems that a relatively large amount of TM light is coupled into the corresponding WG.

(h) The light that excites the TM receiver waveguide is coupled outside of the chip through the exit of the TM receiver waveguide.

(i) This figure is the combined version of (e) and (g) and shows a clear separation between the beams corresponding to TE and TM polarizations.

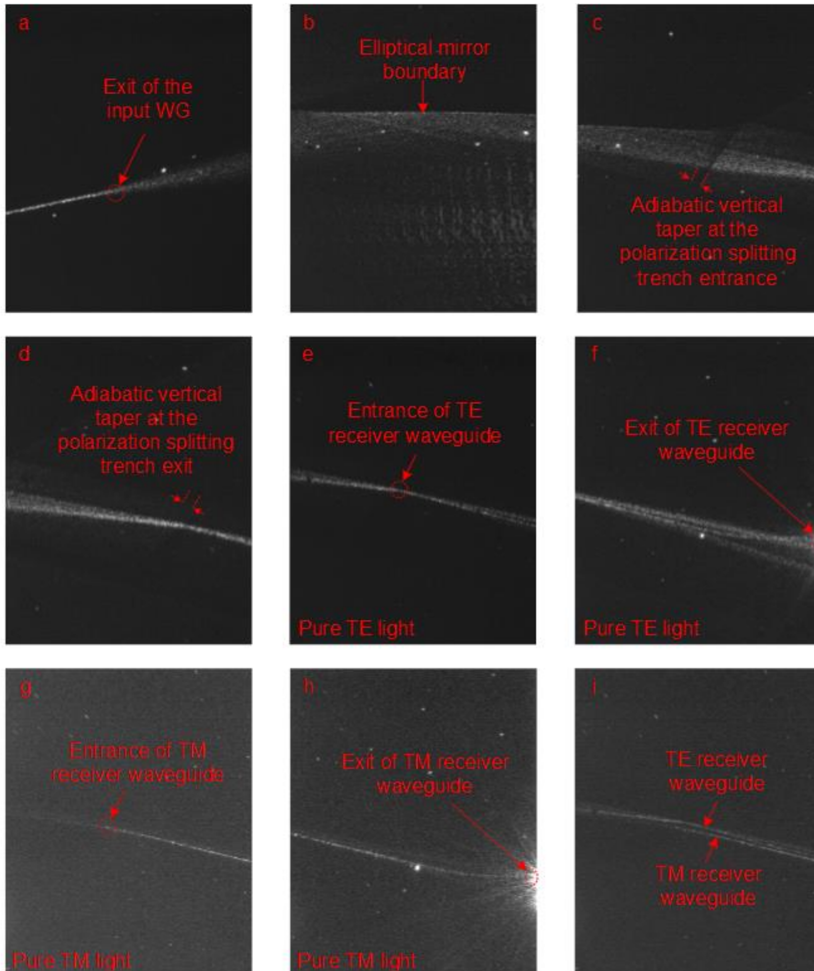

Figure 5.7: The set of photographs taken from the different regions of the fabricated chip while a laser source at 850 nm is coupled into the input waveguide. The first 4 photos were taken while the input is mixed polarized light, (e) and (f) were taken while the input is TE polarized light, (g) and (h) were taken while the input is TM polarized light, (i) is the combined version of (e) and (g).

From the above study we conclude the following:

1. The combination input WG, elliptical mirror and polarization trench lead, as desired, to the spatial splitting of TE and TM polarized light.
2. The PSR effect was not taken into account in the design leading to mismatch between device image and mode profiles of the output WGs.

5.5 Conclusions

We have designed and fabricated an on-chip polarization splitter for light guided by channel waveguides using an elliptic mirror for focusing and a polarization splitting trench. The mirror and trench were based on adiabatically connected waveguiding slabs. In the design the PSR effect are not taken into account and the focal spreads for the two polarizations, owing to geometrical aberrations at the output foci, are used as performance parameter. In order to minimize these spreads a trench with non-parallel interfaces is considered. Characterization results show that the polarization splitter is working approximately as expected, except for losses at the entrance of the receiver waveguides due to imperfect imaging. This discrepancy is attributed to the combined effect of an error in the fabrication (leading to too long tapers) and neglecting the PSR effect.

5.6 References

[1] A. Tervonen, “Integrated optical polarization splitters," *IEE Colloquium on Polarisation Effects in Optical Switching and Routing Systems*, pp. 1-3, Institution of Electrical Engineers, London, 1990.

[2] L. G. Kazovsky, “Phase- and polarization-diversity coherent optical techniques,” *J. Lightwave Technol.*, vol. 2, pp. 279-292, 1989.

[3] H. Maruyama, M. Haruna and H. Nishihara, “TE-TM mode splitter using directional coupling between heterogeneous waveguides in $LiNbO_3$,” *J. Lightwave Technol.*, vol. 13, pp. 1550-1554, 1995.

[4] R.M. de Ridder, A.F.M. Sander, A. Driessen and J.H. Fluitman, “An integrated optic adiabatic TE/TM mode splitter on silicon,” *J. Lightwave Technol.*, vol. 11, pp. 1806-1811, 1993.

[5] L.B. Soldano, A.H. de Vreede, M.K. Smit, B.H. Verbeek, E.G. Metaal and F.H. Groen, “Mach-Zehnder interferometer polarization splitter in InGaAsP/InP,” *IEEE Photonics Technology Letters*, vol. 6, pp. 402-405, 1994.

[6] J.M. Hong, H.H. Ryoo, B.H. O, S.G. Lee, E.H. Lee, D. Woo, and S. Kim, “Novel design of polarization splitter based on a quasistate multimode interference coupler,” *in CLEO’2002 Tech. Dig.*, pp. 194–195, 2002.

[7] P. Tien, "Integrated optics and new wave phenomena in optical waveguides," *Reviews of Modern Physics,* vol. 49, pp. 361-420, 1977.

[8] G.B. Thomas, R.L. Finney and M.D. Weir, “Calculus and analytic geometry (Vol. 7),” MA: Addison-Wesley, 1998.

[9] A. Ghatak, “ Optics (4th Edition),” New Delhi: Tata McGraw Hill, 2009.

[10] V.V. Prasolov and V.M. Tikhomirov, “Geometry,” American Mathematical Society, 2001.

6 Semi-guided Plane Wave Reflection by Thin-Film Transitions for Angled Incidence[2]

The non-normal incidence of semi-guided plane waves on step-like or tapered transitions between thin film regions with different thicknesses, an early problem of integrated optics, is being reconsidered. Accepting the scalar approximation, using an ansatz of harmonic field dependence on the position along the interface, the 3-D problem reduces to a 2-D Helmholtz problem, for guided wave input and transparent-influx boundary conditions, with an effective permittivity that depends on the incidence angle.

6.1 Introduction

Classical concepts [1, 2] for integrated optical components like lenses [3, 4], mirrors [5], prisms [6], but also for complex lens-systems [7], or, more recently, for entire spectrometers as we explained in Chapter 3, rely on the effects that a transition between regions with different layering has on thin-film guided, in-plane unguided waves (semi-guided waves). Specifically, this concerns tapered or step-like transitions between regions with different core thicknesses. Results for the reflection and refraction of 1-D guided plane waves at such a discontinuity may form the basis for a description of the in-plane propagation by geometrical optics [1, 2]. Figure 6.1 provides a schematic view of the problem under consideration. One might be tempted to

[2] This chapter has been published as: F. Civitci, M. Hammer, and H.J.W.M. Hoekstra, "Semi-guided plane wave reflection by thin-film transitions for angled incidence," Optical and Quantum Electronics, vol. 46, pp. 477-490, 2014.

reduce the actual 3-D problem of Figure 6.1 to two spatial dimensions by what is known as “effective index method” [10], i.e. by representing the regions of different film thicknesses in terms of the effective modal indices of properly polarized slab waveguide modes, followed by applying the classical Fresnel-expressions [11] for reflection and transmission of plane waves under angled incidence. Unfortunately, this approach is more questionable (radiation losses, ill-defined effective index [10]) even for the case of normal incidence. For angled incidence, one additionally neglects any effects due to the vectorial nature of the problem (wave hybridization).

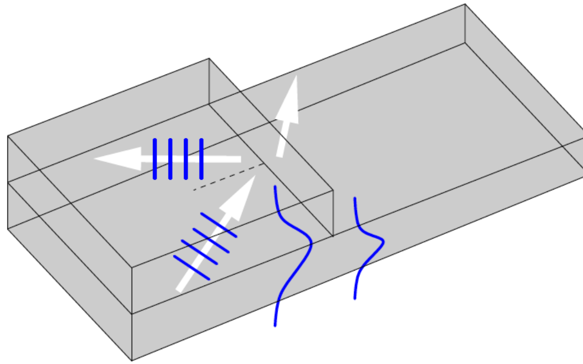

Figure 6.1: Incidence of vertically guided, laterally unguided plane waves under an angle on a step discontinuity between regions with different core film thicknesses. Primary interest is in the relative amplitude, and in the phase, of the reflected semi-guided wave, typically as a function of the angle of incidence. This phase change, or more precisely its angular derivative, determines the lateral displacement, the so-called Goos-Hänchen shift, of an in-plane-guided beam upon reflection at the transition [8, 9].

In this chapter, we introduce the theoretical modeling for angled incidence of the semi-guided waves to a tapered or step-like discontinuity by using the scalar 2-D Helmholtz equation. The respective background is being outlined in Section 6.2. In Section 6.3, simulation results for a step discontinuity and for a series of tapered transitions are discussed. Moreover, these results are

compared with the results that we obtained with the transverse resonance condition based method used for calculating phase shift upon total internal reflection in Chapter 3. The chapter ends with conclusions in Section 6.4.

6.2 Scalar Theory

For simplicity we first look at a step discontinuity, as illustrated schematically in Figure 6.2. What follows relies on the approximation that, for the problem in question, polarization effects originating from interfaces or permittivity gradients can be disregarded. Neglecting the corresponding derivatives, the original Maxwell equations [11] turn into to the scalar Helmholtz equation,

$$\left(\partial_x^2 + \partial_y^2 + \partial_z^2\right)\tilde{E} + k^2\epsilon\tilde{E} = 0, \tag{6.1}$$

where $\tilde{E}$ is optical electric field oscillate in time $\sim exp(i\omega t)$ with frequency $\omega = kc = 2\pi c/\lambda$, for vacuum wavenumber k, wavelength λ, speed of light c, permittivity ϵ_0. Structural information is given by the relative permittivity $\epsilon = n^2$, or by local values for the refractive index n.

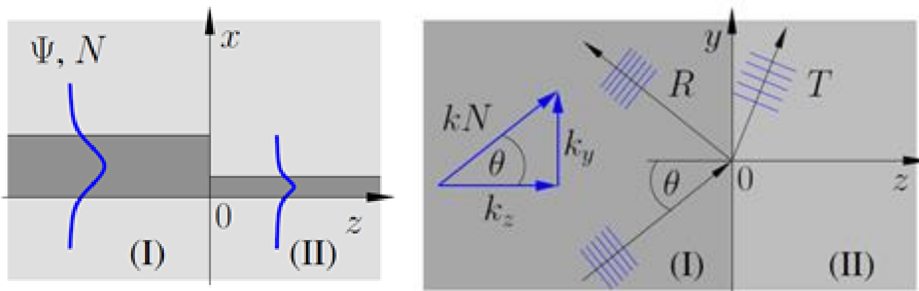

Figure 6.2: Step discontinuity, cross sectional and top views, with the relevant wave vectors and angles indicated.

Motivated by the y-homogeneity of the problem $\partial_y \epsilon = 0$, one adopts an ansatz of harmonic y-dependence for the scalar field $\tilde{E}$:

$$\tilde{E}(x, y, z) = E(x, z)e^{-ik_y y}. \tag{6.2}$$

In region (I), $z < 0$, a slab mode with x-profile and effective mode index N, nonguided in the y- and z-directions, is supposed to be coming in at an angle θ:

$$\tilde{E}_{in}(x, y, z) = \Psi(x)e^{-ikN(\sin\theta y + \cos\theta z)}, \quad \partial_x^2 \Psi + k^2(\epsilon_I - N^2)\Psi = 0. \tag{6.3}$$

This incoming wave $\tilde{E}_{in}$ must satisfy the previous ansatz (6.2). Consequently, the lateral wavenumber k_y has to be related to the angle of incidence as

$$k_y = kN \, sin \, \theta. \tag{6.4}$$

One is left with the effective scalar problem

$$(\partial_x^2 + \partial_z^2)E + k^2 \epsilon_{eff} E = 0, \text{ with } \epsilon_{eff}(x, z) = \epsilon(x, z) - N^2 \, sin^2 \, \theta, \tag{6.5}$$

which is to be solved on a 2-D computational domain. Note that Equation (6.5) emerges as well if one neglects the permittivity derivatives ($\partial\epsilon = \epsilon\partial$) in the elements of the matrix operators of Equations (6.3), (6.4).

In principle, any suitable 2-D Helmholtz (scattering) solver for scalar TE fields could be applied. The outcome will be the field in the computational domain, or a numerical representation thereof, which, in region (I), can be given the form

$$E_I^2(x, y, z) = \{\Psi(x)(e^{-ikNcos\theta z} + \rho e^{ikNcos\theta z}) + \chi(x, z)\}e^{-ikNsin\theta y}, \tag{6.6}$$

where χ is assumed to be orthogonal to the incoming profile, $\int \chi(x,z)\Psi(x)\,dx = 0$, for all $z < 0$. This remainder represents any nonguided parts of the optical fields (radiation losses, backward propagating in region (I)) as well as guided waves of higher orders, if applicable. Our primary result is the complex reflection coefficient $\rho = \rho_0 e^{i\phi}$ which separates into the reflectance $R = \rho_0^2$, and the phase change upon reflection ϕ. In case guided modes are supported in region (II), also the guided wave transmittance T, defined analogously, might be of interest. Typically all quantities will be investigated as functions of the angle of incidence θ.

6.2.1 Total Internal Reflectance

Beyond the discontinuity, in the region (II) of Figure 6.2, the structure becomes z homogeneous again. We assume that the core thickness there is smaller than the thickness in region (I), or, more precisely, that the effective index of the fundamental guided slab mode supported by region (II), if any, is smaller than N. Any in-plane propagating waves in region (II) can be characterized by a wavenumber kn_{II} and an effective index n_{II} that relate to the y-z-propagation. In case the layering of region (II) supports guided slab modes, the effective index of the fundamental mode constitutes an upper limit for n_{II}. If no guided modes exist, the larger one of the refractive indices for $x \to \pm\infty$ in region (II) (i.e. the maximum of the substrate or cover refractive indices) establishes an upper bound for n_{II}. Let N_{II} denote that limiting value.

Our ansatz (6.2) covers region (II) as well. All in-plane propagating waves there can thus be associated with a propagation angle θ_{II}, such that Snell's law holds for the in-plane propagation:

$$k_y = kN\,sin\,\theta = k\,n_{II}\,sin\,\theta_{II} \le kN_{II}\,sin\,\theta_{II}. \tag{6.7}$$

Propagating waves in region (II) require $\sin\theta_{II}$ to be real, i.e. $\sin\theta_{II} \le 1$. Consequently, if the angle of incidence θ exceeds the critical angle θ_c given

by

$$sin\,\theta_c = \frac{N_{II}}{N}, \tag{6.8}$$

no in-plane propagating waves can exist in region (II), and hence no optical power is being transferred into that region (evanescent waves, which decay exponentially in the $+z$-direction, are well permitted).

More formally this can be seen as follows. With a view to the completeness of the operator of Sturm-Liouville type in Equation (6.3), here for region (II), we can restrict to solutions of Equation (6.1), or Equation (6.5), respectively, in the separable form

$$E_{II}(x,y,z) = \Psi_{II}(x)e^{-i(k_y y + k_{II,z}z)} \tag{6.9}$$

where the local "mode" profile Ψ_{II} satisfies

$$\partial_x^2\Psi_{II} + k^2\epsilon_{II}\Psi_{II} = \left(k_y^2 + k_{II,z}^2 z\right)\Psi_{II} \le k^2 N_{II}^2\Psi_{II}. \tag{6.10}$$

Remember that N_{II} has been introduced above as a limiting value, not (necessarily) the actual effective index of the wave in question. In-plane propagating waves of this form, i.e. solutions with $k_{II,z}^2 \ge 0$, thus require that $k^2 N_{II}^2 - k_y^2 \ge 0$, or, using the ansatz (6.4), that the angle of incidence θ does not exceed the critical angle defined in Equation (6.8).

A similar reasoning can be applied to any reflected waves in region (I) that propagate in the negative z-direction, i.e. that carry potential radiative losses. These waves can be associated with an effective index N_1, relating to y-z-propagation. Typically N_1 would be the effective mode index of the first order slab mode, if applicable, or alternatively the maximum of the core/cladding refractive indices, as the limiting value for the continuum of

core/cladding "modes". Also here we can associate an in-plane propagation angle θ_1 with these waves, which needs to comply with Equation (6.2):

$$k_y = kN \sin\theta = kN_1 \sin\theta_1. \tag{6.11}$$

Propagating waves in region (I), beyond the fundamental guided slab mode with effective index N, can exist only if $\sin\theta_1 \leq 1$, or for incidence angles θ below the critical angle

$$\sin\theta_r = \frac{N_1}{N} \tag{6.12}$$

for the in-plane propagation of higher order waves in region (I). In particular, for $\theta > \theta_r$, no backwards traveling propagating waves are permitted in region (I), apart from the fundamental guided mode. Any optical power reflected from the interface is thus being carried away by that mode, there are no radiation losses due to reflected waves, the guided wave reflectance and transmittance (attributed to the fundamental mode only) add up to unity, $T + R = 1$. If in addition $\theta > \theta_c$, then the interface reflects the entire incident power into the backwards traveling fundamental guided mode, $R = 1, T = 0$. In that case one can indeed speak of total internal reflection for the semi-guided plane waves.

Note that, in case that regions (I) and (II) share the same z- and y-uniform cladding, as considered in Section 6.3, θ_r also limits the range of incidence angles where higher order propagating waves can exist in region (II). In fact, as seen by evaluating Equation (6.5) at a position where $\epsilon(x,z) = N_1^2$ (examples are the substrate and cover regions in the examples of Section 6.3), the effective permittivity ϵ_{eff} in the cladding is negative for incidence angles beyond θ_r, i.e. permits only (x-, z-) evanescent waves. Note further that most of this reasoning applies as well for configurations with a tapered domain—of in principle arbitrary shape—in between the regions (I) and (II). Exceptions would be configurations with an intermediate higher refractive

index, or larger core thickness (here one must expect the existence of guided waves, propagating in the y-direction), or large intermediate substrate or cladding indices that establish something like a half- or double-infinite "vertical core".

While these arguments rest on Equation (6.1), i.e. are valid for scalar (TE-like) waves only, one could analogously write equations for a second set of characteristic angles that relate to waves with vertical ($-x$) profiles of TM shape. In case the transition does not cause any (substantial) polarization coupling, the former considerations are applicable independently to TE- and to TM polarized waves. Otherwise one would have to consider both characteristic sets together in order to identify ranges of angles of incidence, where the different types of polarized waves in regions (I) or (II) can exist, i.e. where power transfer between the respective waves is permitted or forbidden.

6.2.2 Goos-Hänchen-shift

Bundles of solutions (Equation (6.6)), for different angles of incidence θ, or different wavenumbers k_y, respectively, can describe what happens to a vertically guided, laterally wide, non-guided beam when it encounters the interface [10, 11]. For the guided part of the waves in region (I), and for configurations with total internal reflection ($\rho_0 = 1$), such a superposition reads

$$\tilde{E}_{I,g}(x,y,z) = \int A(k_y)\Psi(x)\left\{e^{-ik_z(k_y)z} + e^{i\phi(k_y)}e^{ik_z(k_y)z}\right\}e^{-ik_y y}dk_y. \tag{6.13}$$

The second term represents the reflected waves; for total internal reflection only the phase part of the reflection coefficient remains. Its functional form $\phi(k_y)$ is known only implicitly through the numerical results. Note that the explicit dependence $k_z(k_y)$, as stated in Equation (6.6), will not be used

below.

We now assume that the amplitudes $A(k_y)$ of the wave packet are nonzero only in a small region of values k_y around $k_{y0} = kNsin\theta_0$, related to the principal angle of incidence θ_0 of the beam, such that expansions $k_z(k_y) \approx k_{z0} + (k_y - k_{y0})v_0$ and $\phi(k_y) \approx \phi_0 + (k_y - k_{y0})\Delta_0$ of first order, with abbreviations $k_{z0} = k_z(k_{y0})$, $v_0 = \frac{dk_z}{dk_y}|_{k_{y0}}$, $\phi_0 = \phi(k_{y0})$, and $\Delta_0 = \frac{d\phi}{dk_y}|_{k_{y0}}$ suffice for evaluating the integrals formally:

$$\tilde{E}_{I,g}(x,y,z) = \Psi(x)\left\{F(y + v_0 z)\, e^{-ik_{z0}z} + e^{i\phi_0}\, F(y - v_0 z - \Delta_0)e^{-ik_{z0}z}\right\}e^{-ik_{y0}y}. \tag{6.14}$$

The incident and the reflected beam share the same envelope $F(\xi) = \int A(k_{y0} + q)\, e^{-i\xi q} dq$, where, in the plane of incidence $z = 0$, the reflected beam is displaced by the lateral distance Δ_0, relative to the incident beam. Using the relation in Equation (6.4), and dropping the zero subscripts, the expression for the Goos-Hänchen shift Δ of a beam at incidence angle θ can be given the form

$$\Delta = \frac{1}{kNcos\theta}\frac{d\phi}{d\theta}. \tag{6.15}$$

According to the schematic view in Figure 6.3, the lateral shift can be viewed as a geometric reflection at an effective boundary at a distance $\delta = \Delta/(2\, tan\, \theta)$ behind the actual physical interface. Respective values for Δ and δ complement the results for reflectance R and phase change upon reflection ϕ in Section 6.4. Note that the reasoning in this section remains valid for total internal reflection at slab waveguide transitions of arbitrary shape (e.g. for the tapered configurations of Section 6.3.2), as long as the region (I) on the left $z < 0$ of the “interface” is z-homogeneous (where the

precise interface position is arbitrary, in principle), provided that the data for $\phi(\theta)$ is calculated and applied consistently.

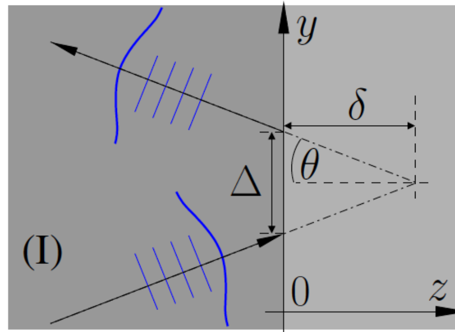

Figure 6.3: Lateral shift Δ (Goos-Hänchen-shift) of a semi-guided beam upon total internal reflection with incidence angle θ at the border of region (I). The displacement can be viewed as the effect of a geometric reflection of the ray associated with the beam at an effective interface that is positioned at a distance δ apart from plane $z = 0$ of the physical discontinuity.

6.3 Examples

The numerical experiments of the following paragraphs rely on the quasianalytical scalar 2-D Helmholtz solver of [12, 13]. Guided mode analysis of channels with 2-D cross sections, as required for the approach of Chapter 3, has been carried out with the quasianalytical technique of [14] (step discontinuities), and with the vectorial finite-difference solver of [15] (tapered transitions). Note that errors are inherent to all these results. For the Helmholtz solver, mainly the effect of the limited computational window and the staircase approximation, for the tapered solutions, are to be mentioned. The mode solvers are invoked for quasi-TE or vectorial, TElike polarized waves. Consequently, different continuity conditions for the lateral interfaces might cause a disagreement with the truly scalar results from the

Helmholtz solvers. Although reasonable convergence, up to the scale of the figures, has been assured in all cases, certain "noisy" features in the respective curves, especially when it comes to derivatives (i.e. differences of possibly defective values), must probably still be attributed to numerical uncertainties. Parameters have been adopted to be comparable with the practical design of the prism spectrometer in Chapter 3. Referring to the insets of Figures 6.4, 6.6, configurations are specified in terms of the core and cladding refractive indices $n_g = 2.0081$ and $n_b = 1.4524$, the slab thicknesses in region (I) $d = 160\,nm$ and region (II) $r = 40\,nm$, for vacuum wavelength $\lambda = 850\,nm$, and in-plane (TE, quasi-TE) polarized (scalar) waves. The slabs of thicknesses d and r, respectively, support guided modes with effective indices $N = 1.678$ and $N_{II} = 1.479$. Equation (8) predicts a critical angle $\theta_c = 61.75°$ for total internal reflection at the transitions. Radiation losses are forbidden for θ larger than the angle $\theta_r = 59.92°$, in line with Equation (12), where the cladding refractive index n_b has been supplied for N_1. Unless stated otherwise, these values apply to all simulations in Sections 6.3.1, 6.3.2.

6.3.1 Step Discontinuity

Figures 6.4, 6.5 summarize our simulations for reflection at a step discontinuity. We look at the entire range of incidence angles first, by means of the scalar approach of Section 6.2. According to Figure 6.4(a), the level of transmittance $T = 0.74$, at normal incidence, remains nearly stationary for incidence angles close to θ_r. The level of reflectance, $R < 0.01$ for $\theta = 0$, increases gradually with θ approaching that limit. For $\theta \geq \theta_r$ one indeed finds $R + T = 1$; the transmittance drops to $T = 0$ for $\theta \geq \theta_c$.

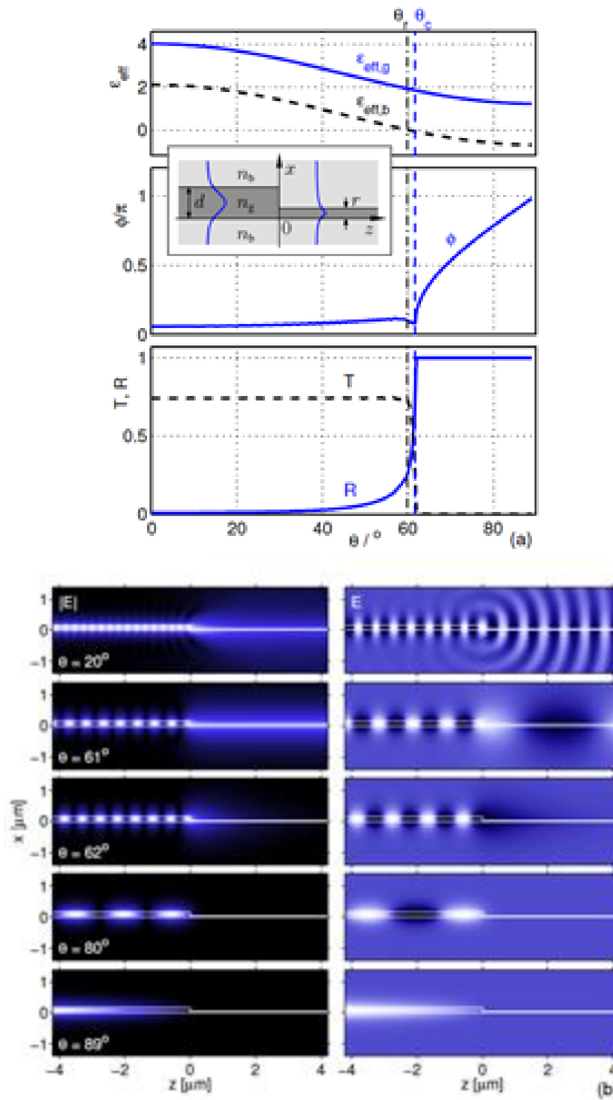

Figure 6.4: Reflection of a semi-guided plane wave at a step discontinuity. (a): Guided wave reflectance R, transmittance T, phase change upon reflection ϕ , and effective permitivities of the background $\epsilon_{eff,b}$ and guiding regions $\epsilon_{eff,g}$, versus the angle of incidence θ. (b): absolute values and time snapshots of the time-harmonic scalar field E associated with the effective problem (Equation (6.5)) for different angles of incidence θ.

At $\theta = \theta_r$, the effective permittivity $\epsilon_{eff,b}$ associated with the substrate and cladding regions, becomes negative. This manifests as well if one takes a look at the associated fields in Figure 6.4(b). At $\theta = 20° < \theta_r < \theta_c$, backwards and forward traveling propagating waves are visible, corresponding to forwards and backwards radiative losses. These waves are suppressed for $\theta_r < \theta = 61° < \theta_c$; the field is to be attributed mainly to the fundamental modes, with a partly standing, partly traveling wave in the input segment $z < 0$, and the wider, outgoing guided mode for $z > 0$. At even higher angles of incidence $\theta_r < \theta_c < \theta = 62°, 80°, 89°$, the incident guided mode is being fully reflected. No propagating waves are permitted in region (II); for $z > 0$ one merely observes evanescent field tails that decrease in extension, if θ grows towards grazing incidence.

Figure 6.5 considers the range of angles with total internal reflection in more detail. In part (a) the $\phi(\theta)$-curve of Figure 6.4(a) is being accompanied by values from mode calculations for channel waveguides of different widths. Some of these mode profiles, together with mode indices and mode angles, are shown in Figure 6.5(b). The profiles relate to the fields of Figure 6.4(b), for nearby angles of incidence.

For grazing incidence $\theta \to 90°$, one expects the field at the interface $z = 0$ to vanish; accordingly the phase change upon reflection ϕ approaches π (Equation (6.6)). ϕ decreases for lower incidence angles, with growing slope, down to the kink at the critical angle θ_c. By using finite-difference approximations for the derivatives, the $\phi(\theta)$-data can be translated to the curves for the beam displacement Δ and the effective boundary position δ, as shown in the upper panel of Figure 6.5(a). Large values for the Goos-Hänchen shift emerge for the steep slope of $\phi(\theta)$ at the critical angle, and for vanishing $cos\theta$ for grazing incidence. The geometrical "penetration depth" of the beams remains small for the step transitions; the largest values are found for the long evanescent field tails just above the critical angle.

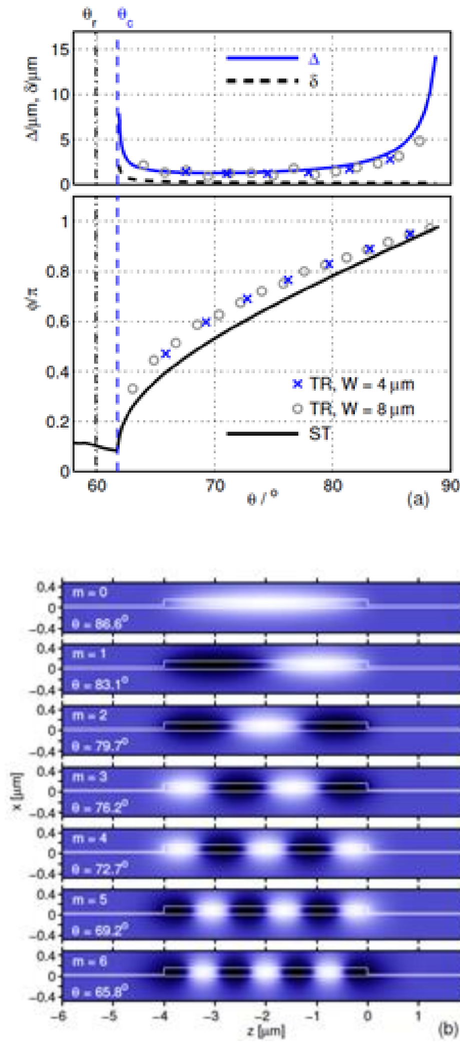

Figure 6.5: Total internal reflection of semi-guided plane waves at the step discontinuity of Figure 6.4. (a): Phase change ϕ of the guided wave upon reflection, associated Goos-Hänchen-shift Δ, and the effective boundary distance δ, as a function of the angle of incidence θ; estimates determined as outlined in Section 6.2 (scalar theory, ST) and Chapter 3 (transverse resonance, TR), in the later case by mode analysis of rib waveguides of different widths W. (b) Guided mode profiles of a rib of width $W = 4\ \mu m$, constituted by two of the former step discontinuities, with associated mode indices m and mode angles θ.

6.3.2 Tapered Transition

Results for linearly tapered transitions have been collected in Figure 6.6. For part (a) the parameters are as given in Figures 6.4, 6.5; the curves in those figures can thus be viewed as the limit of the data in Figure 6.6 for zero taper length. To match the actual final design in Chapter 3, for the simulations in (b) we assumed a slightly larger thickness $d = 170\,nm$, leading to accordingly different angles $\theta_r = 59.08°$ and $\theta_c = 60.84°$. Nevertheless the curves in Figure 6.6(b) should be discussed as part of the series in Figure 6.6(a), for a “long” taper.

The effects of lossless total internal reflection beyond a critical angle of incidence, and the partial lossless reflection in a small intermediate interval of incidence angles, occur for the tapers as well as for the step discontinuity. Note that these characteristic angles do not depend on the intermediate shape of the transition.

The absolute phase change upon reflection grows with increased taper length, as does the lateral beam displacement, and the penetration depth of the beam into the tapered region. The kink in the $\phi(\theta)$-curve at $\theta = \theta_c$ appears to become less pronounced for more extended transitions. Just as for the step discontinuities, extremal values for Δ and δ are observed for incidence close to the critical angle, and for grazing incidence. Still, in case of the long taper of Figure 6.6(b), these deviations are substantial also for intermediate angles reasonably well above the critical angle, e.g. at $\theta = 65°$ with $\Delta = 92\,\mu m$ and $\delta = 21\,\mu m$. Here the geometrical penetration depth turns out to be larger than the actual length of the taper.

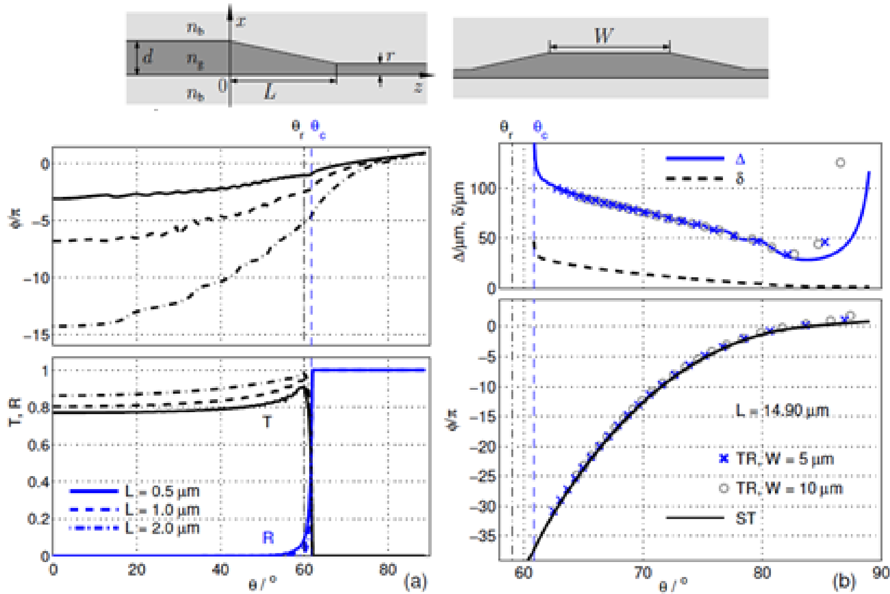

Figure 6.6: Simulations of tapered transitions of different length L. (a): Reflectance R, transmittance T, and the phase change upon reflection ϕ as a function of the angle of incidence θ, computed with the scalar approach of Section 6.2. (b): Configurations with total internal reflection, phase change upon reflection ϕ, lateral beam shift Δ and geometrical penetration depth δ versus the incidence angle θ, for a taper extension $L = 14.90\ \mu m$ (taper angle 0.5°).

6.4 Conclusion

Standard simulation tools can provide approximate quantitative insight on the 3-D slab-transition problem. Where applicable, the results obtained with a scalar 2-D Helmholtz solver and by guided mode analysis of rib waveguides with 2-D cross sections agree reasonably well, given the underlying approximations. Both scalar approaches take the light polarization into account only through the vertical shapes of the major parts of the optical fields, which are here assumed to be in-plane polarized.

Two characteristic angles have been identified, determined solely by the properties of the input- and output regions. Radiation losses are forbidden for wave incidence beyond the first angle, while guided transmission is still allowed. For incidence at angles larger than the second, the critical angle, the entire incident power is being reflected into the guided incoming mode. Only in that regime the “conventional” viewpoint, where one assigns effective mode indices to the regions with constant thickness, followed by application of Snell’s law, is valid. These observations hold for step discontinuities as well as for tapered transitions of (reasonably) arbitrary shape and extension, exemplified by our results on linear tapers of different lengths.

More accurate results would require the (computational) solution of the exact equations. This then concerns a vectorial Helmholtz equation on a 2-D computational domain, with transparent boundary conditions that permit the influx of the properly rotated guided slab mode. Since formally the problem is identical to a standard vectorial mode eigenvalue problem, it should be possible to modify some suitable solver accordingly. It is to be anticipated that phenomena like polarization coupling / field hybridization, as found for specific channel waveguides, will also occur for the present angled slab transition problems.

6.5 References

[1] P. K. Tien. Integrated optics and new wave phenomena in optical waveguides. *Reviews of Modern Physics*, 49(2): 361–419, 1977.

[2] R. Ulrich and R. J. Martin. Geometrical optics in thin film light guides. *Applied Optics*, 10(9): 2077–2085, 1971.

[3] G. C. Righini, V. Russo, S. Sottini, and G. Toraldo di Francia. Geodesic lenses for guided optical waves. *Applied Optics*, 12(7): 1477–1481, 1973.

[4] F. Zernike. Luneburg lens for optical waveguide use. *Optics Communications*, 12(4): 379–381, 1974.

[5] S.Misawa,M. Aoki, S. Fujita, A. Takaura, T. Kihara, K. Yokomori, and H. Funato. Focusing waveguide mirror with a tapered edge. *Applied Optics*, 33(16): 3365–3370, 1994.

[6] C.-C. Tseng, W.-T. Tsang, and S. Wang. A thin-film prism as a beam separator for multimode guided waves in integrated optics. *Optics Communications*, 13(3): 342–346, 1975.

[7] G. C. Righini and G. Molesini. Design of optical-waveguide homogeneous refracting lenses. *Applied Optics*, 27(20): 4193–4199, 1988.

[8] H. K. V. Lotsch. Reflection and refraction of a beam of light at a plane interface. *Journal of the Optical Society of America*, 58(4): 551–561, 1968.

[9] A. W. Snyder and J. D. Love. *Optical Waveguide Theory*. Chapman and Hall, London, New York, 1983.

[10] M. Hammer and O. V. Ivanova. Effective index approximations of photonic crystal slabs: a 2-to-1-D assessment. *Optical and Quantum Electronics*, 41(4): 267–283, 2009.

[11] M. Born and E. Wolf. *Principles of Optics, 7th. ed.* Cambridge University Press, Cambridge, UK, 1999.

[12] M. Hammer. Quadridirectional eigenmode expansion scheme for 2-D modeling of wave propagation in integrated optics. *Optics Communications*, 235(4–6): 285–303, 2004.

[13] M. Hammer. METRIC— Mode expansion tools for 2D rectangular integrated optical circuits. http://www.math.utwente.nl/_hammerm/Metric/.

[14] M. Lohmeyer. Wave-matching method for mode analysis of dielectric waveguides. *Optical and Quantum Electronics*, 29: 907–922, 1997.

[15] FieldDesigner, advanced optical mode solvers. PhoeniX Software, P.O. Box 545, 7500AM Enschede, The Netherlands; http://www.phoenixbv.com/.

7 Conclusions and Outlook

In this thesis, integrated optics based novel modules to be used in miniature Raman measurement systems are presented. Conclusions for the presented research and an outlook for possible future research will be given in this chapter.

7.1 Conclusions

In the course of this PhD study, we have focused on design, fabrication and characterization of three different integrated optical devices that are envisioned to be the parts of a low-cost, portable Raman measurement device. These devices can be listed as quasi-total internal reflecting (TIR) light turning mirrors, integrated optical prism spectrometers and on-chip polarization splitters. The devices are fabricated by using the SiON material platform.

Efficient integration of optical and electronics chips is an important aspect of realizing small scale Raman measurement devices. In this work, we developed quasi-TIR-based, 90° out-of-plane light-turning mirrors with high efficiency for hybrid flip-chip integration of SiON waveguides and CMOS-based photodiodes. The mirror is formed by locally removing the 45° Si facet at the interface between the truncated SiON waveguide and air. The design, modelling, fabrication and characterization of these mirrors are discussed in Chapter 2. The functional loss of the fabricated mirrors is measured as 6.2% for TE and 17.8% for TM polarization, reasonably close to the values obtained from approximate calculations being 7% and 15%, respectively.In Chapter 3, we have described the performance and design aspects of integrated optical prism spectrometers, which utilize dispersion effects in slab waveguides with two different thicknesses. The interfaces between the different slab waveguide regions are assumed to be adiabatic via

vertical tapering. We used the principles of geometrical optics and diffraction theory for optimization of the parameters. Furthermore, a new method to determine the effect of modal phase shifts upon modal reflection by mirrors in the device has been presented. The design strategy was illustrated by a numerical example assuming SiON technology. The device is designed for TE polarized light with a central wavelength of 850 nm, a channel spacing of 5 nm, an adjacent channel cross talk of $-40\,dB$ and a cross talk of $-50\,dB$ over a wavelength range of $100\,nm$. These choices lead to a required device area of $5.5\,x\,13\,mm^2$.In Chapter 4, the design, fabrication and characterization of an integrated optical prism spectrometer to be operated with TE polarized light at a center wavelength of 850 nm and with 5 nm channel spacing. The design strategy proposed in Chapter 3 has not been followed for this device owing to the relatively long fabrication period for such devices, so that the fabrication of the device had to be started prior to finishing the full design strategy. Exciting the fabricated device with light at the central wavelength and taking photos of the light scattered from the various parts of the chip it was found that, as anticipated based on the over length of the tapering (due to an underestimation in the fabrication), that the light was not well focused onto the output waveguide. Measuring the output spectra of a few output showed an unexpected and unexplainable peak break-up in addition to peak broadening. The wavelengths captured by the different output waveguides were approximately the correct ones. The angular dispersion of the beams emerging from the prism was found to have approximately the design value with an error of 10%, which lead to a measured channel separation of ~4.5 nm.

In Chapter 5, design, fabrication and characterization of an on-chip polarization splitter device to be used for center wavelength of 850 nm are presented. The device is composed of ridge waveguides for light transport, elliptic mirror for focusing and polarization splitting trench. The mirror and trench were based on adiabatically connected waveguiding slabs. Characterization results, which are obtained by exciting the device with light at the central wavelength and taking photos of the light scattered from the

various parts of the chip, show that the polarization splitter is working as expected except for the losses at the entrance of the receiver waveguides due to imperfect imaging. In order to determine the insertion loss, crosstalk and bandwidth of the device further measurements are needed but they could not be done due to lack of time.

In Chapter 6, the theoretical modeling for angled incidence of slab-guided waves to a tapered or step-like discontinuity by using a scalar 2-D Helmholtz equation is introduced. The results obtained with this model and by guided mode analysis of rib waveguides with 2-D cross sections, obtained in Chapter 3, agree reasonably well, given the underlying approximations.

7.2 Outlook

The research presented in this thesis demonstrates the on-chip optical building blocks of a miniature Raman measurement platform. Although we have obtained promising results with the fabricated devices, there is plenty of room for improvement, especially at the fabrication process stages of the components. Next, possible future research directions will be explained in detail.

As mentioned in Chapter 2, the buffer layer material used in the light turning mirror device could be changed in order to avoid the interaction between Si substrate and BPSG buffer layer. A possible candidate material is LPCVD TEOS oxide, with which we have achieved successful results in our preliminary deposition experiments.

Another significant future research direction for the light turning mirrors can be the monolithic integration of polymer lenses on top. The distinct advantage (for Raman spectroscopy applications) of incorporating such lenses is to enable out of plane focusing of waveguide output: If the sample is placed on the focal spot created by the polymer lens, the Raman scattered light from the sample can be directly collected into the waveguide that is used for excitation. Thus, a very compact on-chip Raman measurement

device, which does not need any external optical component for light delivery and collection, can be realized.

The fabricated spectrometers and polarization splitters should be investigated further, in order to understand unexpected results explained in Chapter 4 and 5. As a starting point, individual optical components (prism, parabolic and elliptic mirrors etc.) in the devices can be separately characterized. Furthermore, the measurement results can be confirmed by including fabrication errors and underestimated effects in the simulations.

A crucial enhancement for the prism spectrometer and polarization splitter should be in the direction of having a reliable fabrication process. First of all, etching of nitride layer, in which the adiabatic transitions between the waveguiding slabs are created, should be optimized. Furthermore, different material platforms can be considered for improving the overall device performance

In conclusion, the additioinal developments needed for achieving a complete Raman spectrometer can be summarized as follows. First, the prism spectrometers and polarization splitters should be fabricated by using the design strategy that takes the PSR effects into account and the fabricated devices should be characterized fully. If the characterization results show that the devices are good enough for a certain Raman measurement application, the fabrication should be done, while including the light turning mirrors into the functional chips. After that the chips have to be integrated with readout IC containing photodiodes. The integration process is yet to be developed.

Appendices

Appendix A: Surface Roughness Characterization for 45° Angled Si Walls

As described in Chapter 2, a special etchant is used in the anisotropic Si etching step to fabricate 45° angled Si walls. It is a mixture of TMAH and a very small amount of Triton x-100 surfactant [1]. In this etchant, the etch rate of the {110} plane is approximately four times lower than the etch rate of the {100} plane, corresponding virtually to an etch stop at the {110} plane [2]. Therefore the desired wall angle can be achieved by using this etch stop since the angle between the wafer surface and the {110} planes is 45 °. The surface quality of the etched Si walls should be essentially good since these walls are used as a template for the mirrors. The roughness of the walls, if present, will be transferred into the mirrors, which may decrease the reflection efficiency (due to scattering). The {110} walls, which remain after the anisotropic etching process, are not perfectly smooth as shown in Figure A.1(a). The roughness consists of narrow grooves all along the wall, from top to the bottom. This roughness is attributed to roughness in the masking oxide. In order to solve this problem the hard-bake duration of the photo-resist layer, which is used in the oxide patterning step, is increased to have smoother edges. Furthermore, a short BHF etching is applied to the samples, just before the anisotropic Si etching, to remove the native oxide layer. Figure A.1 shows SEM photos of the {110} wall (a) before and (b) after the modifications to the oxide patterning procedure. It is found that the change of the oxide patterning procedure helps to reduce the roughness of {110} walls, but there is still some minor roughness on the wall.

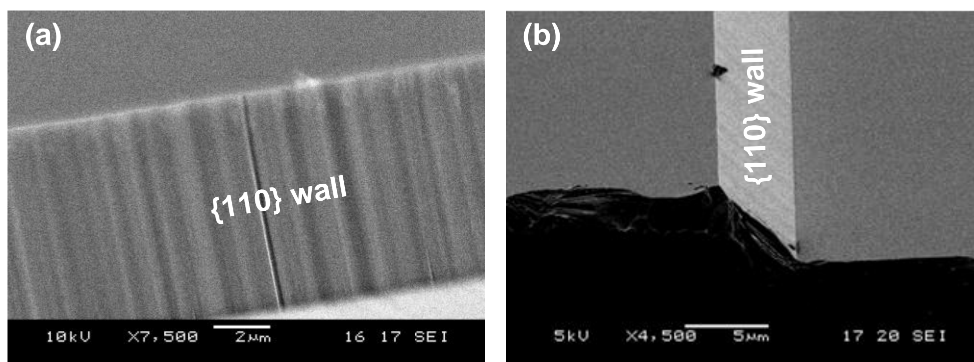

Figure A.1: SEM photos of the {110} wall (a) before and (b) after the modifications to the oxide patterning procedure.

In order to estimate the effect of the {110} surface roughness of the mirrorperformance, the optical setup in Figure A.2 has been constructed. The aim of the setup is to compare the reflection patterns originating from the bare Si wafer surface with that from etched {110} surfaces. A He-Ne laser, at a wavelength of 632 nm, is used as the light source in this setup. The laser is coupled into a single-mode fiber to obtain a high quality spot. The output of the fiber is placed at the focal point of a thin lens in order to produce a collimated light beam. This beam is focused on either the bare Si surface or the etched {110} surface and then the light, which is reflected from the sample, is captured by the camera.

Figure A.3 shows the light patterns reflected from two different Si surfaces. It seems that both the patterns are composed of more or less concentric rings, which is attributed to the effect of cut-off of the beam induced by the lens used for the collimation. The power reflected from these surfaces is also measured and the reflected power coming from the {110} wall is found to be as high as 95 % of that coming from the bare Si wafer surface. So, the {110} wall hardly introduces losses.

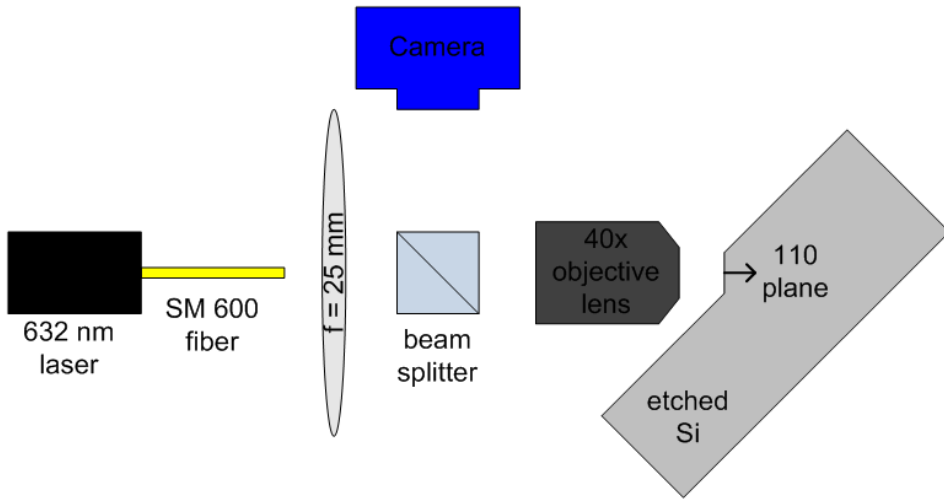

Figure A.2: The optical setup used for estimating the mirror performance.

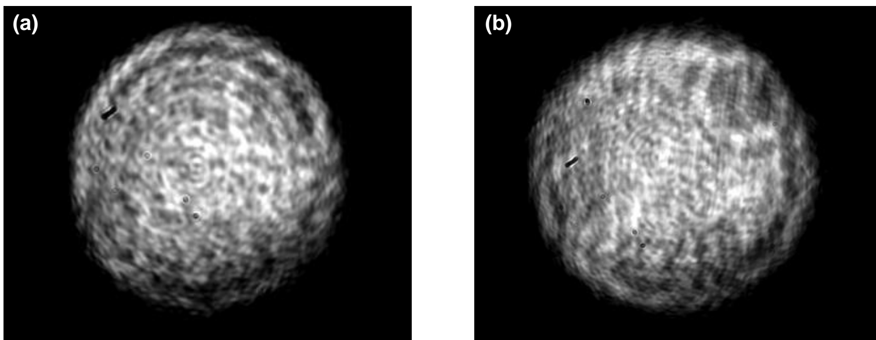

Figure A.3: The light patterns reflected from (a) bare Si wafer surface and (b) etched {110} wall.

References

[1] M. Gosálvez, P. Pal, B. Tang, and K. Sato, "Atomistic mechanism for the macroscopic effects induced by small additions of surfactants to alkaline etching solutions," Sensors and Actuators A: Physical, vol. 157, pp. 91-95, 2010.

[2] D. Resnik, D. Vrtacnik, U. Aljancic, M. Mozek, and S. Amon, "The role of Triton surfactant in anisotropic etching of {1 1 0} reflective planes on (1 0 0) silicon," Journal of Micromechanics and Microengineering, vol. 15, p. 1174, 2005.

Appendix B: Thermal Oxidation of Anisotropically Etched Si

As it was explained in Chapter 2, the wafer should be coated with a SiO_2 layer, which will be used as a buffer layer (Figure 2.3(d)), after the anisotropic Si etching process. Initially it was intended to use thermally grown SiO_2 as a buffer layer but in a later stage it was decided to use an annealed BPSG layer as a buffer layer. In this appendix we will explain this and describe the problems which occurred when thermal SiO_2 was tried to be used as a buffer layer.

Thermal oxidation leads to a very reliable coating which can be used as a buffer layer in SiON based integrated optics. It is a diffusion based process and it is not likely to generate any defects like voids and slits. Furthermore, it is a very conformal process which means that the thermally deposited oxide usually take on the shape of the underlying Si structure. Considering these advantages, we chose thermal oxide as a buffer layer material at the beginning of this study. Therefore, a 5 μm thick thermal oxide layer was grown at 1000 °C for the first samples. Figure B.1 shows the SEM pictures of some structures, which are obtained after the thermal oxidation process. As shown in Figure B.1(a), SiO_2 layer, which is thermally deposited on a 45° wall (before oxide deposition), has a conformal coverage on the Si structure and there is no void at the interface between Si and SiO_2. However, there is a serious problem resulting from the thermal oxidation process. As shown in Figure B.1(b) and B.1(c), the angle between the inclined walls and the wafer surface is decreased drastically. It is decreased from 45° to 36° for the inclined planes originated from the {110} planes and from 54.7° to 39.8° for the ones originating from the {111} planes. This change is due to the difference in the oxide growth rate at different Si planes [1]. During the oxide growth stress is created in the materials owing to expansion which

may alter the wall profile. The above effects make it impossible to use thermally grown oxide as a buffer layer for aimed structure, because none of the observed surface angles is suitable to provide a perpendicular incidence of the light on the photodiode (see Chapter 2).

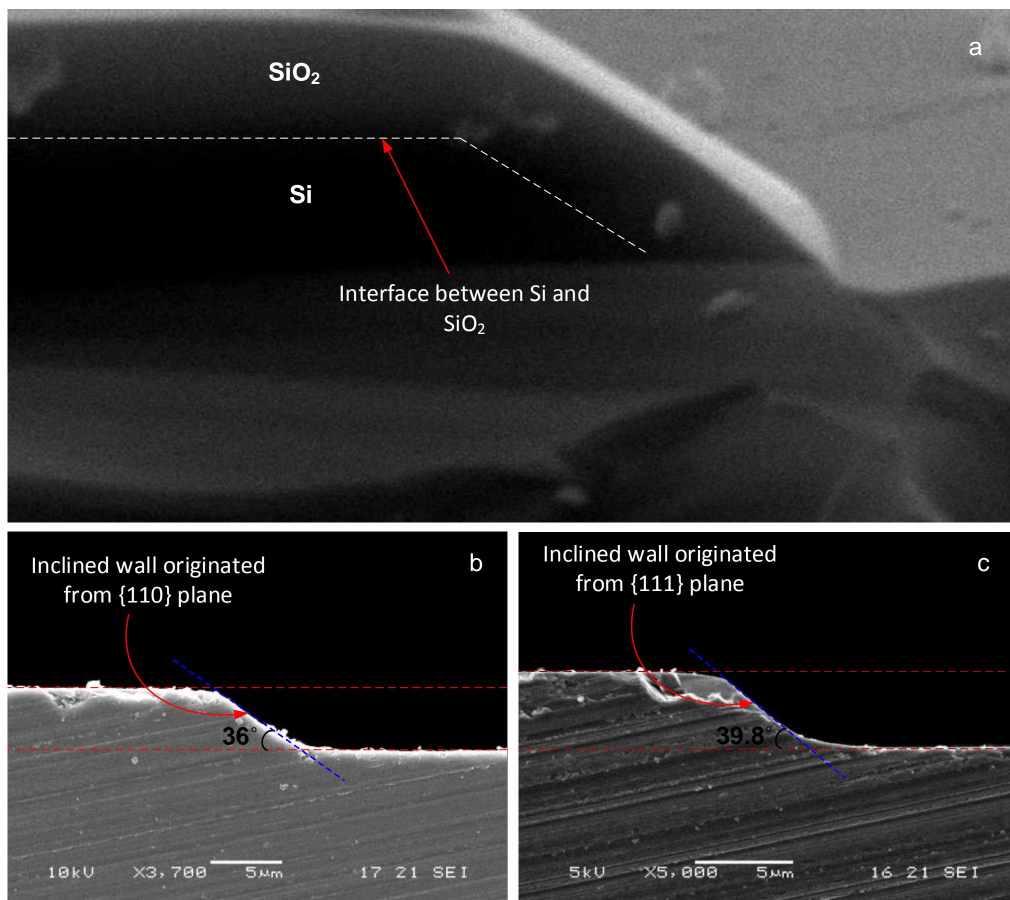

Figure B.1: SEM pictures of the thermally oxidized Si structures after (a) partial oxide removal from a sample that has {110} walls before the oxide deposition, (b) complete oxide removal from the same sample, and (c) complete oxide removal from a sample that has {111} walls before the oxide deposition.

References

[1] R. B. Marcus and T. T. Sheng. "The Oxidation of Shaped Silicon Surfaces". *Journal of the Electrochemical Society*, vol. 129, pp. 1278-1282, June 1982.

List of Publications

Journals:

F. Civitci, M. Hammer, and H. Hoekstra, “Design of a Prism Spectrometer based on Adiabatically Connected Waveguiding Slab,” *ready to be submitted*.

J. V. Lith, H. Hoekstra, F. Civitci, R. Stoffer, and P. V. Lambeck, “A compact optical chip for refractive sensing based on cut-off enhanced modal coupling changes”, *accepted to Sensors and Actuators B*.

F. Civitci, M. Hammer, and H. J. Hoekstra, "Semi-guided plane wave reflection by thin-film transitions for angled incidence," *Optical and Quantum Electronics*, vol. 46, pp. 477-490, 2014.

F. Civitci, G. Sengo, A. Driessen, M. Pollnau, A. Annema, and H. Hoekstra, "Light turning mirrors for hybrid integration of SiON-based optical waveguides and photo-detectors," *Optics Express*, vol. 21, pp. 24375-24384, 2013.

N. Ismail, F. Civitci, K. Wörhoff, R.M. de Ridder, M. Pollnau, and A. Driessen, “Efficiency of Integrated Waveguide Probes for the Detection of Light Backscattered from Weakly Scattering Media,” *Applied Optics*, vol. 50, pp. 935-942, 2011.

Conferences:

F. Civitci and H.J.W.M. Hoekstra, “Design of Spectrometers and Polarization Splitters Using Adiabatically Connected Slab Waveguides,” *16th European Conference on Integrated Optics*, April 2012.

F. Civitci, G. Sengo, A. Driessen, M. Pollnau, A.J. Annema, and H.J.W.M. Hoekstra, "45° Light Turning Mirrors for Hybrid Integration of Silica Optical Waveguides and Photo-detectors," *16th European Conference on Integrated Optics*, April 2012.

F. Civitci, A. Driessen, and H.J.W.M. Hoekstra, "Light Turning Mirrors for Hybrid Integration of Optical Waveguides in SiON Technology and CMOS Based Photo-detectors," *European Conference on Lasers and Electro-Optics 2011*, May 2011.

N. Ismail, F. Civitci, K. Wörhoff, R.M. de Ridder, M. Pollnau, and A. Driessen, "Integrated Waveguide Probes for Efficient Backscattered-Light Collection from Thin Samples," *European Conference on Lasers and Electro-Optics 2011*, May 2011.

M. Y. Tanrikulu, F. Civitci, and Tayfun Akin, "A New Method to Estimate the Absorption Coefficient for Uncooled Infrared Detectors," *SPIE Defense and Security Symposium, Infrared Technology and Applications XXXIV*, SPIE Vol. 6040, March 2008.

M. Tepegoz, F. Civitci, and Tayfun Akin, "An Optimum Reference Detector Design for Uncooled Resistive Microbolometer FPAs," *SPIE Defense and Security Symposium, Infrared Technology and Applications XXXIV*, SPIE Vol. 6040, March 2008.

Acknowledgement

First of all I would like to thank Markus Pollnau for giving me the opportunity to carry out my PhD in a well-equipped research group and for his prescient feedbacks during this study. I thank Alfred Driessen for our helpful discussions during my first year in IOMS. I especially would like to thank my supervisor Hugo Hoekstra for his invaluable guidance and patience throughout my PhD study, especially for the long hours of theoretical discussions and critical inputs during the thesis writing. I thank Anne-Johan Annema for giving me the opportunity to work in ICD group for a period. I also would like to thank Manfred Hammer for his extensive guidance and helps in chapter 6.

I would like to thank all the committee members for accepting our invitation in a short notice and spending their time for me.

I wish to thank Nur Ismail for fruitful collaboration that we did in my first year. In addition, I would like to thank him for our long hours of technical discussions. I thank Imran Akca for her continuous support and encouragements about my research. I thank Gabriel Sengo for his invaluable effort in the cleanroom for my project, we managed to realize very complicated processes with him.

I thank my office mates in Hogekamp; Jing Yang, Marko van Dalfsen, Marcel Hoekman, Lasse Kauppinen and Fei Sun for their kindness and hospitality.

I especially thank IOMS technicians Anton Hollink, Meinderst Dijkstra and Henk van Wolferen for their helps for constructing the measurements setups and for helping me in the cleanroom. It was very difficult for me to accept

loss of Anton, he was always with me when I was in trouble, rest in peace Anton.

I thank Feridun Ay, Kerstin Worhoff, Rene de Ridder, Sonia Garcia Blanco and Shanmugam Aravazhi for their helpful attitude all the time. I thank Dimitri Geskus and Saara-Maarit Reijn for giving me positive energy all the time. I thank Lantian Chang, So van Pham, Chaitanya Dongre, Edward Bernhardi, Laura Agazzi, Jonathan Bradley, Mustafa Akin Sefunc, Sergio Vazquez-Cordova and Yean-Sheng Yong for their friendship and kindness. I also would like to thank the secretaries, Brigit Binkhorst and Annitta Daid but especially to Rita ter Weele for helping me to settle in the Netherlands.

I would like to thank all my friends from TUSAT for their help and support whenever I needed. We did many joyful activities together.

I thank Albert Meulenkamp for giving me the opportunity to stay in a very wonderful apartment, and for his kindness.

I would also like to thank all members of OML for their friendship and support during last two years, especially Hakan Urey for giving me the opportunity to work in such a wonderful group and for giving me the motivation for obtaining my PhD when I was tired of thesis writing. I would also like to thank Onur Ferhanoglu for his friendship and for pushing me to finish my thesis.

I especially thank my very old friend Sertan Sukas and his wife Ozlem Sukas for their hospitality and support. I especially thank Gokce for giving me extra motivation to visit Enschede.

I thank Alyuz Family for their support and encouragement about the thesis and for the delicious dinners that they cooked.

I wish to thank my dad Sukru and my mom Fehime for their continuous and heartedly support through out my whole life. I also would like to thank my sisters Ozlem and Ozgun for their invaluable support, they never made me

feel alone even when we were living at different countries. I also would like to thank Ozden and Volkan for their friendship and encouragement. Very big thanks to my nieces Deniz and Duru, they always gave me power to concentrate on social life rather than work and that makes me feel happy.

Last but not the least, I thank Nese for her endless love, continuous support and extraordinary patience. She made a lot of sacrifice without any hesitation for me to finish this thesis. Without her I would not be able to finish this thesis as a healthy man.

Fehmi